Probing Interfacial Dynamics in Solid-State Lithium Metal Batteries

A Dissertation
Presented to
The Academic Faculty

by

John A. Lewis

In Partial Fulfillment
of the Requirements for the Degree
Doctor of Philosophy in
Materials Science and Engineering

Georgia Institute of Technology
May 2022

Probing Interfacial Dynamics in Solid-State Lithium Metal Batteries

Approved by:

Dr. Matthew McDowell, Advisor
School of Materials Science and Engineering
George W. Woodruff School of Mechanical Engineering
Georgia Institute of Technology

Dr. Juan-Pablo Correa-Baena
School of Materials Science and Engineering
Georgia Institute of Technology

Dr. Meilin Liu
School of Materials Science and Engineering
Georgia Institute of Technology

Dr. Tom Fuller
School of Chemical and Biomolecular Engineering
Georgia Institute of Technology

Dr. Faisal Alamgir
School of Materials Science and Engineering
Georgia Institute of Technology

Date Approved: April 13th, 2022

ACKNOWLEDGEMENTS

I first have to acknowledge my advisor, Matt McDowell, who has been the most important person to my success in grad school. His deep experience in batteries and materials science provided me with the expertise I needed as I gained my footing in the field. As I grew into an experienced student, he encouraged me to pursue my own ideas while still providing a healthy balance of feedback and perspective. PhD advisors can make or break a PhD, and I was fortunate that Matt consistently facilitated my growth as a researcher and person. I also would like thank my committee members Prof. Meilin Liu, Prof. Faisal Alamgir, Prof. Juan-Pablo Correa-Baena, and Prof. Tom Fuller for their time evaluating my work. I also want to express my gratitude towards Kumar Bugga, Will West, and the NASA organization for their support during my fellowship.

I'm lucky to have worked with so many talented researchers and gained good friends at the same time. Matthew Boebinger and Neha Kondekar were the first students under Matt, and the impact the group has had in materials science can be traced back to how they helped foster a positive culture. Matthew taught me how to conduct difficult characterization experiments with meticulous precision, while also providing a much needed outlet for sports talk. While Neha worked in a different subgroup, I still learned a great deal from her. She had a boldness and confidence in how she approached science, which I've learned are important traits to have when working on cutting edge topics.

Out of any grad student that I've worked with, Francisco Javier Quintero Cortes had the biggest impact on my growth as a researcher. Francisco was the first grad student

dedicated to working on solid-state batteries, and when I joined the group he taught me many of the skills I needed to succeed. Working together, we developed many of the tools and methodologies that have come to form the core structure of the solid-state battery subgroup. His background in X-ray science and talent at coding were invaluable our X-ray tomography projects, and was a key reason for our success. Beyond research, Francisco's conversations and desire for everyone to be happy had a huge impact on the group's culture. This was further amplified by Sang Yun Han, who always managed to make us laugh. Sang joined the solid-state subgroup later in his PhD life, but made important contributions to how we assemble and test our batteries. Talking to Sang about his experience working at Tesla has helped guide me to my own desire to work in industry. While I was the only PhD student to join the group in 2017, Jared Tippens also came to the group that year as a master's student, leading the group's first thrust into using X-ray tomography to characterize batteries. Jared helped design many of the cell housings that I ended up using later in my work, and leveraged his background in mechanical engineering to provide a unique perspective. Outside of the lab, we shared many common interests that made Jared a great friend (and now groomsman).

As I grew into an older grad student, I earned the role of leading and mentoring younger students in the group. This responsibility has been an important part of how I have grown as a researcher and person. While I recognize that I still have many things to work on as a leader, I appreciate the skills that I did gain during this time. To the younger grad students – Stephanie Sandoval, Kelsey Cavallaro, Clay Wright, Timothy Chen, Yuhgene Liu, Emily Klein, Lars Nelson, Sonakshi Saini, and Ziyi Li – I want to thank you for the various roles that you have played in my experience at Georgia Tech. This appreciation is

also be extended to all of the undergraduates the I've mentored, including Kirit Joshi, JP Berenguer, Dhruv Prakash, Thomas Marchese, David Yeh, and Ori Nofsinger. I'm proud that these students, as well as all of the other undergraduates who have worked in our group, have been able to achieve so much success. A special shout out is deserved for Chanhee Lee, who was a visiting student from Korea and helped me tremendously to fix the problems we had building sulfide solid-state batteries.

Beyond students, I want to acknowledge the post-docs that have helped me through my journey. Akila Thenuwara was the first post-doc the group ever had, and I was always impressed how he was able to balance his research projects and family life with his wife and young children. Pralav Shetty joined soon after, and brought phenomenal structure and organization along with a broad background in materials science. I've never met any researcher as consistently passionate about both his and other people's work. Two new post-docs, Sun Geun Yoon and Concheng Wang, recently joined and have already improved my understanding of how we can build better batteries.

Outside of the McDowell group, I would like to acknowledge the friendships that helped me get through my PhD. The first is my MSE cohort, who helped me succeed in my core classes and pass the qualifying exam my first year. I want to especially recognize Nick Kane, Sven Voigt, and Hannah Woods for the late night hang outs playing Catan and standing around the front door for an hour talking. Beyond Georgia Tech, I want to thank all of my friends from undergrad who have helped keep me sane throughout my PhD.

I wouldn't have been able to achieve what I've done during my PhD without my family's support. My parents have always believed in my ability to be successful. My dad,

Tom Lewis, has always pushed me to be the best person I can be and invoked the philosophy of legendary coach John Wooden, who said that "Success is peace of mind which is a direct result of self-satisfaction in knowing you made the effort to become the best you are capable of becoming". I appreciate that my mom, Martha Lewis, has always given me the freedom to be who I want to be. While we talk less than we should, I know that my sister Katy is proud of my accomplishments, and I'm proud of her own achievements in TV production. I also want to acknowledge my step-mom Ann Edwards, who has helped me understand what it takes to be a leader as an adult. Even though we're not legally family yet, I have thank my soon-to-be in laws Stacy and Alex Locke, who are two of the kindest people that I have ever met and have supported me for many years.

The last person I want to acknowledge is the most important person in my life, my fiancée Cori Locke. We've been together for over 10 years now, including long-distance during college and for over half of my PhD. Despite the distance, our relationship has stayed strong and her support for me hasn't wavered. I was lucky that she got into graduate school at the University of South Carolina for the last two years of my PhD, even though it was still a 3.5 hour drive away. I know that I've driven Cori crazy with how focused I can be on research, thinking about new ideas, talking about testing them, and spending long hours in the lab. Despite this, she has always respected my passion for research and supported me through both my lowlights and highlights.

TABLE OF CONTENTS

ACKNOWLEDGEMENTS **iii**

LIST OF TABLES **ix**

LIST OF FIGURES **x**

LIST OF SYMBOLS AND ABBREVIATIONS **xiv**

SUMMARY **xvi**

CHAPTER 1. INTRODUCTION AND BACKGROUND **1**
1.1 Conventional Lithium-Ion Batteries 1
1.2 Solid-State Batteries 7
1.3 Experimental Materials Background 15
1.3.1 NASICON Solid-State Electrolytes 15
1.3.2 Thiophosphate Solid-State Electrolytes 17

CHAPTER 2. EXPERIMENTAL METHODS **20**
2.1 Materials Synthesis and Processing 20
2.2 Solid-State Battery Assembly 21
2.3 Electrochemistry 24
2.4 Advanced Characterization 28
2.4.1 X-Ray Tomography 28
2.4.2 Electron Microscopy 34
2.4.3 Focused-Ion Beam Milling 37

CHAPTER 3. INTERPHASE MORPHOLOGY IN AN OXIDE ELECTROLYTE DRIVES CELL FAILURE **40**
3.1 Introduction 40
3.2 Chemical Reaction Between Lithium Metal and LAGP 41
3.3 Effects of Cycling on LAGP Decomposition 43
3.4 Conclusions 50

CHAPTER 4. OBSERVING INTERFACIAL DYNAMICS IN SOLID-STATE BATTERIES DURING CYCLING USING OPERANDO X-RAY TOMOGRAPHY **52**
4.1 Introduction 52
4.2 *Operando* X-Ray Tomography During SSB Cycling 53
4.3 Interphase Growth and the Absence of Lithium Plating 56
4.4 Interfacial Void Formation and Contact Loss 58
4.5 Volumetric Changes and Partial Molar Volume Mismatch 65
4.6 Conclusions 67

CHAPTER 5. HOW ELECTROCHEMCIAL PARAMETERS IMPACT LITHIUM METAL PENETRATION THROUGH SOLID-STATE ELECTROLYTES 69
5.1 Introduction 69
5.2 Limitations of the Critical Current Density 72
5.3 Threshold Capacity as a Metric to Evaluate Plating in SSBs 74
5.4 Relationship Between Threshold Capacity and Cycling Stability 78
5.5 Conclusions 86

CHAPTER 6. ELECTROCHEMICAL MECHANISMS OF ANODE-FREE SOLID-STATE BATTERIES 88
6.1 Introduction 88
6.2 Deposition of Lithium Metal at Cu/LPSC Interface 90
6.3 Impact of Stripping on Cycling Stability 96
6.4 Conclusions 103

CHAPTER 7. ENERGY DENSITY ANALYSIS OF ALLOY ANODES IN SOLID-STATE BATTERIES 104
7.1 Introduction 104
7.2 Mechanistic Advantages of Alloy Anodes in SSBs 105
7.3 Energy Density Analysis of Alloy Anodes 106
7.4 Conclusions 113

CHAPTER 8. CONCLUSIONS AND FUTURE WORK 114

APPENDIX 117
A.1 Tables for energy density calculations in Chapter 7 117

REFERENCES 120

LIST OF TABLES

Table 5.1: Summary of average threshold capacities measured in Figure 5.4. ……76

Table A.1: Composition and areal capacity for each SSB electrode evaluated. ……..117

Table A.2: Composition, areal capacity, and porosity for liquid electrodes. ……..118

Table A.3: List of the densities and specific capacities used. ……118

Table A.4: Average voltage, specific energy, and energy density for each configuration. ……..119

LIST OF FIGURES

Figure 1.1: Schematic of a rechargeable lithium-ion battery during discharge. ……2

Figure 1.2: Schematic of a solid-state battery. ……8

Figure 1.3: Thermodynamic predictions of the electrochemical stability windows of various SSEs based on DFT calculations. Materials are electrochemically stable at a given potential if it falls within the colored bar. ……...10

Figure 1.4: Schematic representation of the different types of interfacial stability at Li/SSE interfaces. **a)** A thermodynamically stable interface with no reaction. **b)** A reactive interface that decomposes into species with mixed conducting properties. **c)** An interface that reacts, but forms species that conduct ions and block electrons. ……..11

Figure 1.5: SEM images of contact loss at **a)** cathode/SSE and **b)** Li/SSE interfaces. ….13

Figure 1.6: X-ray tomography images taken from a lithium metal SSB during the formation of a short circuit. After initial cracking near the interface (top of image), a vertical crack is formed and propagates across the electrolyte, followed by lithium metal deposition into the crack. ……...14

Figure 2.1: a) Schematic and **b)** photo of the cell housing design used to make sulfide-based SSBs. The component dimensions could be altered depending on the user's constraints. In this thesis, all cell housings with this design had an inner die diameter of 10 mm. **c)** Schematic of the sealing mechanism added to some cell housings. ……23

Figure 2.2: An example of a Nyquist plot and its equivalent circuit model. …….27

Figure 2.3: Schematic of an X-ray tomography instrument. …….29

Figure 2.4: Schematic of the cell housing designed for *operando* X-ray tomography experiments. ……..31

Figure 2.5: Visualization of the segmentation procedure used to identify lithium metal electrodes in an X-ray tomography dataset. ……...33

Figure 2.6: Schematic of an *in situ* TEM holder used to probe battery reactions at the nanoscale. ……..36

Figure 2.7: SEM images of Li metal foil after FIB milling at **(a)** room temperature, **(b)** 0 °C, **(c)** -50 °C, **(d)** -100 °C, **(e)** -150 °C, and **(f)** -170 °C. ……..38

Figure 3.1: a) Plot of impedance versus time for a Li/LAGP/Li symmetric cell held at open circuit. **b)** Cross-sectional SEM image of the interphase formed by chemical reaction. **c)** *Ex-situ* glancing angle XRD of unreacted LAGP (black) and LAGP that was chemically

reacted for ~170 h (blue). **d-g)** *In-situ* TEM of the reaction of an LAGP particle with lithium. ……..42

Figure 3.2: a) Galvanostatic cycling of symmetric Li/LAGP/Li cells cycled to failure (defined to be ±10 V) at 0.1 mA cm^{-2} (black), 0.2 mA cm^{-2} (blue), and 0.5 mA cm^{-2} (red). **b-d)** Magnified plots of the galvanostatic traces presented in (a) at early cycling times. **e)** Impedance spectra of each cell in (a) prior to cycling. **f)** Impedance spectra of each cell after galvanostatic cycling to failure. ……44

Figure 3.3: a-c) Low-magnification cross-sectional SEM images of LAGP cycled until failure at **a)** 0.1 mA cm^{-2}, **b)** 0.2 mA cm^{-2}, and **c)** 0.5 mA cm^{-2}. The darker regions are the reacted interphase that has grown into the bulk of the LAGP. **d)** Higher-magnification SEM image of the interphase grown deep within LAGP. ……..45

Figure 3.4: Galvanostatic cycling of symmetric Li/LAGP/Li cells at **a)** 0.1 mA cm^{-2}, **b)** 0.2 mA cm^{-2}, and **c)** 0.5 mA cm^{-2}. For all three current densities, the capacity per half-cycle was 0.25 mAh cm^{-2} and the total capacity was 2.5 mAh cm^{-2}. **d-f)** Cross-sectional SEM images of LAGP after cycling with the same amount of Li^+ passed. ……46

Figure 3.5: Comparison of XPS spectra of electrochemically and chemically reacted LAGP. ……...48

Figure 3.6: Schematic showing the competing pathways between interphase formation and lithium metal deposition at unstable Li/SSE interfaces. ……49

Figure 4.1: Attenuation length calculated for $Li_{10}SnP_2S_{12}$. Smaller attenuation lengths indicated greater X-ray absorption by the material. The dashed line represents the X-ray energy used for all operando experiments (28 keV). ……54

Figure 4.2: a) Galvanostatic voltage curves measured during operando experiments at 1 mA cm^{-2}. **b-e)** Reconstructed cross-sectional images from X-ray tomography scans taken during cycling of the cell in (a). ……55

Figure 4.3: Analysis of interphase and lithium volume changes. ……57

Figure 4.4: Visualization of interfacial voids formed at the Li/LSPS interface. ……..59

Figure 4.5: a) Overlay of the measured electrochemistry and quantified contact area for each interface. **b**) Comparison between the experimental voltage curve and theoretically predicted voltage curves. ……...61

Figure 4.6: Evolution of contact area maps at each interface during the experiment. ….62

Figure 4.7: Electrochemical behavior of LPSC in the tomography cell housing. ……64

Figure 4.8: Dynamic mechanics of components in SSBs during cycling. ……...66

Figure 5.1: Effects of different CCD protocols on the measure CCD value. ……70

Figure 5.2: a) Critical current density test of a symmetric Li/LPSC/Li cell. **b)** Continuous plating at one interface in a Li/LPSC/Li cell at 0.6 mA cm^{-2}. ……72

Figure 5.3: Plot of the measured CCD versus areal capacity per half cycle used to compare the CCD measurement from the current study (green star) compared to other reports. …73

Figure 5.4: a) Plot of the threshold capacity as a function of current density for two electrolyte fabrication pressures: 125 MPa (red circles) and 375 MPa (blue circles). **b)** Example electrochemical curves of continuous plating experiments for the cells in **(a)**. **c)** SEM image of the cross-section of a pristine Li/LPSC interface. **d, e)** SEM images showing the morphology of LPSC pellets pressed at 125 and 375 MPa. ……75

Figure 5.5: Continuous plating at 1.4 mA cm^{-2} with an SSE fabrication pressure of 375 MPa and a stack pressure of **a)** 6 MPa and **b)** 30 MPa. ……..77

Figure 5.6: a) Cycling of symmetric Li/LPSC/Li cells at current densities of 1.4 mA cm^{-2} (green), 2.2 mA cm^{-2} (blue), and 3.0 mA cm^{-2} (red) with half-cycle areal capacities of 2.0 mAh cm^{-2}. **b)** Magnified plot from the cell cycled at 3.0 mA cm^{-2} in **(a)**. ……79

Figure 5.7: a) Stable symmetric cell cycling at 1.4 mA cm^{-2} using a half-cycle capacity of 6.0 mAh cm^{-2}. (b) Unstable cycling at 1.4 mA cm^{-2} when the half-cycle capacity was increased to 9.0 mAh cm^{-2}. (c) Unstable cycling at 2.2 mA cm^{-2} using a half-cycle capacity of 5.0 mAh cm^{-2}. ……80

Figure 5.8: SEM image of the composite cathode microstructure using **a)** a secondary electron detector and **b)** a backscattered electron detector. **c)** Magnified image of a polycrystalline NMC811 particle collected using secondary electrons. ……81

Figure 5.9: a) Charging a Li/LPSC/NMC811 full cell at 2.0 mA cm^{-2} with a cathode loading of 6.0 mAh cm^{-2} to form a short circuit during the first charge. **b-d)** Cycling a full cell at 2.0 mA cm^{-2} with different cathode loadings. ……82

Figure 5.10: Optical images of the cathode/LPSC interface, showing how the cathode thickness varied at different locations. ……...85

Figure 6.1: Schematics of an SSB with an excess lithium layer (left) and an anode-free configuration (right). The calculated specific energy and energy density for both architectures are labelled below. ……89

Figure 6.2: a) Deposition of lithium metal onto copper foil at 1 mA cm^{-2} in an anode-free Cu/LPSC/Li half cell with a stack pressure of 15 MPa. **b, c)** Optical and SEM images of thick lithium layers deposited at 1 mA cm^{-2}. **d-g)** EIS data gathered at different stages of the deposition in **(a)**. **h)** Depositing lithium metal onto copper foil at 0.5 mA cm^{-2} **i)** Depositing lithium metal onto copper foil at 1.5 mA cm^{-2}. **j)** Depositing lithium metal onto copper foil at 1 mA cm^{-2} using stack pressures of 5 MPa (blue curve) and 30 MPa (red curve). ……91

Figure 6.3: Comparison of FIB milling at different temperatures on the same sample. The left trench was milled at -145 °C, while the right trench was milled at 25 °C. ……94

Figure 6.4: SEM images taken after cryo-FIB milling through anode-free Cu/LPSC interfaces after deposition. **a,b)** 3 mAh cm^{-2} deposited at 0.5 mA cm^{-2} in a Cu/LPSC/Li half cell. **c,d)** 1 mAh cm^{-2} deposited at 1.5 mA cm^{-2} in a Cu/LPSC/Li half cell. **e,f)** 3 mAh cm^{-2} deposited at 0.5 mA cm^{-2} in a Cu/LPSC/NMC full cell. ……95

Figure 6.5: a) Cycling a Cu/LPSC/Li half cell at 0.5 mA cm^{-2} with 3 mAh cm^{-2} per half cycle. **b)** Cycling a Cu/LPSC/NMC full cell at 0.5 mA cm^{-2} with a cathode loading of 3 mAh cm^{-2}. **c)** Cycling a Li/LPSC/NMC full cell at 0.5 mA cm^{-2} with a cathode loading of 3 mAh cm^{-2}. This cell used a lithium metal anode with a thickness of ~0.3 mm. **d)** Comparison of the Coulombic efficiencies between the anode free full cell (red circles) and thick Li foil full cell (black circles). **e)** Magnified view of the plot in **(d)**. ……97

Figure 6.6: a-e) Limited cycling of anode-free SSBs to prevent effects of non-uniform stripping. **f)** Cycling a Cu/LPSC/Li half cell with a slow nucleation step at 0.1 mA cm^{-2}, followed by plating and stripping at 0.5 mA cm^{-2}. ……..100

Figure 7.1: Predicted energy density (Wh L^{-1}) and specific energy (Wh kg^{-1}) of solid-state and liquid-based battery stacks with different anodes: graphite, lithium, and alloy materials (silicon, tin, aluminum). ……..110

Figure 7.2: (a) Specific energy (Wh kg^{-1}) and **(b**) energy density (Wh L^{-1}) for a SSB stack as a function of the electrolyte separator thickness and the volume fraction of active material in the anode. ……...112

LIST OF SYMBOLS AND ABBREVIATIONS

SSB	Solid-state battery
SSE	Solid-state electrolyte
CE	Coulombic efficiency
LCO	Lithium cobalt oxide, $LiCoO_2$
NMC	Lithium nickel manganese cobalt oxide, $LiNi_xMn_yCo_zO_2$
LFP	Lithium iron phosphate, $LiFePO_4$
SHE	Standard hydrogen electrode
SEI	Solid electrolyte interphase
LLZO	Lithium lanthanum zirconium oxide, $Li_7La_3Zr_2O_{12}$
NASICON	Sodium superionic conductor
LPS	Lithium phosphorous sulfide, $Li_7P_3S_{11}$
PEO	Poly(ethylene oxide)
MIEC	Mixed ionic-electronic conductor
LPSC	Lithium phosphorous sulfur chloride, Li_6PS_5Cl
LATP	Lithium aluminum titanium phosphate, $Li_{1+x}Al_xTi_{2-x}(PO_4)_3$
LAGP	Lithium aluminum germanium phosphate, $Li_{1+x}Al_xGe_{2-x}(PO_4)_3$
LGPS	Lithium germanium phosphorous sulfide, $Li_{10}GeP_2S_{12}$
LSPS	Lithium tin phosphorous sulfide, $Li_{10}SnP_2S_{12}$
XPS	X-ray photoelectron spectroscopy
LNTO	Lithium niobium tantalum oxide, $LiNb_{0.5}Ta_{0.5}O_3$
PEEK	Polyether ether ketone
EIS	Electrochemical impedance spectroscopy

$\boldsymbol{\sigma}$	Conductivity
$\boldsymbol{l}$	Thickness
$\boldsymbol{A}$	Area
$\boldsymbol{R}$	Resistance
$\boldsymbol{\theta}$	Angular resolution
$\boldsymbol{\lambda}$	Wavelength
$\boldsymbol{d}$	Aperture diameter
TEM	Transmission electron microscopy
SEM	Scanning electron microscopy
EDS	Energy-dispersive X-ray spectroscopy
FIB	Focused ion beam
XRD	X-ray diffraction
SAED	Selected area electron diffraction
CCD	Critical current density
$\boldsymbol{\rho}$	Density
$\boldsymbol{\phi}$	Volume fraction
$\boldsymbol{q}$	Specific capacity
$\boldsymbol{Q_{vol}}$	Electrode charge density
$\boldsymbol{Q_{areal}}$	Electrode areal capacity
$\boldsymbol{m}$	Mass
$\boldsymbol{V_{cell}}$	Cell voltage

SUMMARY

Solid-state batteries (SSBs) are a promising technology to surpass the energy density and safety of conventional lithium-ion batteries. These devices replace the flammable liquid electrolyte with a more stable solid-state electrolyte (SSE) that can conduct lithium ions. The rigid mechanical properties of SSEs are also promising for enabling the energy dense lithium metal anode, which is plagued by dendrite formation, side reactions, and dead lithium in liquid electrolytes. Despite advances toward SSEs with high ionic conductivity, the understanding and control over solid electrode/SSE interfaces have emerged as major challenges in the development of SSBs. Chemo-mechanical degradation is expected to be more severe in SSBs compared to conventional liquid-electrolyte-batteries because the SSE cannot reconfigure like liquids. Understanding chemical transformations at interfaces, mechanical damage, and lithium filament growth is therefore critical for engineering SSBs.

This dissertation investigates the underlying mechanisms of these interfacial phenomenon to better inform the design of SSBs. First, severe SSE decomposition caused by electrochemical side reactions with lithium metal is found when the reacted species exhibit mixed ionic-electronic conduction. Continuous decomposition ultimately results in fracture due to the build-up of internal stress, and this process is found to be accelerated when operating at higher current densities. Second, the dynamic evolution of Li/SSE interfaces is probed using *operando* X-ray tomography. 3D images of SSBs are obtained during operation, which are then processed using segmentation to quantify how phases change and link their behavior directly to the measured electrochemistry. Analysis reveals

that the significant loss of interfacial contact is responsible for cell failure in this experiment. Third, the relationships between unstable filamentary lithium metal deposition and electrochemical parameters, such as current density and areal capacity, are investigated. A new metric called the threshold capacity is introduced and used to evaluate lithium deposition behavior in SSBs. Cycling of cells with areal capacity controlled to be well below the threshold capacity is found to greatly improve cell lifetime, while approaching the threshold capacity results in rapid short circuiting. Fourth, the behavior and operational mechanisms of anode-free SSBs are investigated, in which lithium metal is deposited onto a bare copper current collector during the first charge. Using sulfide SSEs, it is demonstrated that substantial amounts of lithium can be deposited onto a copper current collector at a relatively high current density of 1 mA cm^{-2}. However, stripping lithium from the copper current collector is found to cause significant degradation that severely limits cycling lifetime. Strategies to mitigate the detrimental effects of stripping and extend cell lifetime are explored. Lastly, the energy densities of various battery chemistries are calculated at the cell-level. Alloy anodes in SSBs are shown to have competitive energy densities, and their mechanistic advantages over alloy anodes with liquid electrolytes and lithium metal SSBs are discussed.

.

CHAPTER 1. INTRODUCTION AND BACKGROUND

Modern technology demands large quantities of energy storage that can be conveniently accessed. Since their commercialization in the early 1990's, lithium-ion batteries have become a key method of storing energy in many people's daily lives. While the energy stored in lithium-ion batteries is low compared to fuels like gasoline (~1 MJ kg^{-1} vs ~50 MJ kg^{-1})[1], they offer a distinct advantage in that they can directly convert chemical energy into electricity without external devices. Furthermore, a typical lithium-ion battery can be charged and discharged for thousands of cycles without significant loss in its ability to store energy[2]. The electrochemical nature of lithium-ion batteries, combined with their excellent rechargeability and relatively high energy density compared to other electrochemical devices[3], has made them the most important energy storage device for powering the portable electronics that have come to dominate society over the past three decades. With the increasing need for electric vehicles and renewable energy grid storage to reduce atmospheric emissions, it is expected that the global deployment of lithium-ion batteries will increase from 195 GWh in 2019 to over 2000 GWh in 2030[4]. These demands have put pressure on manufacturers to make batteries with higher energy density, lower costs, and safer chemistries.

1.1 Conventional Lithium-Ion Batteries

A lithium-ion battery fundamentally consists of three primary components: an anode, a cathode, and an electrolyte (Fig. 1.1)[5]. The anode and cathode are what allow the battery to store energy by acting as hosts for lithium ions. When a lithium-ion battery is fully charged, the lithium ions are stored in the anode material. If an external load is

connected to a charged battery, it begins to discharge and supplies electricity to the load. This phenomenon occurs because there is a favorable potential difference between the anode and cathode that drives redox reactions at the electrodes. During this process, the anode is oxidized to liberate lithium ions and electrons. These electrons leave the anode and go to the cathode through the external load, doing electrical work in the process. To ensure that charge is conserved, lithium ions are transported through the electrolyte and enter the cathode, where they are then reduced by electrons. Eventually, lithium stored in the anode is exhausted or too difficult to remove, and no more energy can be extracted from the cell. However, the battery can return to its charged state by supplying external electrical energy to drive the electrochemical reactions in reverse.

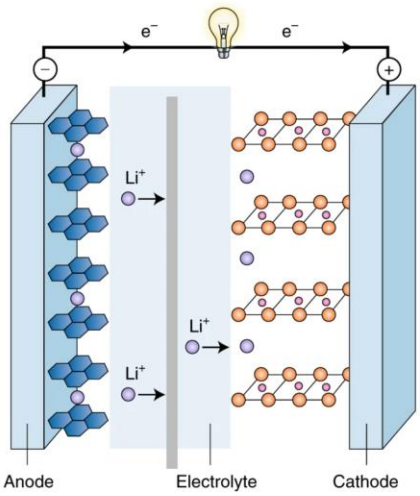

Figure 1.1. Schematic of a rechargeable lithium-ion battery during discharge. Adapted with permission from reference[6]. Copyright 2018 Springer Nature.

Various metrics are used to gauge the performance of a lithium-ion battery. Two key parameters are the specific energy (Wh kg^{-1}) and energy density (Wh L^{-1}), which describe how much energy is stored per amount of the battery. It is important to note that

these two parameters are often discussed at different architecture levels. For example, the cell-level energy density only considers the components that are necessary to run the electrochemical reactions (electrodes, electrolyte, and current collectors), whereas the pack-level energy density takes into account the additional components like the cell housing that are necessary to integrate the battery into a device. Conventional lithium-ion batteries typically achieve cell-level specific energies of ~250 Wh kg^{-1}, which decreases to ~150 Wh kg^{-1} at the pack-level[7].

The electrochemical properties of the electrodes play key roles in determining a cell's energy density. One important parameter is the amount of lithium ions that can be stored in each electrode, which is known as the capacity. Each material has a theoretical specific capacity, i.e. the amount of capacity that can be stored per unit mass (mAh g^{-1}). Higher specific capacities are desirable because more lithium ions are stored in the battery, providing more electrons that can do useful electrical work when connected to a load. While a material may have a high theoretical specific capacity, the practical specific capacity that can be stably accessed is often lower[8,9]. This effect is often due to structural damage that is introduced when extracting or inserting too many lithium ions into the electrode, which must be avoided to improve cell lifetime.

Another electrochemical parameter of interest is the potential(s) at which an electrode reaction(s) occur. The difference between the potentials of the anode and cathode determines the cell voltage, which is used directly to calculate energy density[5,10]. Maximizing this potential difference is therefore a common way to increase energy density. However, there are important trade-offs when it comes to maximizing cell voltage. One issue is that the electrolyte may not be stable at the electrode potentials and will

decompose[5]. It may also be disadvantageous to use materials that maximize cell voltage if they have lower specific capacities compared to other options.

While the specific capacity and electrochemical potentials govern the energy density of a cell, it is also important to evaluate cell stability and lifetime. The two most common metrics used to track degradation are the Coulombic efficiency and capacity retention. Coulombic efficiency (CE) is defined as the ratio of the discharge capacity to the charge capacity[11]. Capacity retention refers to the fraction of the initial discharge capacity that is retained as a function of cycle number. A common reference for cell lifetime performance is the number of times a cell can be cycled until the capacity retention is 80%[11]. For a lithium-ion battery to cycle for hundreds of times before hitting this 80% mark, the average Coulombic efficiency must be >99.95%.

The electrodes in conventional lithium-ion batteries are composites consisting of the active material that stores lithium ions and additives that improve performance[12]. The active material typically comprises ~95% of the total mass of the composite. A binder additive is introduced to improve the mechanical properties of the electrode and hold particles together. Conductive particles, such as carbon black, are also added to increase the electrical conductivity in the electrode. The composite electrode has a porosity of ~30%[12], which allows for the liquid electrolyte to infiltrate the electrode and establish pathways for ion conduction between active particles. The liquid electrolyte must be a good lithium ion conductor to minimize cell impedance, as well as an electronic insulator to ensure that the electrons do work through the load instead of traversing across the electrolyte[13]. Without these porous channels, the impedance of the cell would be too high,

as the ions can typically conduct much faster through the liquid electrolyte than the active material.

The first successful commercial lithium-ion battery used graphite as the anode and $LiCoO_2$ (LCO) as the cathode[6,14]. These materials are known as intercalation compounds, meaning that ions are stored in between the layers of the host material. During cycling, lithium ions are intercalated and de-intercalated via the following redox reactions.

$$Li_xC_6 \leftrightarrow C_6 + xLi^+ + xe^- \quad (1.1)$$

$$Li_{1-x}CoO_2 + xLi^+ + xe^- \leftrightarrow LiCoO_2 \quad (1.2)$$

Graphite has a theoretical specific capacity of 372 mAh g^{-1}, most of which can be accessed, and exhibits a low average potential of ~0.15 V vs Li/Li^+ [15]. This low potential is one reason for graphite's continued success as anode material, as it exhibits the lowest average potential of any anode material besides lithium metal. LCO was the first successful cathode due to its moderate specific capacity and reaction potential, as well as its stability over many cycles[16–18]. However, LCO is less common in modern lithium-ion batteries due to the discovery of new materials with better electrochemical properties, as well as the ethical[19], environmental, and cost concerns of sourcing cobalt. Conventional liquid electrolytes typically use lithium salts dissolved in carbonate based solvents[20]. The chemistry of the electrolyte plays a critical role in determining cell performance due to its conductivity and effects on side reactions with the electrodes.

Battery researchers have strived over the past 30 years to discover new electrode materials with higher specific capacities and wider cell voltages. Numerous fundamental

and applied advances have been made for the anode, cathode, and electrolyte. Current state-of-the-art lithium-ion batteries are typically made using cathode materials such as $LiNi_xMn_yCo_zO_2$ (NMC) and $LiFePO_4$ (LFP)[12,21,22]. NMC is advantageous because of its high specific capacity and reaction potential[9]. NMC cathodes can be made using different compositions, such as $LiNi_{0.6}Mn_{0.2}Co_{0.2}O_2$ (NMC-622) and $LiNi_{0.8}Mn_{0.1}Co_{0.1}O_2$ (NMC-811)[23]. While decreasing the cobalt content has the advantage of increasing the specific capacity, removing cobalt tends to destabilize the crystal structure[21]. LFP has recently seen a rapid increase in market share, owing to its cheaper components, stable cyclability, and greater thermal stability compared to NMC[24]. The disadvantages of LFP are its lower specific capacity and cell voltage. Other cathodes with higher specific capacities, such as sulfur, have also been investigated, but have seen no practical application yet, primarily due to poor cyclability[25]. On the anode side, significant research has gone into using alloy materials like silicon because of their extremely high specific capacities[26–30], but these materials utilize different reaction mechanisms and are prone to large volume changes that damage the material. Modern anodes still typically use graphite, although other active additives such as silicon particles have been introduced to increase energy density[31].

Lithium metal has long been recognized as the ideal anode material because it has a very high specific capacity (3860 mAh g^{-1}) and the lowest reduction potential (-3.04 V vs SHE)[32,33]. In fact, lithium metal was one of the first materials to be tested during the infancy of commercial lithium-ion batteries, but failed due to poor cyclability and significant safety hazards[14,34]. However, the desire for a significant leap in energy density has revitalized research on lithium metal anodes over the past decade. Various strategies have been explored to improve the Coulombic efficiency and lifetime of lithium metal

anodes, including artificial coatings, 3D host structures, and electrolyte design[32]. Despite substantial progress in this field, these cells have continued to be challenged by phenomena such as dead lithium, poor solid electrolyte interphase (SEI) formation, and lithium dendrite growth[35–40]. Unfortunately, these effects are fundamentally tied to the nature of the interface between liquid electrolytes and lithium metal, which is inherently susceptible to the rearrangement of interfacial morphology and formation of dead lithium.

1.2 Solid-State Batteries

A solid-state battery replaces the liquid electrolyte with a solid material that has high ionic conductivity (~0.1-10 mS cm^{-1}) and low electronic conductivity (~10^{-6} mS cm^{-1})[41–43]. Solid-state electrolytes fundamentally alter the phenomena that occur within the battery due to their distinct mechanical properties. Liquid electrolytes flow and conform to the shape of the electrodes, wetting the surfaces of particles and easily establishing ion pathways. This behavior is in stark contrast to SSEs, which will not conform to the shape of the electrode on its own. Instead, pressure is often needed to alter the shape of the SSE and form a continuous interface with the electrodes[44–49]. The rigidity of SSEs also changes how forces generated by electrochemical reactions are transmitted throughout the cell, modifying the chemo-mechanical environment[50,51]. The unique mechanical properties of SSEs open new pathways to use electrode materials that are challenging to cycle with liquid electrolytes. In particular, the lithium metal anode has attracted great interest in the SSB community, as SSEs have been theorized to inhibit dendrite growth, reduce SEI formation, and eliminate the loss of dead lithium that contribute to significant capacity fade in liquid electrolytes[52,53].

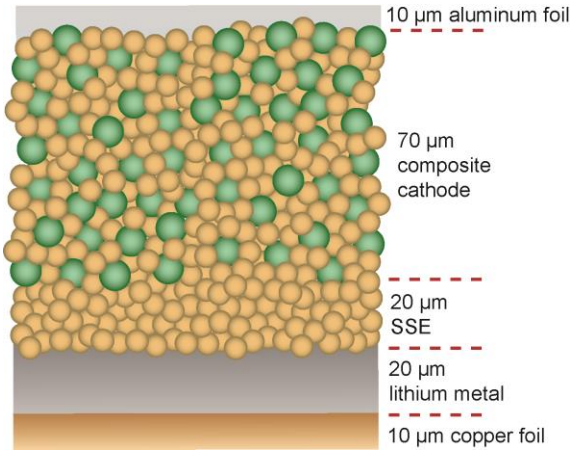

Figure 1.2. Schematic of a solid-state battery with a lithium anode and composite cathode.

In addition to enabling battery chemistries that are challenging to use in liquid electrolytes, SSBs may offer enhanced safety[41]. Conventional liquid electrolytes use highly flammable organic solvents, whereas many SSEs are much less flammable materials[42]. Additionally, inorganic SSEs are ceramics that are stable over a wide temperature range and may be able to operate safely at temperatures >100 °C with less risk of thermal runaway. Given the challenges that lithium-ion batteries have had with safety[54], and their increasing use in applications like electric vehicles where severe fires can be catastrophic, SSBs could be a practical route to mitigate safety risks.

The feasibility of SSBs hinges on being able to make a solid material that has exceptionally high ionic conductivity and sufficiently low electronic conductivity[55]. For many years, SSB research was relatively inactive due to the lack of good ionic conductors. However, many key breakthroughs have greatly expanded the number of materials with high ionic conductivity[56–59], allowing researchers to build SSBs with only minimal impedance resulting from the electrolyte layer. The greatest strides in conductivity have been made in the space of inorganic SSEs[42,43,55]. Important inorganic SSEs include the

oxide $Li_7La_3Zr_2O_{12}$ (LLZO, discovered in 2007)[56], the NASICON family of lithium conductors (1992)[60], the sulfide $Li_7P_3S_{11}$ (LPS, 2007)[57], and the halogenated argyrodite sulfides (2008)[59].

Polymer SSEs have seen less success due to their poor ionic conductivity at room temperature (0.001-0.01 mS cm^{-1}) and limited electrochemical stability at high potentials[61,62]. Most research has been focused on the poly(ethylene oxide) (PEO) system, which typically consists of dispersing lithium salts within a PEO matrix[63]. While PEO has been used in a large number of studies, its unsuitable electrochemical properties have driven researchers to develop novel polymer SSEs with higher conductivity and improved stability[64]. These recent results are promising because polymer electrolytes have many processing advantages over inorganic ceramic SSEs. Additionally, the softer mechanical properties of polymer electrolytes could be advantageous for maintaining interfacial contact with electrodes.

Since the discovery of numerous SSE materials with high ionic conductivity, the community's focus has shifted over the past 5 to 10 years to understand how to successfully interface SSEs with electrode materials[43,52,65–67]. This effort has proved to be challenging due to the nature of solid/solid interfaces and the electrochemical properties of both the SSE and electrode materials available. These interfacial challenges can be defined by three major phenomena: the electrochemical stability of electrode/SSE interfaces, contact loss at electrode/SSE interfaces, and non-uniform lithium metal deposition causing filament penetration through the SSE. Each of these phenomena on their own can be responsible for significantly limiting the performance of SSBs, and as such they must all be addressed to achieve a commercially viable SSB.

The first major challenge towards interfacing SSEs and electrodes is the electrochemical stability between these materials[65,68–86]. While an SSE material may have suitable ionic and electronic conductivities, these factors do not make them immune to reacting with the electrodes. Figure 1.3 shows the predicted electrochemical stability windows based on thermodynamic calculations for practical SSEs, represented by the green bars[80]. This figure shows that all practical SSEs reported in the literature to date exhibit some form of limited electrochemical stability; some SSEs are prone to reacting with anodes, some with cathodes, and others with both electrodes. For example, LLZO is remarkably stable close to the low reduction potential of lithium metal, but is vulnerable to oxidation by cathodes. On the other hand, LAGP exhibits poor stability against anodes but good stability against cathodes. Meanwhile, sulfide SSEs are predicted to be thermodynamically unstable against both anodes and cathodes.

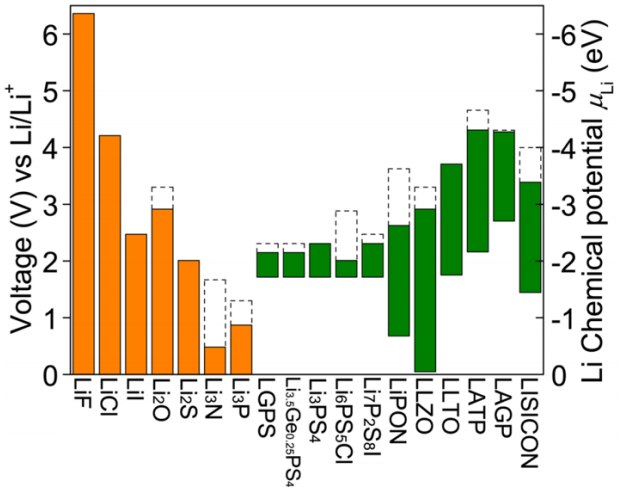

Figure 1.3. Thermodynamic predictions of the electrochemical stability windows of various SSEs based on DFT calculations. Materials are electrochemically stable at a given potential if it falls within the colored bar. Adapted with permission from reference[80]. Copyright 2015 American Chemical Society.

While an SSE may be thermodynamically unstable at an electrode's potential, that does not describe how severe the reaction will be. In general, the conductive properties of the decomposition products, known as the interphase, dictate how susceptible an SSE is to prolonged reactions with electrodes[87–93]. Interfaces with lithium metal anodes can be divided into three classes based on their conductive properties[87], as shown in Fig. 1.4. The first class (Fig. 1.4a) is a thermodynamically stable interface, where no interphase is formed. The second class describes interfaces where an interphase that can conduct both ions and electrons has formed (Fig. 1.4b). These mixed ionic-electronic conducting (MIEC) interphases are the most detrimental reactions, as electrons can be transported through the decomposed products and continue to electrochemically reduce the underlying pristine SSE, resulting in constant interphase formation. The third class of interfaces are those that form interphases that can conduct ions but not electrons (Fig. 1.4c). These interfaces can be described as kinetically stabilized or passivated interfaces.

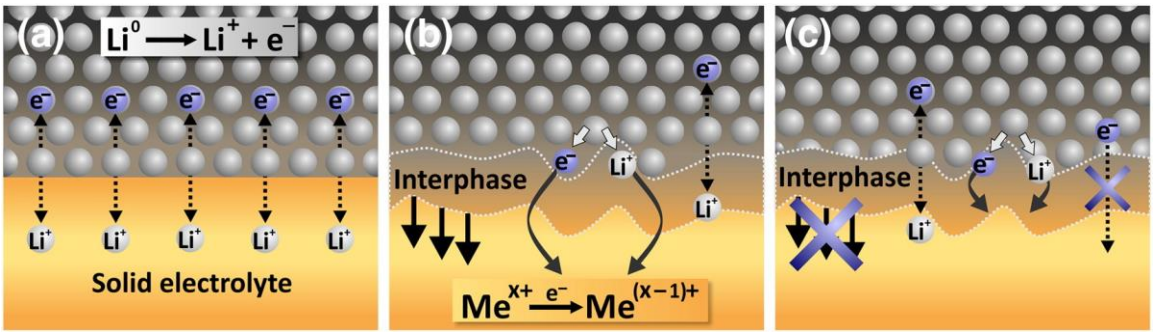

Figure 1.4. Schematic representation of the different types of interfacial stability at Li/SSE interfaces. **a)** A thermodynamically stable interface with no reaction. **b)** A reactive interface that decomposes into species with mixed conducting properties. **c)** An interface that reacts, but forms species that conduct ions and block electrons. Adapted with permission from refence[87]. Copyright 2015 Elsevier.

The divergent behavior dictated by interphase conductivity show that thermodynamic stability is not necessary to build viable Li/SSE interfaces, as long as the reactions that occur are self-passivating[78,89,94]. SSEs that form poor interphases cannot be considered as practical SSEs, since their continuous reactions will increase cell impedance and eventually deplete the total lithium reservoir in the cell. Fortunately, some SSEs that are thermodynamically unstable against lithium metal form passivating interfaces that make them viable candidates[78,88,89,93]. One example is the sulfide Li_6PS_5Cl (LPSC), which decomposes initially into products such as Li_3P, Li_2S, and LiCl[88], all of which exhibit low electronic conductivity.

The second challenge of interfacing SSEs with electrodes is to establish and maintain contact between these materials during cycling[44–46,85,95,96]. Interfacial contact is fundamentally important, as the interface allows for the transport of species between the SSE and electrode that is necessary to store energy. Reducing interfacial contact constricts the flow of species[52,96,97], resulting in regions with high local current densities that can exacerbate degradation. Since SSEs cannot flow and wet the surfaces of the electrodes to the same extent as a liquid, an emphasis must be placed on developing strategies to maintain contact. The most basic principle is apply a stack pressure to the cell during operation, which forces the solid materials to interface with each other[45–48]. However, applying a stack pressure does not guarantee that good contact will be created. It is also expected that stack pressures greater than a few MPa will be impractical at a commercial scale due to the costs of housing materials and loss in pack-level energy density[98–100].

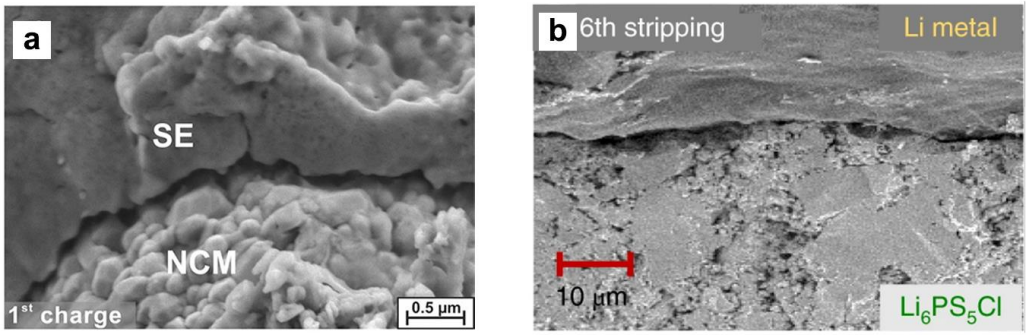

Figure 1.5. SEM images of contact loss at **a)** cathode/SSE and **b)** Li/SSE interfaces. Adapted with permission from references[44,85]. Copyright 2017 American Chemical Society and copyright 2019 Springer Nature.

Another challenge of maintaining interfacial contact is that it will evolve over time due to chemo-mechanical processes[44–46,85,96]. For example, cathode active particles are typically surrounded by an SSE matrix to establish ion conduction pathways. During cycling, the active particles expand and contract. If the surrounding materials cannot adjust to these volume changes, then interfacial contact will be lost and the cell impedance will increase (Fig. 1.5a)[85]. Contact evolution is also a significant challenge at Li/SSE interfaces. When lithium metal is stripped from the interface during discharge, a void is left in its place and interfacial contact is reduced (Fig. 1.5b)[44,46,96]. This void can be filled if lithium metal is driven back into it, which is possible via self-diffusion of lithium or mechanical deformation[44,46]. If the rate of lithium stripping is greater than the rate of lithium replenishment, voids will form faster than they can be filled. The permanent loss of interfacial contact increases the effective current density, promoting detrimental phenomena at the interface such as non-uniform lithium deposition during subsequent charges[44].

The third and final major challenge of interfacing SSEs with electrodes is that lithium metal can be deposited as filaments that penetrate through SSEs and create a short

circuit, killing the cell[101–106]. This behavior is unexpected, as the mechanical properties of many SSEs were thought to be sufficiently rigid to block lithium metal penetration during plating[107]. However, numerous studies have confirmed the existence of lithium metal penetration in oxide, sulfide, and polymer SSEs. This phenomenon is believed to occur above a certain critical overpotential that is sufficiently high enough to nucleate and grow a non-uniform lithium filament[108]. It is important to note that this interfacial challenge is most relevant for SSBs using a lithium metal anode, as these cells function by plating lithium metal during charging. However, lithium plating can occur even with other anode materials when the kinetics become too fast.

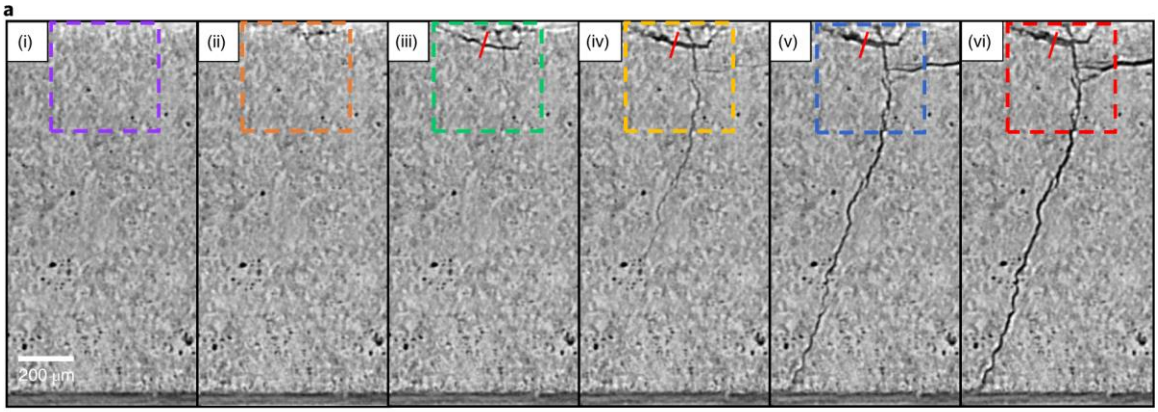

Figure 1.6. X-ray tomography images taken from a lithium metal SSB during the formation of a short circuit. After initial cracking near the interface (top of image), a vertical crack is formed and propagates across the electrolyte, followed by lithium metal deposition into the crack. Adapted with permission from reference[109]. Copyright 2021 Springer Nature.

Numerous mechanisms have been suggested for causing lithium penetration through SSEs, such as crack initiation and growth[105,109–112], surface defects[105], grain boundaries[101,113], microstructural inhomogeneities, and electronic conductivity[108]. Recently, X-ray tomography studies have provided new insight into the mechanisms of

lithium penetration through sulfide SSEs (Fig. 1.6)[109–111]. An *operando* experiment revealed that cracks initiate and propagate across the electrolyte first, followed by lithium deposition into the crack[109]. This behavior is counter to some previous theories, which proposed that lithium filaments drove crack formation from the tip of the filament[105]. It is likely that filament growth is a result of the interplay between all of these factors. Lithium penetration will also depend on the type of SSE being studied. For example, oxides have different mechanical and microstructural properties than sulfides and polymers, which could cause different mechanisms to dominate.

Although lithium filaments grow during plating, recent work has shown that the voids formed during stripping are often responsible for this behavior when cycling[44–46]. When plating begins at a stripped interface, it is more likely that a lithium filament will grow because of the higher effective current density caused by having lower contact area. Therefore, preventing lithium penetration requires an understanding of both the plating and stripping phases of cycling. These observations show that the mechanical dynamics that take place at Li/SSE interfaces are complex and play a major role in how cell failure occurs.

1.3 Experimental Materials Background

1.3.1 NASICON Solid-State Electrolytes

The NASICON family of SSEs was originally discovered for sodium-ion conductors with the general formula $Na_{1+x}Zr_2Si_{2-x}P_xO_{12}$ ($0 \leq x \leq 3$)[114], and as such the NASICON abbreviation is derived from the name “Na superionic conductor”. However, isostructural lithium analogues have since been discovered and studied in detail due to their relatively high ionic conductivity (> 0.1 mS cm^{-1}). The two most common lithium

conductors in the NASICON family are $Li_{1+x}Al_xTi_{2-x}(PO_4)_3$ and $Li_{1+x}Al_xGe_{2-x}(PO_4)_3$ (LAGP)[55,115]. Both materials are commonly used in their crystalline form. They typically exhibit ionic conductivities between 0.2-0.5 mS cm^{-1}, although values up to 1 mS cm^{-1} have been achieved[55,115].

NASICON electrolytes can be fabricated through a number of different routes. These methods can be roughly divided into solid-phase and liquid-phase[115]. A simple solid-phase route is solid-state synthesis, which involves mixing the chemical precursors via ball milling and then heating the powder to drive a solid-state reaction in the mixture[116]. One challenge with this method is lithium evaporation at high temperatures, which is typically compensated for by including additional lithium sources. Another solid-phase method is melt quenching, where the precursors are melting at extremely high temperatures (~1500 °C) and then quenched to form an amorphous glass[117]. While the product is in an amorphous state, it can be further heated to achieve the crystalline phase. Lastly, NASICONs can be fabricated using fast sintering techniques, such as spark plasma sintering, which typically use electricity to generate very large heating rates[118].

The most common liquid-phase synthesis used for NASICONs is the sol-gel method[115,119,120]. This process starts by forming a colloidal solution of the precursors, which is then heated at low temperatures (~100 °C) until a gel forms. After heat treatment steps, a crystalline powder with small particle size is yielded. This powder can then be compressed into a pellet and sintered at ~800-1000 °C to obtain a dense ceramic sample. An advantage of the sol-gel procedure is that it can be done at much lower temperatures and shorter times than the solid-phase methods. Sol-gel synthesis can also obtain small

particle sizes less than 1 μm[115]. Comparable ionic conductivities can be obtained for all of the synthesis routes discussed here.

The thermodynamically predicted electrochemical stability windows for LAGP is shown in Fig. 1.3. In general, the NASICON family of lithium conductors exhibits excellent stability at high reduction potentials, making them suitable for applications with cathode materials[79]. However, they have poor stability at low potentials[79,80], and have been shown to react with anode materials that operate in this regime, such as lithium metal. *In situ* X-ray photoelectron spectroscopy (XPS) measurements taken during the chemical reaction between LAGP and lithium metal revealed that Ge^{4+} is reduced to Ge^{0}, suggesting the presence of Li-Ge alloys in the interphase generated by this reaction[77,91]. As discussed earlier, the presence of MIEC interphases can enable continuous decomposition of the SSE due to their ability to transport electrons to the interface with the remaining pristine SSE. The instability of the chemical reaction created by contacting lithium metal and LAGP has also been shown to cause the brittle oxide to fracture[77,116]. Furthermore, heating these two materials together near the melting point of lithium metal (~185 °C) can cause a spontaneous and dramatic thermal runaway reaction to occur, despite LAGP's excellent thermal stability[116].

1.3.2 Thiophosphate Solid-State Electrolytes

The family of thiophosphate SSEs are inorganic materials containing sulfur and phosphorous[55], and are typically referred to simply as sulfide SSEs. These materials are known for having high ionic conductivity, which can often be accessed without high temperature sintering after the annealing process is completed[121]. This behavior is in

contrast to oxide SSEs, which generally require a sintering step to densify the SSE. One reason for this difference is that sulfides exhibit softer mechanical properties than oxides[122], and can be densified to greater extents when cold pressing pellets.

Sulfide SSEs are traditionally synthesized through one of two routes: a solid-state synthesis or a liquid-phase synthesis[121]. The solid-state synthesis involves ball milling precursors for many hours, followed by annealing at moderate temperatures (~300-600 °C) to access the correct crystalline phase[57,58,123,124]. Liquid-phase synthesis is more practical for scaled up production of SSEs, as it involves mixing precursors in solvents followed by heating at moderate temperatures (~100-300 °C)[125]. However, liquid-phase synthesis can be challenging due to the poor compatibility of sulfides with many solvents.

The $Li_{10}GeP_2S_{12}$ (LGPS) family of sulfide SSEs was discovered in 2011 and exhibit an extraordinarily high conductivity of ~10 mS cm^{-1}, which is on par with the conductivity of many liquid electrolytes[58]. Later work showed that the Ge^{4+} ions can be substituted for Sn^{4+} to form $Li_{10}SnP_2S_{12}$ (LSPS), which was done to reduce material costs[126]. Interestingly, LSPS has lower ionic conductivity (~3 mS cm^{-1}), despite Sn^{4+} ions having a larger radius than Ge^{4+} ions. This result was somewhat unexpected, since it was thought that the larger Sn^{4+} ions would create wider pathways for lithium diffusion[55]. A further study of the structural dynamics in the LGPS family revealed that the addition of Sn creates diffusion bottlenecks along the z-direction and also drives stronger bonding between Li^+ and S^{2-} that increases the activation barrier[127].

Although the LGPS family of sulfides has high ionic conductivity, these materials are electrochemically unstable against both lithium metal and cathodes[80]. The predicted

stability windows for LGPS is shown in Figure 1.3. This plot shows that LGPS has a very narrow range of thermodynamic stability, and will decompose to some extent against lithium metal. Chemical decomposition has been confirmed experimentally for both LGPS and LSPS through XPS measurements[90,128]. Interphase formation is expected to be severe and continuous due to the formation of lithium alloy compounds in the interphase, similar to the behavior of LAGP. Therefore, the LGPS family of sulfides is incompatible with lithium metal without steps to modify the interface. Additionally, it is necessary to coat cathode particles with protective oxides that help stabilize the cathode/LGPS interface[82]. Without these coatings, the cell cannot be cycled for long due to high interfacial impedance.

While the LGPS family of sulfides initially attracted interest because of high conductivity, their poor electrochemical stability has limited their practical application. Fortunately, there are other sulfide materials that have been found to exhibit improved stability against lithium metal anodes. One popular class is the argyrodite sulfide, which is typically halogenated and has the general composition Li_6PS_5X (X = Cl, Br, I)[55,59]. The most widely used material from this family is Li_6PS_5Cl, which has an ionic conductivity between 1-5 mS cm^{-1}. While LPSC is not initially stable against lithium metal (Fig. 1.3)[80], it decomposes into species that do not conduct electrons and becomes passivated against further decomposition[88,129]. This phenomenon allows LPSC to be stably cycled with lithium metal anodes at high current densities for thousands of hours[130]. However, this stability comes with caveat that LPSC is susceptible to non-uniform lithium metal deposition that grows filaments through the SSE, which can kill the cell by forming a short circuit[44,47,109,130].

CHAPTER 2. EXPERIMENTAL METHODS

This chapter summarizes the experimental methods used to collect data for this dissertation. This summary includes how SSB materials were synthesized and processed, the general assembly procedure used to build SSBs, the electrochemical methods used to test different SSB configurations, and the characterization techniques used to probe SSBs before, during, and after operation.

2.1 Materials Synthesis and Processing

The NASICON type SSE $Li_{1.4}Al_{0.4}Ge_{1.6}(PO_4)_3$ was synthesized using a sol-gel method following existing procedures[119,120]. In the first step, a solution of 0.2 M citric acid was mixed with germanium ethoxide in a round bottom flask at 80 °C for 20 hours to create a homogenous solution. The amount of germanium ethoxide added was enough to create a concentration of 0.8 M. The remaining precursors of lithium nitrate, aluminum nitrate nonahydrate, and ammonium phosphate monobasic were then added in stoichiometric amounts and mixed for 30 minutes. Ethylene glycol with a 1:1 molar ratio to the citric acid was pipetted into the solution and the temperature increased to 120 °C. During this step, the water was evaporated and the solution began to thicken into a gel and then burned to form a brown powder. The powder was ground up in a mortar and pestle, and heated in a tube furnace in air at 500 °C for 4 h and 800 °C for 5 h. The resulting white powder was then ground again and pressed into 10 mm diameter pellets with a thickness of ~1 mm and sintered in air at 900 °C for 11 hours.

The sulfide electrolytes LSPS and LPSC were purchased from NEI Corporation. LSPS was used as-received without any modifications. LPSC was modified to alter the particle size and improve the quality of pressed pellets by hand grinding ~600 mg of LPSC in a mortar and pestle for ~20 minutes.

Polycrystalline $LiNi_{0.8}Mn_{0.1}Co_{0.1}O_2$ (NMC-811) and single crystal $LiNi_{0.6}Mn_{0.2}Co_{0.2}O_2$ (sc-NMC-622) were purchased from NEI Corporation and MSE Supplies, respectively. Due to the poor electrochemical stability of sulfide SSEs against cathodes, it was necessary to coat cathode particles with a passivating $LiNb_{0.5}Ta_{0.5}O_3$ (LNTO) coating. The LNTO coating was added by dissolving stoichiometric amounts of lithium acetate, niobium (V) ethoxide, and tantalum butoxide in dry ethanol and mixing for 4 hours. 1 mL of the prepared solution was then mixed with 2g of cathode material, dried in a vacuum oven overnight, and annealed at 450 °C for 1 min in air. After coating, composite cathodes with 70/27.5/2.5 ratios of active material / LPSC / conductive carbon were mixed using a planetary ball mill (Fritsch Pulverisette 7) with a milling speed of 140 RPM for 30 minutes.

2.2 Solid-State Battery Assembly

SSBs with oxide SSEs, such as LAGP, were assembled inside an Ar filled glovebox using 2032 coin cell housings. Symmetric Li/LAGP/Li cells were made by punching out two ¼'' discs of clean lithium metal and compressing the discs onto each face of a sintered LAGP pellet by hand. The Li/LAGP/Li stack was sandwiched between two steel spacers, and conductive foam was added behind each spacer to help apply a uniform pressure across

the sample. The stack pressure applied during cell operation was created when the coin cell was crimped at 500 psi to form an air tight seal.

Custom cell housings were designed to build SSBs using sulfide SSEs. A schematic and image of this housing is shown in Figure 2.1. The working principle of the cell housing was to apply stack pressure by tightening four nuts, causing the two steel plates to compress on the cell stack. Using an accurate digital torque wrench and a calibrated force sensor, the stack pressure could be reliably controlled to approximately ±1 MPa. The housing consisted of 3 main components – a polyether ether ketone (PEEK) die where the materials were compressed, titanium current collector rods that were inserted into the die, and steel plates that were used to apply pressure to the SSB during electrochemical experiments. PEEK was chosen as the die material because it is an insulator and does not react with lithium metal. The diameter of the PEEK die hole was 10 mm for all cells used in this format. The current collectors were made out of titanium due to the high applied pressure during pellet fabrication (>300 MPa), which required a high strength material to prevent plastic deformation over the lifetime of the components. The rod diameters were machined to slip smoothly through die hole without getting stuck or being too loose.

A modified version of the sulfide cell housing was designed to include a sealing mechanism that allowed cells to be cycled outside of the glovebox, as shown in Figure 2.1c. The general principles of the original cell housing were used, but an o-ring and compression plate with bolt holes were added to each titanium rod. A seal was formed by bolting the two compression plates together, which applied pressure to each o-ring, causing them to compress and form a seal. The quality of this mechanism was tested by sealing pristine lithium metal inside the cell and letting it sit outside of the glovebox for a day.

Since lithium metal rapidly reacts with compounds such as O_2, N_2, and H_2O, the color changes associated with these reactions on the surface of lithium metal would indicate a poor seal. Testing showed that the lithium metal remained visibly pristine, suggesting a sufficient seal was formed. Additionally, cells were successfully cycled in ambient atmosphere for weeks without abnormal degradation. This design allowed for some types of SSBs to be cycled outside in controlled temperature chambers.

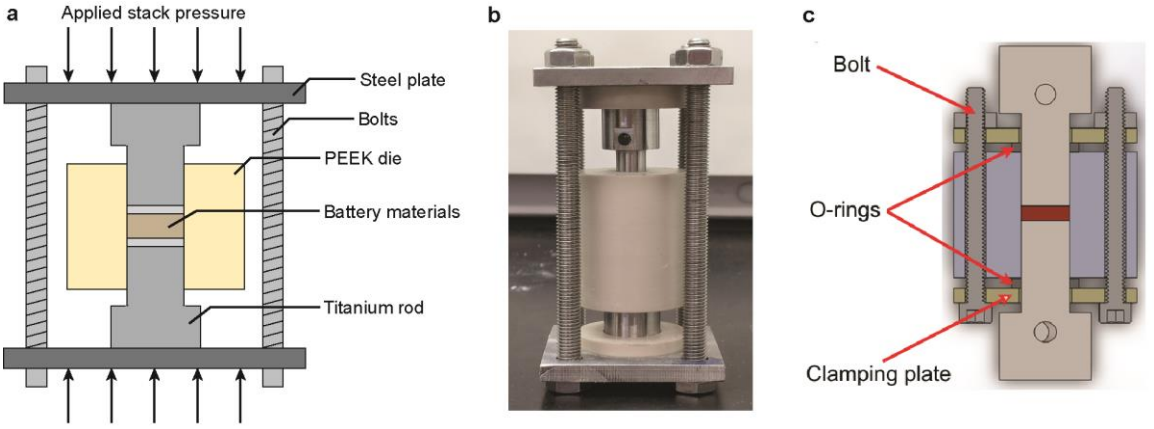

Figure 2.1. a) Schematic and **b)** photo of the cell housing design used to make sulfide-based SSBs. The component dimensions could be altered depending on the user's constraints. In this thesis, all cell housings with this design had an inner die diameter of 10 mm. **c)** Schematic of the sealing mechanism added to some cell housings.

Sulfide-based SSBs were assembled inside an Ar filled glovebox using the following general procedure. First, one rod was inserted into the die, and the necessary powders (such as the sulfide SSE or electrode materials) were poured in and spread around to form a uniform powder layer. The other rod was then added and the stack was placed in a uniaxial press to compress the powders under high pressures (typically ~375 MPa). Foils, such as lithium metal or copper, were then added to the cell after this pressing step. The copper foil used was 10 µm thick and purchased from MTI. Lithium metal foil was

prepared by cleaning the surface with Teflon blocks until the metal was shiny, flattened to the desired thickness (typically ~300 μm), and then cleaned again with a toothbrush. After adding all materials, the cell was compressed by the steel plates at the desired stack pressure (typically ~15 MPa). This stack pressure was applied throughout cycling to maintain contact between the solid materials. Cells using the original housing design were cycled inside the glovebox because they were not sealed and contained air sensitive materials.

2.3 Electrochemistry

A variety of electrochemical tests were used to study the behavior of SSBs, and the methods chosen depended on the cell architecture. In this thesis, three broad configurations were investigated: symmetric cells, half cells, and full cells. Each general configuration used different electrochemical procedures for testing.

A symmetric cell uses the same material for both electrodes. The most common type of symmetric cell is the Li/electrolyte/Li cell, which is frequently used by researchers studying lithium metal anodes with either liquid electrolytes or SSEs. The primary benefit of using a symmetric cell is that it enables studying the behavior of Li/electrolyte interfaces without the convoluted effects that a cathode material can introduce. A typical electrochemical experiment with a symmetric cell involves applying a positive current for a specified amount of time or capacity, and then switching the current to be negative for the same duration. This process is then repeated to cycle the symmetric cell. In theory, the voltage of a symmetric cell should be 0 V since there is no potential difference between the two electrodes. However, the application of a current inherently involves inefficiencies that cause the voltage to deviate from 0 V during operation.

Half cell configurations use a lithium metal counter electrode and a different material as the working electrode. The role of the lithium electrode is to act as a supply of lithium ions while maintaining a relatively constant potential. Half cells are traditionally used when studying novel anode materials. When the working electrode is a material that does not initially contain lithium, such as a silicon anode or a copper substrate, the cell is tested by first applying a current that drives lithium ions to the working electrode. This process is limited by either a specified voltage or time. The current is then reversed, and lithium is extracted from the working electrode. This process is repeated many times to cycle the cell. In this thesis, the only cells using this configuration were the anode-free half cells discussed in Chapter 6. It is important to note that anode-free Cu/SSE/Li cells only represented half cells in the assembled state, as they effectively became symmetric cells once lithium was plated onto copper during charging.

A full cell configuration incorporates both cathode and anode materials, and best represents a lab prototype of a commercial battery. Because of the high potential of the cathode and low potential of the anode, the measured cell voltage is much larger than symmetric and half cells. The voltage of a full cell will typically be somewhere between 2.0-4.5 V depending on the cathode and anode materials used. Most full cells are assembled in the discharged state, as the pristine cathode is usually pre-lithiated. Full cells are thus normally charged first. During this process, the voltage increases over time until reaching a specified upper voltage limit. The full cell is then discharged down to a lower voltage limit, and the process is repeated for many cycles. Choosing appropriate voltage limits is critical for maximizing cell lifetime, as negative effects can occur if the limits are set too high or low.

Electrochemical impedance spectroscopy (EIS) was used to probe the impedance of SSBs. EIS applies a small sinusoidal input signal (either a current or voltage) with a given amplitude and frequency to an electrochemical device and measures the resulting AC signal (a voltage or current)[131,132]. The output signal has the same frequency as the input, but can have a different amplitude and may also be out of phase. During an EIS experiment, the input frequency is swept across many values while the output signal is measured. A fast Fourier transform is then applied to convert the signal information in the time domain to the frequency domain. A comparison of the transformed input and output signals yields the complex impedance at a given frequency, as well as the phase angle.

The magnitude of the complex impedance and the phase angle can be used to determine the real and imaginary components of the impedance at a given frequency. These values form the basis of the Nyquist plot by plotting the real and imaginary pairs for every frequency value[131,132]. An example Nyquist plot is shown in Fig. 2.2; the data points on the left are taken at high frequencies (~1 MHz) and decrease in frequency as the plot moves to the right (until ~1 Hz). Nyquist plots can be fit using equivalent circuit models that represent the EIS data as components in a circuit[131,132]. For example, the plot shown can be modeled as a resistor in series with a capacitor and resistor that are in parallel with each other. These components represent the electrochemical behavior of the battery, such as the charge transfer resistance. Therefore, EIS can directly quantify different electrochemical processes and how they impact cell impedance.

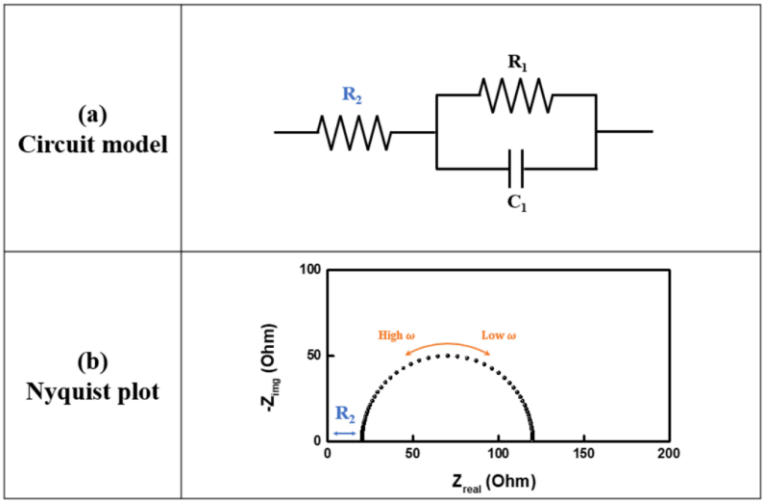

Figure 2.2. An example of a Nyquist plot and its equivalent circuit model. Adapted with permission from reference[132]. Copyright 2020 Korean Electrochemical Society.

EIS has been used to study many types of electrochemical phenomenon in batteries[131,132]. One common application is to measure the conductivity of SSEs. This experiment is set up by placing blocking electrodes, such as gold, on both faces of the SSE[131,133,134]. EIS data is typically collected over a frequency range between ~1-10 MHz and ~1 Hz. Depending on the SSE studied, different features will be present in the Nyquist plot, such as the grain boundary impedance and the bulk impedance. The ionic conductivity of the material can be calculated using these impedances and the known sample geometry from Eq. 2.1, where l is the length of the sample, A is the area of the sample (based on the blocking electrodes), and R is the total impedance. EIS can also be used to probe how impedances of individual processes change throughout cycling, since these processes can have distinct features in a Nyquist plot. One example of this is the charge transfer impedance at an interface, which may evolve over time due to changes in interfacial structure, composition, morphology, etc[131,132].

$$\sigma = \frac{l}{R * A} \tag{2.1}$$

The conductivities of SSEs studied in this thesis were measured using EIS. For oxides, such as LAGP, a gold colloidal paste was painted onto each side of a sintered SSE pellet. The samples were then heat treated at 700 °C using a 1 hour ramp and 1 hour dwell time to evaporate the solvents and cure the gold. The coated samples were placed between clips and EIS measurements were taken over a frequency range of 3 MHz down to 1 Hz using an input voltage signal with an amplitude of 10 mV. For sulfides, such as LSPS and LPSC, gold foils were cold pressed onto each side of a pellet. The stack pressure was held at ~15 MPa during EIS measurements to ensure good contact between the SSE and gold foils. EIS was also used to probe the impedance of SSBs at different stages of the cells life. The same measurement procedure was carried out on cells assembled using the methods described in Chapter 2.2.

2.4 Advanced Characterization

2.4.1 X-Ray Tomography

X-ray tomography is an imaging technique that uses X-rays to penetrate a sample and recreate an image of the 3D space[135]. A schematic of a typical X-ray tomography instrument is shown in Figure 2.3. To collect data, the sample is rotated, typically 180°, while X-rays are transmitted through the sample. The full rotation range is broken down into a discrete number of angles, and at each angle, X-rays that pass through the sample

are collected by a scintillator that converts them into visible light, which is then recorded by a detector as an image. This projection image provides information about the interactions between the X-rays and the sample at a given angle. After recording projections at many angles (a typical experiment consists of ~1000 projection images), the data are processed using a reconstruction algorithm to display the information in real 3D space as a stack of reconstructed 2D images[136]. Each 2D image displays a cross-section of the sample in a particular orientation in space. Because a reconstructed image is made up of individual pixels, the size of each pixel represents an amount of length in real space.

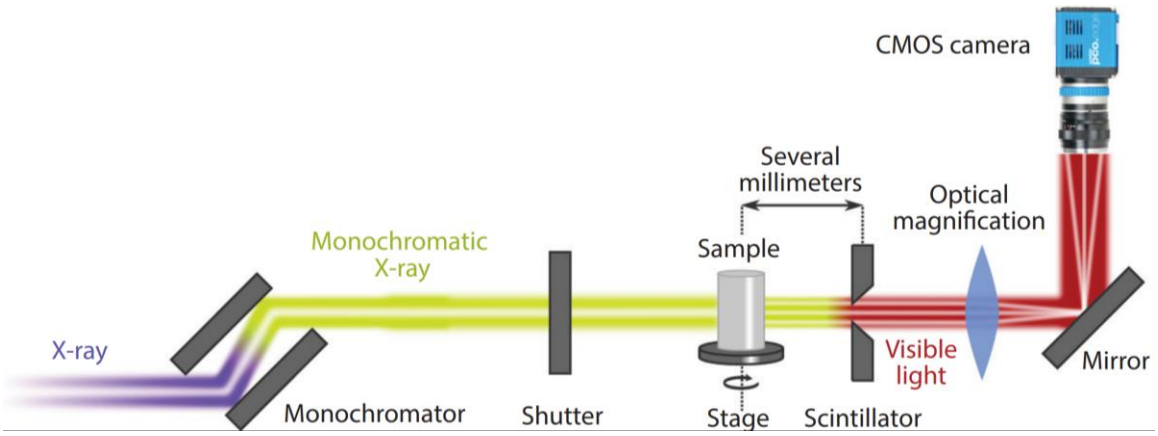

Figure 2.3. Schematic of an X-ray tomography instrument. When the shutter is open, X-rays are passed through the sample, with some being transmitted and others being absorbed. The transmitted X-rays continue on and pass through a scintillator, which converts them into visible light. An optical system is then used to collect the light and transmit it onto a detector. Adapted with permission from reference[135]. Copyright 2017 Annual Reviews.

There are two general ways to obtain X-ray tomography data: lab scale instruments and synchrotrons[135,137]. Lab scale X-ray tomography instruments are commonly found on university campuses, making them more accessible to a wider range of researchers. Modern instruments can achieve high spatial resolution (~1 μm), enabling the detection of many

features in the sample[137]. However, getting high resolution data with lab scale instruments is typically constrained by long scan times on the order of hours. On the other hand, the high flux of X-rays at a synchrotron can be used to generate high resolution data sets on the order of minutes. Using X-rays generated at a synchrotron are advantageous for many other reasons, such as better control of photon energy and the use of monochromatic X-rays[138]. However, there are only a limited number of beamlines that can do X-ray tomography across the world, and generally involve a lengthy user proposal process to get access for experiments.

The experiments in Chapter 4 were conducted at Argonne National Laboratory's synchrotron, the Advanced Photon Source. The beamline used was 2-BM, which is dedicated to X-ray microtomography and has a number of tools to assist *in situ* and *operando* data collection. Monochromatic X-rays with an energy of 28 keV were chosen to maximize transmission in our samples on the basis of attenuation length calculations. Fifteen hundred projections were taken with an exposure time of 210 ms while rotating the sample through 180°. An Oryx 5.0 MP Mono 10GigE detector and a ×2 magnification lens were used for the optics in this setup. The sample-to-detector distance for all experiments was 100 mm. A voxel size of 1.7 μm was achieved while fitting the entire sample within the field of view of ~$4.2 \times 1.4\ mm^2$. The time required to complete a scan under these conditions was approximately 7 min. The raw data were reconstructed with TomoPy using the Gridrec method.

A specialized SSB cell was designed to meet the experimental constraints of *operando* X-ray tomography experiments. The key constraints were 1) a suitable housing material that was electronically insulating, durable, and X-ray transparent 2) a small sample

size to allow for X-ray transmission 3) maintain an air-tight seal in ambient atmosphere to preserve air sensitive materials 4) apply stack pressure to the battery materials to enable cyclability.

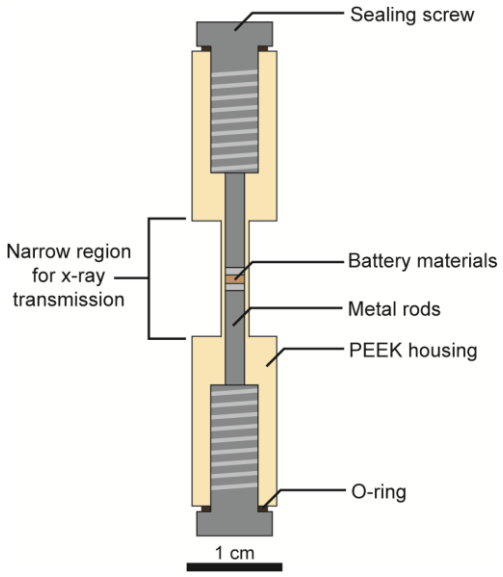

Figure 2.4. Schematic of the cell housing designed for *operando* X-ray tomography experiments. Screws and rods applied pressure to the battery materials, while a seal was simultaneously formed by compressing o-rings with the screw heads. The materials were housed in a narrower region of the cell to reduce X-ray absorption by other components.

A schematic of the cell design chosen to meet these constraints is shown in Figure 2.4. The battery materials sat in the middle of the cell, where the inner diameter was 2 mm and the wall thickness was approximately 1 mm. This small size allowed for excellent transmission for many battery materials of interest. Additionally, it allowed for the entire cell to be fit into the field of view of the detector, which enabled observation of the entire SSB in three dimensions. The wider barrels on each end of the cell allowed for screws to thread into the cell and apply a stack pressure. The sealing mechanism was controlled by compressing an o-ring underneath the screw head. To ensure that the sealing and pressure

constraints were met, spacers were added inside the cell to appropriately control the position of the screw. This method ensured that the o-ring was compressed by the screw head while the end of the screw applied pressure to the spacers.

X-ray tomography cells were assembled using the following general procedure. First, a rod was inserted into the cell's 2 mm diameter hole. The length of the rod was machined to ensure the battery materials would be positioned within the thinner part of the cell. The desired powders were then poured in and another rod was inserted on top. The two rods were compressed between two steel plates at the desired pressure (typically 225 MPa), which was calibrated using a force sensor. The pressure was then released and the rods removed. Any additional battery materials, such as lithium metal foil, were then inserted, followed by 2 mm diameter rods on each side with an approximate length of 0.4 inches each. Conductive spacers were added on each side until an adequate height was reached for the screw to simultaneously seal the cell and apply the stack pressure.

Segmentation procedures were developed to identify what phase each pixel in a 2D image belonged to. Repeating this process for every 2D image contained in the 3D image stack would yield a 3D volume of the segmented phase. Most of the segmentation in Chapter 4 was done using MATLAB. A schematic representation of the procedure used to segment lithium metal electrodes is shown in Fig. 2.5. The algorithm started by sequentially traversing each pixel column in a reconstructed 2D image slice. The intensity profile of the pixels along each column was used to identify the location of lithium metal, which exhibited an intensity below the SSE and the steel rods. First, the upper boundary was defined based on the reduction in intensity at the interface between the steel current collector and lithium electrode (see blue dashed box labeled 1 in Fig. 2.5). Second, the

algorithm continued to recognize pixels along the column as lithium if their intensity was below the specified intensity cutoff (see blue dashed box labeled 2 of the intensity profile). Third, the lower boundary of lithium was identified when the average value of five adjacent pixels in the column was above a threshold value typical of the SSE. This procedure was repeated for every column in the image slice, and then extended to every image slice in the stack. The final result was the segmented lithium electrode volume consisting of many segmented 2D slices.

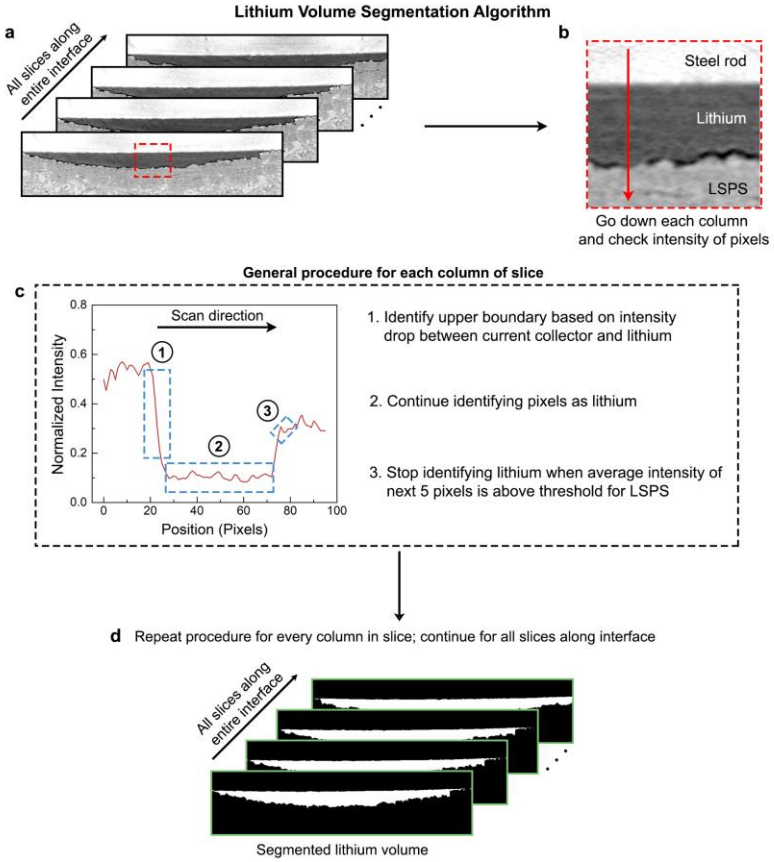

Figure 2.5. Visualization of the segmentation procedure used to identify lithium metal electrodes in an X-ray tomography dataset.

The only phase that did not use a custom segmentation routine was the interphase, due to its subtle contrast differences that were difficult to assign rules to identify. Instead, a machine learning tool built into the FIJI image processing package known as WEKA (Waikato Environment for Knowledge Analysis) was used to segment the interphase. The WEKA software used manually identified inputs of different phases to train a machine learning algorithm, which could then classify entire images based on the trained data. The interphase segmentation was only performed on a smaller 680 × 680 × 340 μm subvolume due to the difficulty of identifying the interphase near the edges of the cell.

2.4.2 Electron Microscopy

Electron microscopy was developed to image samples with much higher resolution than what is possible with optical microscopy[139]. The resolving power limit of a microscope can be described by the Rayleigh criterion (Eq. 2.2), which is effectively the ratio of the source's wavelength (λ) and aperture size (d). The wavelength of an electron is significantly smaller than visible light, enabling electron microscopes to have greater resolving power.

$$\theta \approx 1.22\frac{\lambda}{d} \tag{2.2}$$

An electron microscope generates electrons using an electron gun, which are then accelerated towards the sample by applying a voltage[139]. Many different interactions occur between the electrons and sample that can be leveraged to extract information about the material being studied. If the sample is thin, then electrons can transmit through the material and be detected, which is the basis for transmission electron microscopy (TEM).

Secondary electrons can be produced when the electron beam ionizes the material, and are commonly used to generate images in scanning electron microscopy (SEM). Incident electrons can also be reflected off of the sample; these backscattered electrons can be used to form images, and contain information about the atomic number of the material. In addition to electron signals, other signals such as X-rays can be generated and detected. A common signal used is the characteristic X-ray, which is the basis for energy-dispersive X-ray spectroscopy (EDS) and allows for analysis of composition.

TEM can achieve spatial resolution on the order of 0.1 nm when using state-of-the-art instruments[140]. In addition to imaging, diffraction patterns can be collected from transmitted electrons that have been scattered to identify the sample's crystal structure. A number of specialized TEM holders have been developed to conduct *in situ* experiments during imaging[141]. Capabilities include *in situ* sample heating, gas/liquid flow, and electrical biasing. *In situ* biasing has been particularly useful for studying the reaction dynamics of battery materials at the nanoscale[142]. These experiments are typically done by manipulating a probe with an ion source attached, such as lithium metal, and using the electrical bias to drive ions into the battery material mounted in the TEM holder (Fig. 2.6)[77,143–145]. One challenge of TEM is that samples must be thin (~100 nm or less) to achieve sufficient transmission. This requirement can make sample prep time intensive and may require specialized and expensive equipment to thin the sample depending on the material being studied.

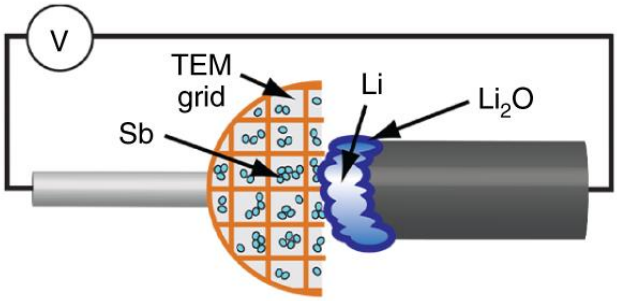

Figure 2.6. Schematic of an *in situ* TEM experiment. A specialized holder allows for a small probe to be manipulated with a controller (right). An ion source, such as lithium metal, is added to this probe and then manipulated to contact the battery material that is mounted in the holder (left). Adapted with permission from reference[144]. Copyright 2020 Springer Nature.

SEM has limited spatial resolution compared to TEM, but has the advantage of being able to image many types of samples because the electrons do not need to transmit through the sample. The electron beam is scanned across the sample, which generates secondary and backscattered electrons that can be collected by a detector and used to form an image. A typical achievable resolution is on the order of ~100 nm or less. SEM is used to provide information about sample topography and morphology at length scales that are difficult to resolve with an optical microscope. They can also be paired with other instruments and detectors, such as a focused ion beam (FIB) system or EDS detector, to achieve multi-functionality.

This dissertation used both SEM and TEM to characterize materials. SEM was used in Chapters 3-6 to characterize sample morphology and composition. Most samples were probed using a Zeiss Ultra60 FE-SEM operating between 5 and 10 kV. Samples were prepared by mounting them to aluminum SEM stubs with carbon tape. For cross-sectional imaging, the samples were fabricated by either fracturing the material or cutting through it

with a scalpel. The *in situ* TEM experiments in Chapter 3 were conducted using a 300 kV FEI Titan S aberration-corrected TEM and a 300 kV FEI Tecnai F30 TEM. A specialized FEI NanoEx 3D TEM specimen holder was used that allowed for the physical manipulation of samples and electrical biasing via a piezoelectrically-controlled metallic probe. LAGP particles were attached to the tip of sharpened tungsten probes using conductive epoxy and placed in the sample holder. Lithium metal was attached to the tip of another probe inside of an Ar filled glovebox and placed in the holder. The holder was then quickly inserted into the TEM column to minimize air exposure.

2.4.3 Focused-Ion Beam Milling

Focused-ion beam technology is used throughout materials science to mill through samples in controlled patterns and with nanoscale precision[146]. A conventional FIB uses a gallium metal source and large electric field to ionize gallium atoms and accelerate them towards the sample. The impact of these ions against the material ejects local atoms; as the ion beam is rasterized across the sample, a milling pattern is created. Repeating this milling pattern causes deeper trenches to be formed over time. A modern FIB using a gallium source can cut ~30 μm by 30 μm by 30 μm trenches in hours or less depending on the magnitude of beam current used. FIB instruments are typically paired with an SEM column to image the sample throughout the milling process.

One challenge of using FIB to characterize batteries is that some materials are sensitive to damage from interactions with the ion beam[147]. This is especially true for lithium metal anodes, which are known to alloy with gallium[148]. The damage induced by gallium FIB sources has been well documented in literature. Cryogenic milling has been

explored as a solution to this problem, since cooling materials to extremely low temperatures reduces interactions with the beam[147,149]. Figure 2.7 shows cross-sections of lithium metal milled at different temperatures[147]. At room temperature, the cross-section was artificially porous due to beam damage. At temperatures below -100 °C, there was a clear transition to a smooth lithium morphology, indicating that beam damage had been greatly reduced. These images highlight the general problem of FIB milling samples that are beam sensitive, as the morphology after milling may be artificial, leading to inaccurate conclusions about the materials being studied.

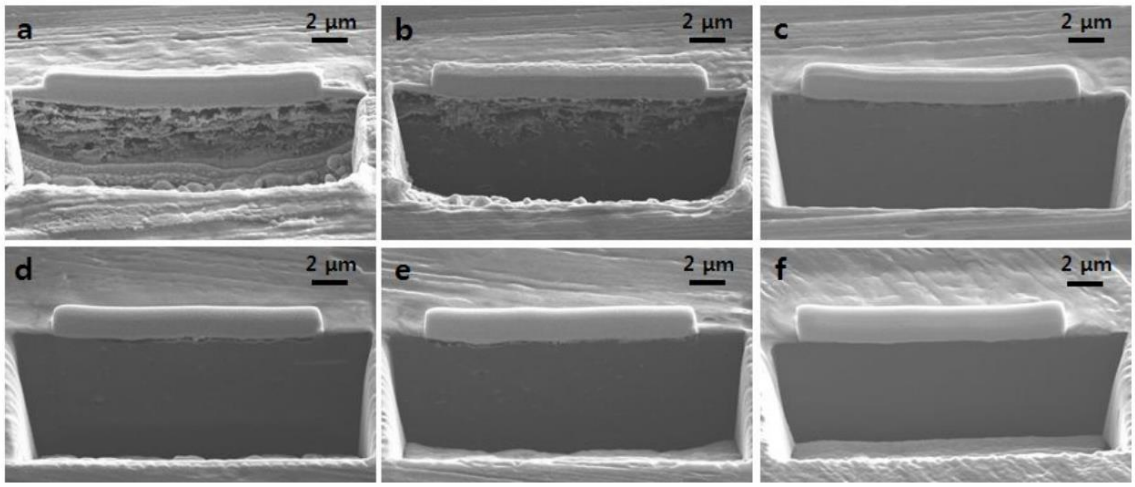

Figure 2.7. SEM images of Li metal foil after FIB milling at (a) room temperature, (b) 0 °C, (c) -50 °C, (d) -100 °C, (e) -150 °C, and (f) -170 °C. Adapted with permission from reference[147]. Copyright 2019 American Chemical Society.

A Thermo Fisher Helios 5CX was used for the FIB-SEM experiments in this thesis. Gallium ions were used as the ion beam for milling. For large cuts, a beam current of 45 nA and accelerating voltage of 30 kV were used. Final cleaning cuts of the cross-sections used lower currents at the same accelerating voltage. This instrument was equipped with a

Quorum cryogenic stage, which enabled samples to be cooled down to -185 °C. Samples were typically cooled to -145 °C before conducting cryo-FIB milling. This temperature was chosen because going below -145 °C caused delamination of the carbon tape holding the sample onto the stage. The same ion beam conditions were used during room temperature FIB. SEM images were taken at 5 kV and 0.34 nA using an Everhart-Thornley secondary electron detector.

CHAPTER 3. INTERPHASE MORPHOLOGY IN AN OXIDE ELECTROLYTE DRIVES CELL FAILURE

3.1 Introduction

The first major hurdle for the development of SSBs was to synthesize solid materials with high ionic conductivity and low electronic conductivity. After years of research, a wide variety of SSEs have been discovered. However, a key criterion for any practical SSE material is that it must be electrochemically stable against the electrodes during operation. If an SSE is unstable at one (or both) interfaces, then it will decompose over time. Side reactions typically reduce the remaining capacity of lithium ions in the battery by permanently forming new phases that sequester the lithium. Capacity fade due to electrochemical degradation of the SSE reduces a cell's energy density over time, and in some cases can proceed indefinitely if interfacial stability is poor.

Despite the existing understanding of the chemical reaction between LAGP and Li that occurs when resting[91,116], there had not been a detailed investigation of how degradation at Li/LAGP interfaces is impacted by electrochemical cycling. In this study, published in *ACS Energy Letters* in 2019, the rate dependence of the reactions between LAGP and a lithium metal anode were monitored during electrochemical cycling. This work found that LAGP was unsuitable as an SSE when interfaced with a lithium metal anode due to the severe and continuous electrochemical reaction that decomposed LAGP. This reaction was found to cause LAGP to fracture, which greatly increased the impedance

of the cell and prevented continued operation. The decomposition of LAGP was observed to be more severe when operating at higher rates, which was found to be due to the altered morphology of the reacted phases.

3.2 Chemical Reaction Between Lithium Metal and LAGP

To better understand the chemical reaction between LAGP and Li, symmetric Li/LAGP/Li cells were assembled and EIS was used to track the impedance over time (Fig. 3.1a). After an initial increase in impedance, the value remained relatively stability for ~200 hours. However, the impedance then began to rapidly grow over the next few hundred hours. Inspection of the cell afterwards revealed that the LAGP material had fractured into many small pieces. This mechanical destruction was believed to be the cause of the impedance growth. An SEM image of the Li/LAGP interface after chemically reacting for ~170 hours showed that a thick interphase layer with fairly uniform thickness was formed (Fig. 3.1b). X-ray diffraction (XRD) patterns of an unreacted LAGP sample showed the expected diffraction peaks for the material, but the diffraction pattern showed a loss of crystalline structure after inducing the chemical reaction, indicating that the interphase formed was amorphous (Fig. 3.1c).

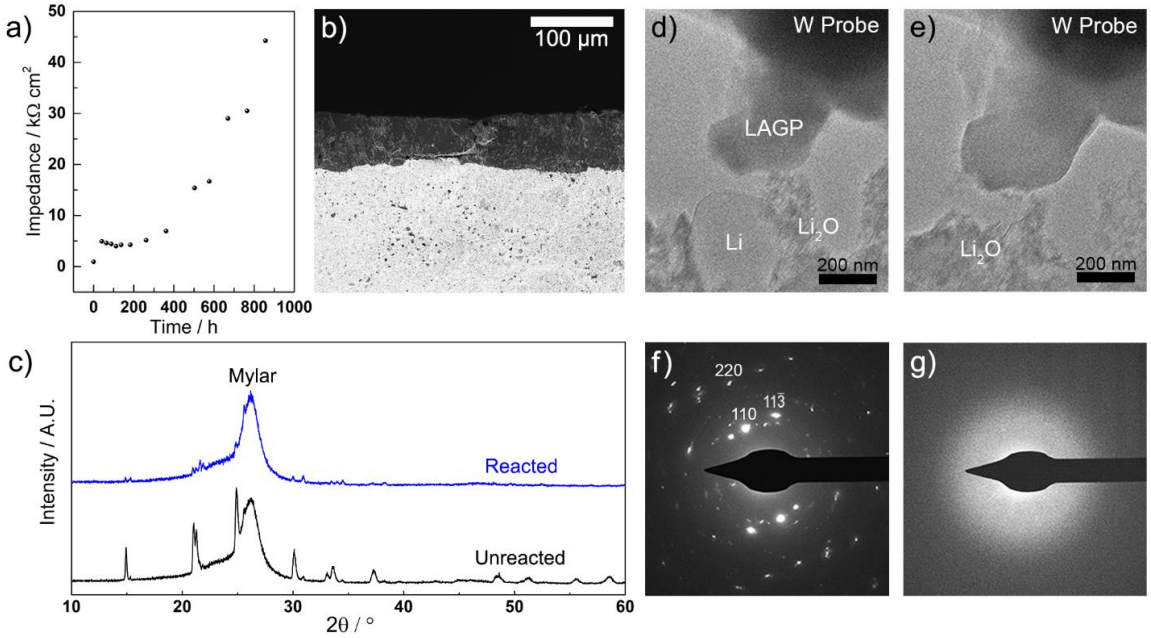

Figure 3.1. a) Plot of impedance versus time for a Li/LAGP/Li symmetric cell held at open circuit. **b)** Cross-sectional SEM image of the interphase formed by chemical reaction. **c)** *Ex-situ* glancing angle XRD of unreacted LAGP (black) and LAGP that was chemically reacted for ~170 h (blue). The broad peak at ~26.5° was from the Mylar film covering the samples to prevent air exposure. **d-g)** *In-situ* TEM of the reaction of an LAGP particle with lithium. **d)** Image of an unreacted LAGP particle before contact with lithium. **e)** Image of the same LAGP particle after being contacted and reacting with lithium. After lithiation, the particle expanded in volume and the lithium crystal disappeared. **f)** SAED pattern of an unreacted LAGP particle. **g)** SAED pattern of the same particle after lithiation.

The reaction between lithium metal and LAGP was further elucidated by using a specialized *in situ* biasing TEM holder (Fig. 2.6), capable of manipulating a probe on the order of nanometers while simultaneously applying a voltage. During the experiment, a single LAGP particle with a size of ~400 nm was contacted by a Li crystal attached to the holder probe (Fig. 3.1d). After contact, a voltage of 5 V was applied to drive lithium into the LAGP particle and cause a reaction. During this process, the LAGP particle was observed to expand by ~38% (Fig. 3.1e). Selected area electron diffraction (SAED) patterns taken before and after the reaction showed that the initially crystalline particle was converted to an amorphous structure after lithiation (Figs. 3.1f, g), in agreement with the

separate XRD measurements of a bulk LAGP pellet. The expansion of LAGP during lithiation provided insight into why fracture occurs after a long period of chemically reacting with lithium metal. Since LAGP is a rigid and brittle oxide ceramic, expansion during the formation of the interphase within the LAGP structure introduces stresses that must be eventually relieved by initiating cracks.

3.3 Effects of Cycling on LAGP Decomposition

With an improved understanding of how LAGP and Li react chemically under open circuit conditions, the effects of electrochemical cycling were explored next. Symmetric Li/LAGP/Li cells were assembled and cycled at three different current densities: 0.1, 0.2 and 0.5 mA cm^{-2}. Figure 3.2 shows the voltage profiles for cells ran at each current density using a cycle time of 2 hours for all three cells. Each cell eventually failed due to a large increase in cell impedance, similar to what was observed in the chemical reaction. However, the time to failure for these cycled cells was much faster than the chemical reaction. In the case of the chemical reaction, a high impedance was observed after ~600 hours of reacting. This time was contrasted with the cell cycled at 0.5 mA cm^{-2}, which failed in only 10 hours. Cycling at a low current density of 0.1 mA cm^{-2} still resulted in much faster failure than the chemical reaction. Comparing the results between different current densities also showed that the relationship between cell lifetime and the magnitude of the current density was not linear, as the cell at 0.5 mA cm^{-2} failed 15x faster than the cell at 0.1 mA cm^{-2}, despite only being a 5x higher current density.

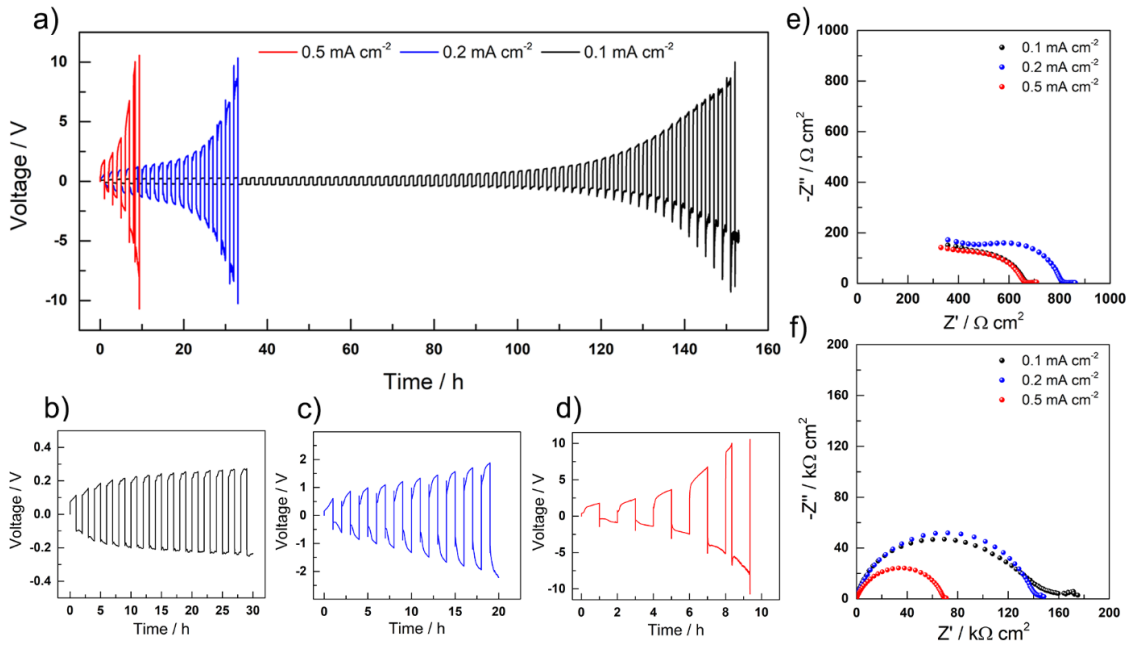

Figure 3.2. a) Galvanostatic cycling of symmetric Li/LAGP/Li cells cycled to failure (defined to be ±10 V) at 0.1 mA cm^{-2} (black), 0.2 mA cm^{-2} (blue), and 0.5 mA cm^{-2} (red). **b-d)** Magnified plots of the galvanostatic traces presented in (a) at early cycling times. **e)** Impedance spectra of each cell in (a) prior to cycling. **f)** Impedance spectra of each cell after galvanostatic cycling to failure.

After cycling until failure under these three different current densities, the cells were opened and the fractured LAGP pellets were extracted for SEM imaging. Figure 3.3 shows cross-sectional images for these three samples, which had distinct interphase morphologies compared to the interphase formed during the chemical reaction. In particular, the interphase grew non-uniformly and penetrated into the interior of LAGP, instead of forming a uniform layer only at the interface. The non-uniformity of interphase formation was also observed to increase with current density, as the sample cycled at 0.5 mA cm^{-2} exhibited significant interphase penetration throughout the cross-section.

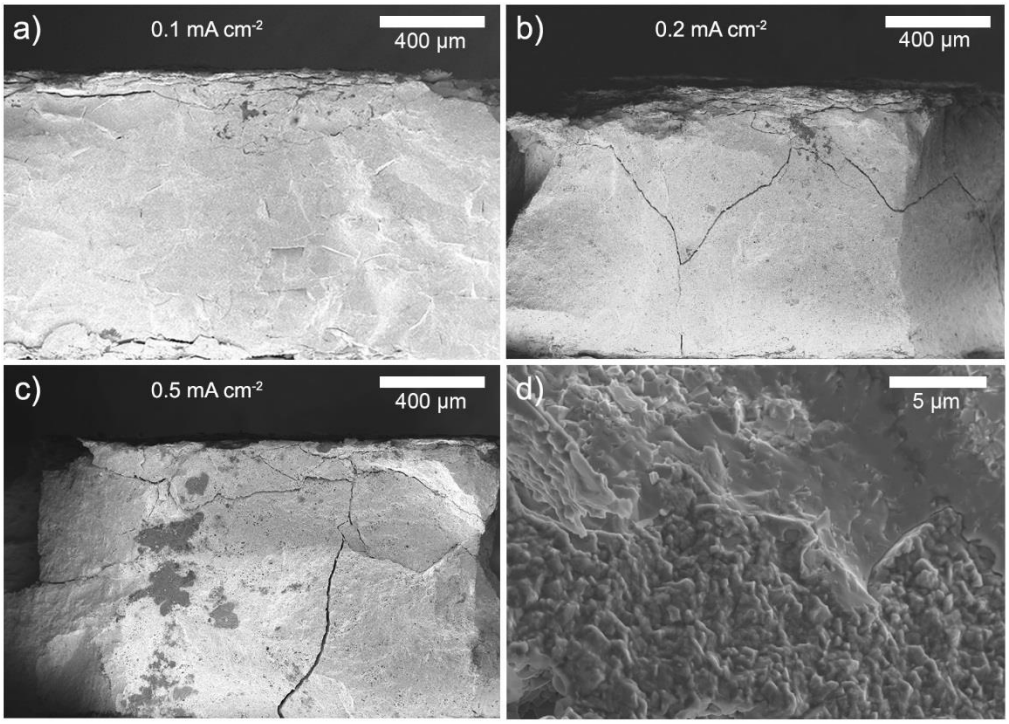

Figure 3.3. a-c) Low-magnification cross-sectional SEM images of LAGP cycled until failure at **a)** 0.1 mA cm^{-2}, **b)** 0.2 mA cm^{-2}, and **c)** 0.5 mA cm^{-2}. The darker regions are the reacted interphase that has grown into the bulk of the LAGP. **d)** Higher-magnification SEM image of the interphase grown deep within LAGP.

It was unclear whether the differences in cell lifetime and the extent of interphase growth were caused by the current density or by the different amounts of lithium transferred in each experiment. To decouple these two parameters, symmetric Li/LAGP/Li cells were cycled using the same capacity per half-cycle (0.25 mAh cm^{-2}) and a total capacity of 2.5 mAh cm^{-2} over the course of the experiment. Figure 3.4 shows the galvanostatic traces for cells cycled at each current density (0.1, 0.2, and 0.5 mA cm^{-2}), as well as SEM images showing the reaction throughout the cross section of each sample. The SEM image from the cell cycled at 0.1 mA cm^{-2} showed that the interphase is primarily maintained near the top surface (Fig. 3.4d), with some small regions of the reacted phase penetrating into the near-surface bulk region. In contrast, the cells cycled at currents of 0.2

and 0.5 mA cm^{-2} rapidly reached high overpotentials and exhibited poor electrochemical stability. Despite the similar galvanostatic signatures, the cell cycled at 0.5 mA cm^{-2} exhibited substantially more growth of the reacted phase into the bulk of the LAGP pellet compared to the cell cycled at 0.2 mA cm^{-2}. Having isolated the effects of current density from the total lithium transferred during cycling, these data demonstrated that interphase morphology is highly dependent on the magnitude of the applied current density. Given that the interphase is expanded and exerts stress on the surrounding material, the highly non-uniform morphology generated larger stresses and accelerated fracture, causing the cell at 0.5 mA cm^{-2} to fail much faster.

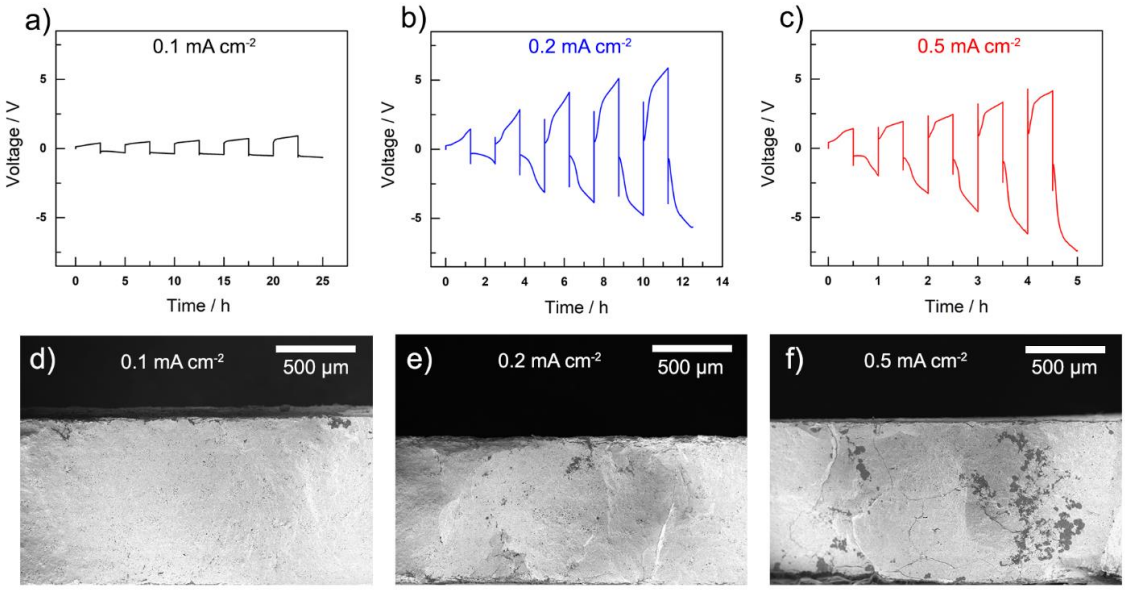

Figure 3.4. Galvanostatic cycling of symmetric Li/LAGP/Li cells cycled at **a)** 0.1 mA cm^{-2}, **b)** 0.2 mA cm^{-2}, and **c)** 0.5 mA cm^{-2}. For all three current densities, the capacity per half-cycle was 0.25 mAh cm^{-2} and the total capacity was 2.5 mAh cm^{-2}. **d-f)** Cross-sectional SEM images of LAGP after cycling with the same amount of Li^+ passed. The top surfaces of the pellets were visible in (d) and (f) due to sample orientation in the microscope.

The transport properties of the interphase should play a key role in the interphase reaction process. If the interphase is electronically insulating but ionically conductive, then a self-limiting interphase layer is expected to form because of direct chemical reaction. Instead, continuous growth of the chemically formed interphase and non-uniform penetration was observed during electrochemical cycling, which suggested that the interphase was a mixed ion and electron conductor. Previous XPS experiments on the chemical reaction between lithium and LAGP demonstrated that Ge^{4+} is reduced to Ge^{0} in the interphase, which could give rise to increased electronic conductivity. However, the chemical nature of the electrochemically formed interphase had not yet been investigated. To compare the chemical nature of the chemical and electrochemical interphase, XPS experiments were conducted on (i) a chemically reacted sample that was contacted with lithium foil for ∼25 h and (ii) an electrochemically reacted sample cycled at 0.2 mA cm^{-2} for ∼25 h in a symmetric cell. Ar sputtering was used for depth profiling. Figure 3.5 shows the Ge 3d spectra at the surface and deeper within the interphase for the two different interphases. In both cases, the Ge in the interphase was reduced compared to the Ge^{4+} in pristine LAGP. However, these data also showed that the distribution of oxidation states in the two different interphases was different, with an increased fraction of species reduced beyond Ge^{2+} in the electrochemical interphase. This difference could be explained by the fact that the electrochemical interphase is formed both by chemical diffusion (as in the chemical interphase) as well as additional reactions due electrochemical reduction. In both cases, however, mixed-conduction behavior was observed.

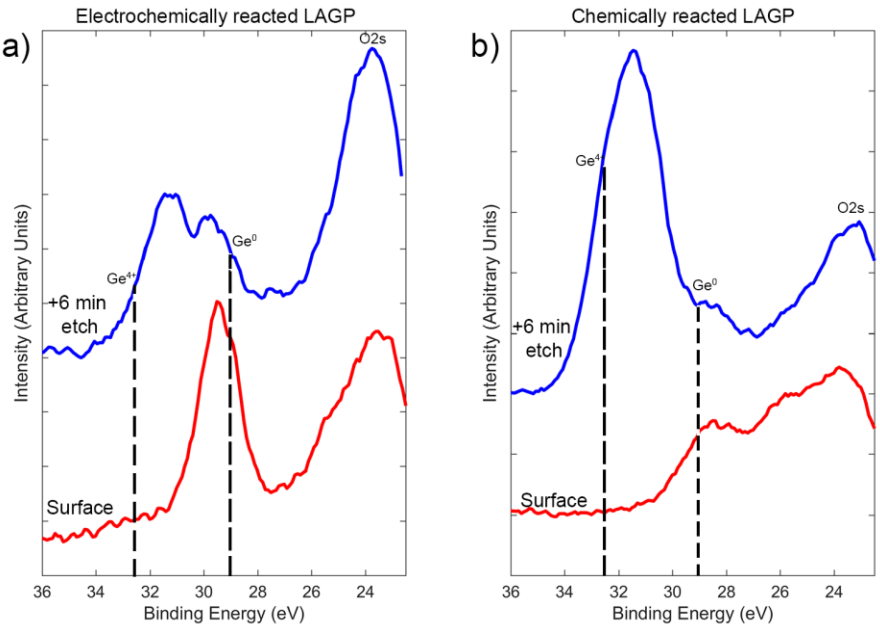

Figure 3.5. XPS spectra of **a)** the electrochemically-reacted interphase (0.2 mA cm-2 for ~25 h) and **b)** the chemically-reacted interphase (held at open circuit for ~25 h). In both experiments, spectra were taken at the surface (red) and after sputtering into the interphase using an Ar^+ ion beam (blue). The dotted lines illustrate standard binding energies for Ge^{4+} and metallic Ge. After sputtering, a series of Ge intermediate oxidation states (Ge^{4+}-Ge^0) were seen for both the reacted interphases. Relatively reduced Ge was observed for the surfaces. All spectra were smoothened using a Savitzky-Golay filter with a degree of 1.

The ability to conduct both ions and electrons through the interphase would enable two electrochemical reduction pathways during cycling, as schematically shown in Fig. 3.6. LAGP could be electrochemically reduced at the LAGP/interphase boundary (reaction pathway 1) by combining incoming Li^+ ions with electrons that have traversed the interphase. This reaction may occur via the direct electrochemical reduction of LAGP, or it could be a multistep process involving electrochemical reduction of ions to form lithium metal followed by chemical reaction with LAGP. Lithium plating at the Li/LAGP interface could also occur (reaction pathway 2). These two distinct reduction pathways are in competition with each other in this system, and it is likely that both processes occur simultaneously (depending on the current density).

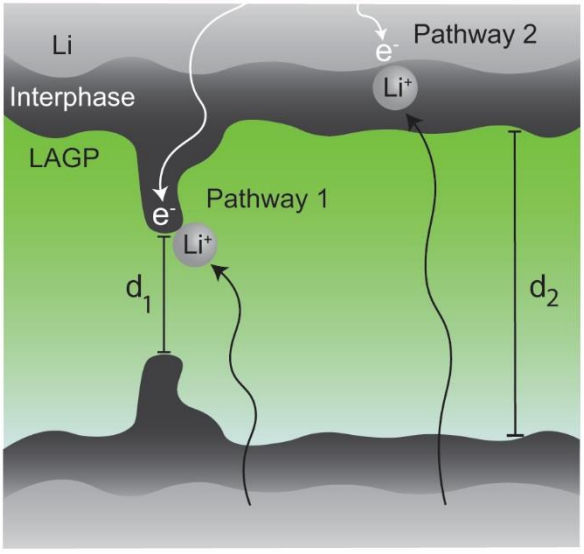

Figure 3.6. Schematic showing non-uniform interphase growth and possible reduction pathways in relation to the growth of the mixed-conducting interphase. Pathway 1 is the reduction of LAGP at the LAGP/interphase boundary via the transport of electrons through the mixed-conducting interphase. This pathway plays an important role in non-uniform growth of the interphase. Pathway 2 is the plating of lithium at the interphase/Li interface, which should not cause electrochemical growth of the interphase. Non-uniform growth is promoted via pathway 1 since non-uniform growth decreases the distance required for Li^+ transport (e.g., d_1 compared to d_2), thereby locally lowering the resistance to ion conduction.

We hypothesize that the shift from uniform interphase growth seen in the chemical reaction to non-uniform growth observed after electrochemical cycling at higher currents was a consequence of the mixed-conducting properties of the interphase that activate reaction pathway 1. In general, the resistance to ion transport across the SSE (and thus the portion of the overpotential due to ion transport) is lower when the ion transport length is shorter. The non-uniform growth of the interphase at higher currents likely arises because of the system acting to minimize the transport distance and the required overpotential for the electrochemical process. The reduction of LAGP at interphase protrusions (pathway 1) allows for the continuous decrease of ion transport length. This promotion of shorter ion transport pathways is expected to be amplified at higher current densities because the

overall overpotential is higher, leading to the significant nonuniformities observed. In addition to this effect, reaction pathway 1 would also be promoted if the interphase electronic conductivity was higher than the interphase ionic conductivity; this phenomenon (which would also be exacerbated at higher currents) could also be playing a role.

As previously mentioned, the transport properties of the interphase strongly influence interphase growth behavior and degradation mechanisms in SSEs. Discovering or creating interphases on various SSEs with appropriate ionic and electronic conductivities to prevent the reduction of the SSE by lithium is critical for designing SSBs that can be reliably cycled over long periods of time. For example, engineering the surface of LAGP to create artificial interphases that are stable over time could prevent the buildup of stresses that lead to mechanical failure. This strategy has recently been pursued with the primary goal of reducing interface resistance at Li/LLZO interfaces, but going further to engineer interfaces in inherently unstable SSE materials is a promising route to increasing the number of electrolytes available for solid-state battery development. Furthermore, preventing the continuous formation of the interphase will also require consideration of the direct diffusion of Li species from lithium metal to react with the SSE, as occurs during the chemical reaction reported here. This pathway is often overlooked in the context of mixed-conducting interphase formation, but it also must be controlled for long-term stability.

3.4 Conclusions

This study revealed reaction mechanisms at the Li/LAGP interface and linked current-dependent reaction processes to chemo-mechanical failure of SSBs. The chemical

and electrochemical reactions at the Li/LAGP interface were investigated using *in situ* TEM and other *ex situ* techniques. The reaction of LAGP with lithium involved (electro)chemical reduction of the SSE to form an amorphous interphase. During this process, LAGP underwent volume expansion due to the incorporation of lithium that caused the evolution of mechanical stress within bulk LAGP pellets and eventually induced fracture. Electrochemical cycling of symmetric Li/LAGP/Li cells showed that the impedance and overpotential increased with time until fracture-induced failure. Non-uniform growth of the reacted interphase occurred within the bulk of the SSE at higher currents, which can cause localized stress concentrations and accelerate mechanical failure of the LAGP. This work demonstrated that the continuous reaction of the Li/LAGP interface was the root cause of the chemo-mechanical degradation of this material during cycling, and the improved understanding of these chemical and electrochemical interfacial reactions will hopefully spur development of strategies to combat degradation processes in a variety of SSE materials.

CHAPTER 4. OBSERVING INTERFACIAL DYNAMICS IN SOLID-STATE BATTERIES DURING CYCLING USING OPERANDO X-RAY TOMOGRAPHY

4.1 Introduction

Lithium metal anodes in SSBs are currently limited by how Li/SSE interfaces evolve during cycling due to phenomena such as lithium metal penetration, contact loss, and electrolyte decomposition. These phenomena are dynamic and do not necessarily occur continuously or behave linearly. Understanding these phenomena requires *operando* experiments for directly elucidating how solid-solid interfaces evolve in real time. However, probing buried interfaces in SSBs necessitates techniques that can penetrate materials while providing local interfacial information.

X-ray tomography is an excellent tool for studying buried interfaces as it yields three-dimensional reconstructions of materials with spatial resolution down to the sub-micron scale[135,138]. X-ray tomography has recently revealed how SSB cell performance is impacted by factors such as structure, porosity and the mechanical properties of materials[44,47,50,51,86,110,150–160]. Operando and multi-modal experiments have captured the evolution of cathodes and alloying anodes (such as tin and indium) during cycling[152–154], and such experiments have been able to image lithium metal within SSBs despite its weak X-ray attenuation[155,156]. However, only a relatively small number of X-ray imaging studies has investigated the interfaces between lithium metal electrodes and SSEs[46,47,86,110,156–158]. Furthermore, there have been no operando X-ray tomography experiments that have

imaged void formation and Li/SSE interfacial contact during cycling to enable quantitative linkage to electrochemical behavior, which is critical for improving our understanding of SSB operation.

This chapter discusses work that was published in *Nature Materials* in 2021. *Operando* X-ray computed microtomography experiments were conducted at the Advanced Photon Source, a state-of-the-art synchrotron facility, to probe Li/SSE interfaces during cell operation. The advantages of synchrotron radiation were leveraged to detect interfacial features, such as interfacial voids and interphase, across entire interfaces in SSBs. Segmentation routines were developed to quantify the presence of different phases in the reconstructed tomographic images, which provided a direct link between the evolution of these phases and the electrochemical performance. The results from this work demonstrate the importance of interfacial contact and its rearrangement throughout cycling on cell stability, which had never been imaged directly before.

4.2 *Operando* X-Ray Tomography During SSB Cycling

The SSE material studied in this work was the sulfide $Li_{10}SnP_2S_{12}$, which was measured to have a room temperature ionic conductivity of 2.1 mS cm^{-1}. Similar to LAGP discussed in Chapter 3, LSPS is susceptible to electrochemical degradation against lithium metal due to the presence of tin that is easily reduced by lithium metal to form Li-Sn alloys in the interphase[128,161]. Given the MIEC properties of the interphase, LSPS does not form a self-passivating interphase and instead continues to react over time. However, the advantage of using LSPS in this study was that it allowed for operating under high current densities due to its high ionic conductivity.

SSBs were assembled using the custom cell housing for X-ray tomography described in Chapter 2. The beamline was set-up to use monochromatic X-rays with an energy of 28 keV to avoid the predicted absorption edge of LSPS at 29.2 keV (Fig. 4.1). The combination of the lens and detector yielded a field of view of ~4.2 x 1.4 mm^2 with a voxel size of 1.7 µm. The time to complete an entire scan was 7 minutes. Scans were taken during the electrochemical experiment without pausing the applied current.

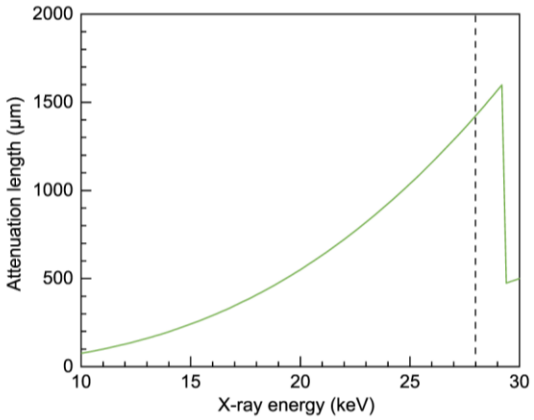

Figure 4.1. Attenuation length calculated for $Li_{10}SnP_2S_{12}$. Smaller attenuation lengths indicated greater X-ray absorption by the material. The dashed line represents the X-ray energy used for all operando experiments (28 keV).

Figure 4.2a shows the voltage profile for a symmetric Li/LSPS/Li cell cycled once at 1 mA cm^{-2}. A total of 40 X-ray tomography scans were completed over the course of this experiment. A reconstructed image of the cell cross-section at the start of the experiment is shown in Fig. 4.2b. The dark contrast at the top and bottom of the image represented the two lithium metal electrodes, while the grey contrast in the middle was the LSPS layer. Given the orientation of the electrodes, they were referred to as the top and bottom electrodes to differentiate between the two. During the first half cycle of this

experiment (t = 0 hr to t = 5.25 hr), lithium was stripped from the top electrode and plated at the bottom electrode. The voltage increased slightly during this time, until the current direction was manually switched and stripping started at the bottom electrode. During this second half cycle, the voltage began to rapidly polarize after a few hours, corresponding to cell failure. It is important to note that the subtle oscillation seen in the voltage profile was likely because the electrochemistry was not paused during each tomography scan. The interactions between the X-rays and battery materials likely shifted the voltage by ~10 mV, but these interaction were not expected to fundamentally alter the battery degradation that was observed.

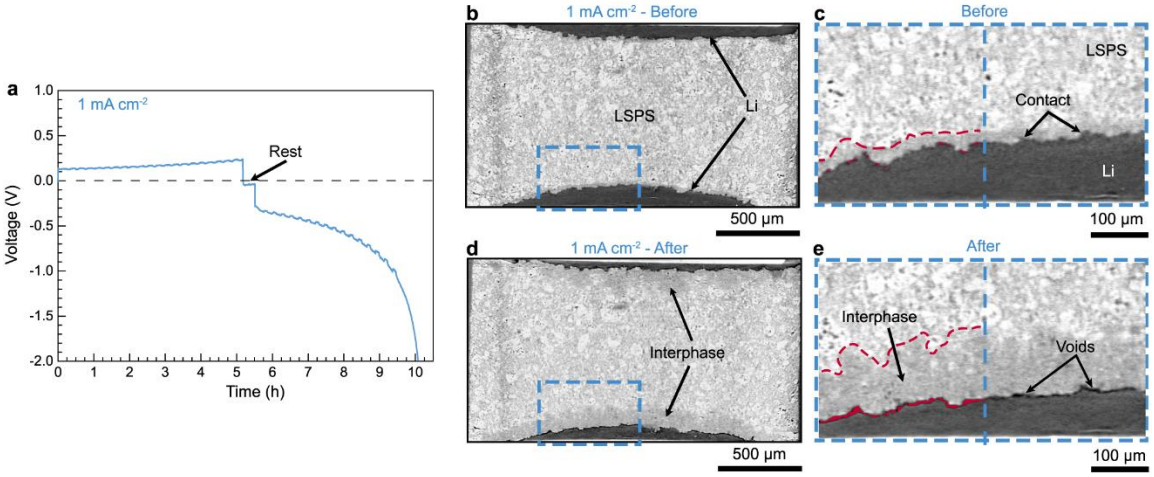

Figure 4.2. a) Galvanostatic voltage curves measured during operando experiments at 1 mA cm^{-2}. **b, c)** Reconstructed cross-sectional image before cycling at 1 mA cm^{-2}. The regions with dark contrast were the lithium electrodes, whereas the grey phase was the LSPS electrolyte. The steel current collectors were also visible with white contrast at the top and bottom of the image. **c**) Magnified cross-section of the Li/LSPS interface before cycling at 1 mA cm^{-2}, taken from the blue-boxed region in (**c**). In the left half of the image, voids were overlaid with red for easier visualization, and the red dashed line above demarcated the interphase boundary; the right half of the image was unmarked. **d**) Cross-sectional image from the same location shown in **(b)** after the electrochemical protocol. **e)** Magnified cross-section of the same interface as shown in **(d)** after one full cycle at 1 mA cm^{-2}.

After the cell was cycled once, distinct differences at the interface could be detected in the reconstructed cross-sectional images, as shown in Fig. 4.2d,e. A key observation was the significant formation of voids at the interface between the bottom lithium electrode and LSPS. These voids manifested as pixels darker than lithium, as they represented the absence of material. Additionally, the formation of interphase could be seen based on the darker grey contrast formed above the lithium electrode. Both the interphase and voids are expected to play a role in how cell failure occurs. With over 40 tomographic scans that each represented the 3D volume of the entire solid-state battery at different stages of the experiment, it was possible to analyze these data and develop quantitative relationships between different phases and the electrochemistry.

It is also noted that the electrolyte exhibited varying contrast between particles, with some being brighter than others. One reason for this variation could be the presence of particles with a different phase than the desired $Li_{10}SnP_2S_{12}$. This could be related to impurities in the synthesis, or particle reactions that occurred during processing. Another factor could be variation in density of the individual particles due to differences in the compaction forces. Regardless of the contrast variation in the electrolyte, this material still enabled operating the SSB at high current densities.

4.3 Interphase Growth and the Absence of Lithium Plating

Reconstructed images revealed that a large amount of interphase was formed continuously at the cathodic interface (where reduction occurs). This process was visualized over time using the segmentation routines, as discussed in Chapter 2. The presence of persistent interphase growth indicated that a fraction of the total current was

being used to decompose LSPS. In an ideal battery, 100% of the current should be utilized for lithium plating. By tracking the change in volume of the two lithium electrodes and interphase, the fraction of current that went towards plating could be quantified. Figure 4.3a shows a plot of these volume changes over the course of the first half cycle. Plating should have been occurring at the bottom lithium electrode during this time, and thus the volume of that electrode should have increased. However, the data analysis showed that the volume actually decreased, indicating that no plating was occurring. Furthermore, the interphase volume was observed to increase linearly during this time.

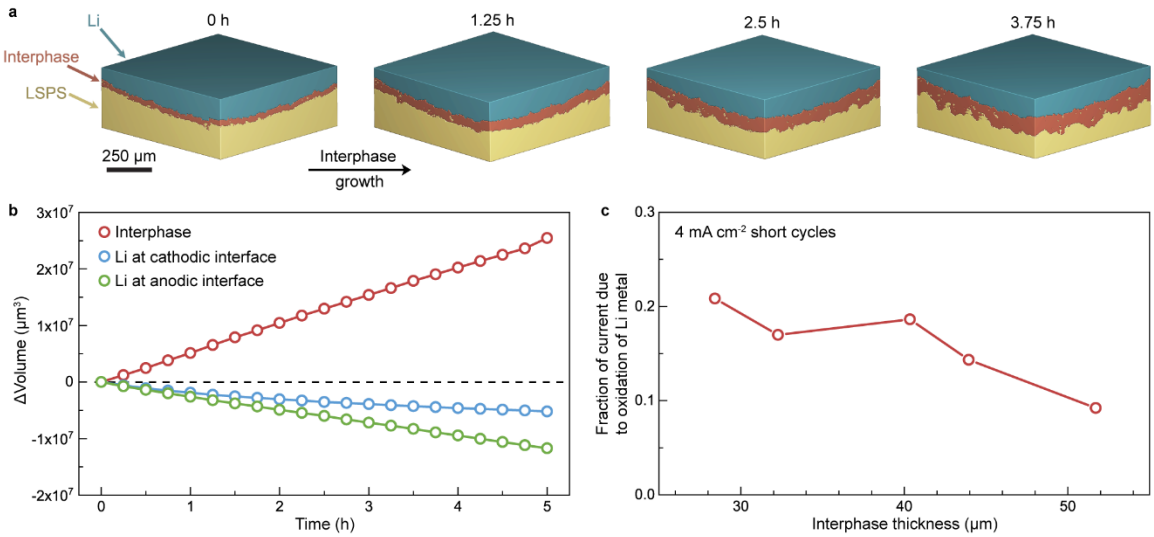

Figure 4.3. a) Three-dimensional renderings of a 680 × 680 × 340 µm subvolume at the Li/LSPS interface over time during reduction at 1 mA cm^{-2}. Segmentation routines were used to visualize the lithium metal (blue), interphase (red) and LSPS (yellow). **b**) Plot showing the change in volume of the interphase at this interface, as well as both lithium electrodes, during the first half-cycle. The interphase and cathodic lithium volumes were taken from the subvolume shown in **(a)** whereas the anodic lithium volume was taken from a subvolume with the same size at the opposite interface (not shown). **c**) Fraction of total current due to oxidation of lithium metal, plotted as a function of the interphase thickness. These data were taken from a separate operando experiment with 30 min cycles at a current density of 4 mA cm^{-2}; these conditions were used to steadily grow the interphase thickness.

These results demonstrate that little to none of the current was used to plate lithium, instead being used to form interphase. This result is important in the context of the SSB community. While the reactivity of Li/LSPS interfaces was known, this study was the first to confirm the absence of measurable lithium plating during cell operation. The lack of lithium plating is a critical blow to the viability of LSPS as an SSE material, as a practical device has a limited reservoir of lithium that would be rapidly depleted if LSPS was the electrolyte material. This behavior emphasizes the importance of carefully selecting SSE materials with appropriate electrochemical stability against the electrodes being used.

Data analysis of the volume changes for multiple experiments yielded additional understanding of charge transfer at reactive Li/SSE interfaces. During stripping, lithium ions should have been oxidized from the lithium metal electrode and used in reduction reactions at the opposite plating electrode. Unexpectedly, tracking the volume change of the stripping lithium electrode showed that not enough current was supplied to match the total current in the cell. Therefore, additional oxidation current likely was supplied by the oxidation of lithium ions in the interphase, indicating that the interphase was a partially reversible electrode.

4.4 Interfacial Void Formation and Contact Loss

The observed formation of voids at the Li/LSPS interfaces was expected to play an important role in cell stability. A segmentation routine was used to distinguish interfacial voids from other phases, such as lithium metal, LSPS and internal porosity. This analysis allowed us to identify voids across the entire Li/LSPS interface and quantitatively link their evolution to electrochemistry. Figure 4.4a displays a segmented 3D subvolume at the

Li/LSPS interface during stripping that shows the interphase and voids that form between LSPS and the lithium electrode. These renderings were taken from the second half-cycle of the cell tested at 1 mA cm^{-2} (Fig. 4.2a) From these renderings, it is clear that the volume of the voids grows substantially after 3.0 mAh cm^{-2} have been stripped.

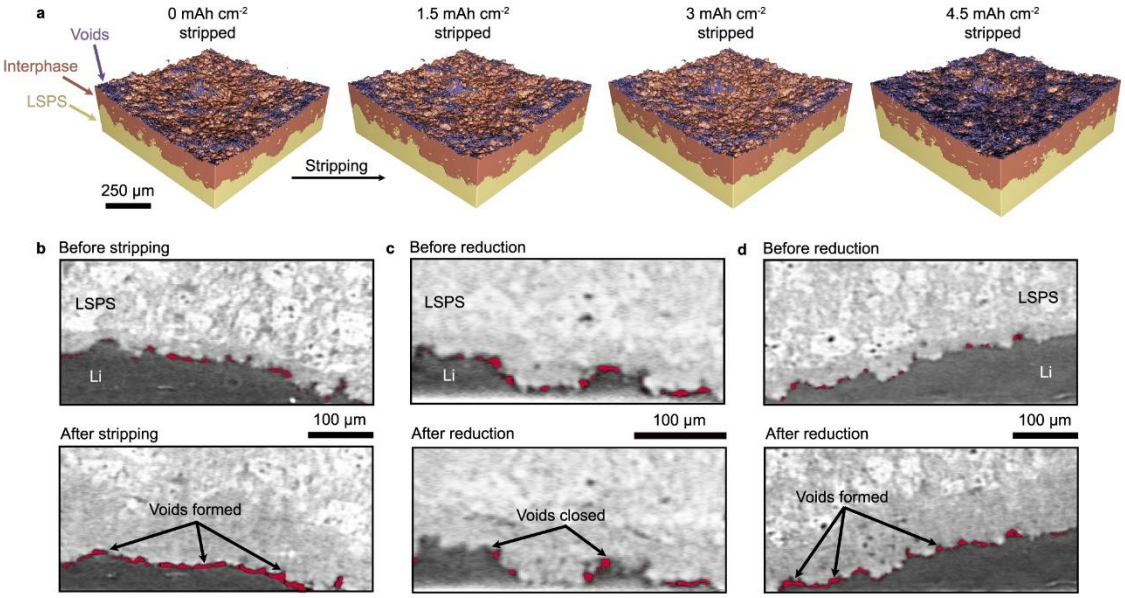

Figure 4.4. a) Three-dimensional segmented renderings of the Li/LSPS interface at different times during stripping at 1 mA cm^{-2}. The renderings show the voids (purple), the interphase (red) and LSPS (yellow). **b)** Two-dimensional cross-sectional images of the Li/LSPS interface before (top) and after (bottom) stripping at 1 mA cm^{-2}. Pixels identified as voids during the segmentation process were overlaid with red, showing that void growth occured during stripping. **c)** Cross-sectional images of the Li/LSPS interface before (top) and after (bottom) reduction at 4 mA cm^{-2} showed that voids could be closed during reduction. **d)** Cross-sectional images before (top) and after (bottom) reduction at 1 mA cm^{-2} showed that voids could also be formed during reduction.

Three different types of interfacial void evolution were observed. Each subfigure in Fig. 4.4b-d shows the two-dimensional reconstructed image of the same location at the Li/SSE interface before and after an electrochemical process, with the segmented interfacial voids colored red for visibility. The most common process was the formation of voids during stripping (Fig. 4.4b). Voids formed during stripping when Li^+ ions were

removed faster than the lithium metal could be replenished, either through self-diffusion or mechanical deformation. Void formation during stripping was consistent with recent studies that have demonstrated polarization at the stripping electrode.

The second phenomenon observed was the closing of voids during reduction (Fig. 4.4c). Despite there being no measurable lithium deposition to fill the voids, it is suspected that local compression due to interphase growth could close them, but this process was not observed in every experiment. The third phenomenon observed was the formation of voids at the cathodic interface (Fig. 4.4d). This behaviour was counterintuitive, as mass was being added at this interface. However, the lithium electrode was being consumed due to a chemical side reaction, which probably resulted in such void formation.

The image contrast between voids and lithium enabled the real-time determination of how contact area influences the electrochemistry. Figure 4.5a shows how the total Li/LSPS contact areas across the entire top and bottom interfaces changed over time for the cell cycled at 1 mA cm^{-2}. Stripping occurred at the top interface for the first ~5.5 h, after which stripping began at the bottom interface. The electrochemical signature in the first half-cycle showed only a minor increase in overpotential, which was reflected in the relatively invariant contact areas at both interfaces. After cycling for ~9 h, the cell began to rapidly polarize to −4 V, during which the interfacial contact area at the bottom interface decreased by 52%. It is important to note that this two-electrode experiment included voltage contributions from impedance at both interfaces.

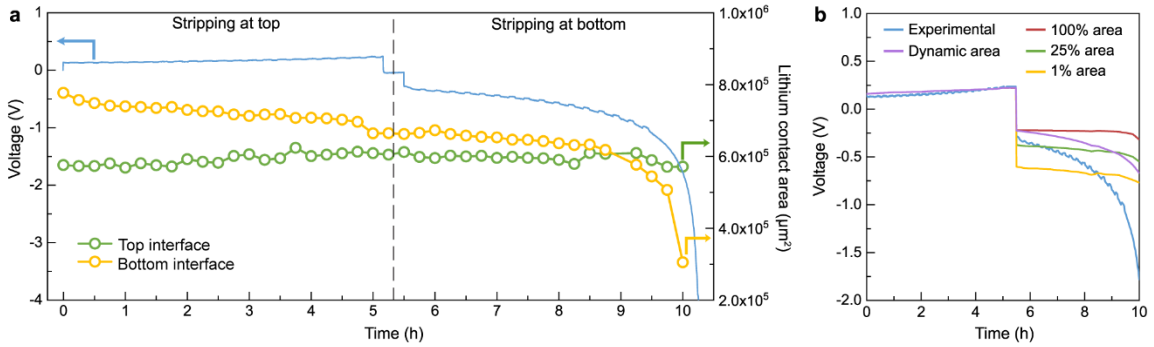

Figure 4.5. a) Plot of the voltage curve measured during cycling at 1 mA cm^{-2} (blue line) and the corresponding total lithium contact area of the top (green) and bottom (yellow) Li/LSPS interfaces in this cell. **b**) Comparison between the experimental voltage curve (blue) and theoretically predicted voltage curves using 100% (red) of the experimental contact area in the second half-cycle, 25% (green), 1% (yellow) and the dynamically varied contact area (purple).

The observed correlation between the interfacial contact and the increase in cell voltage suggested that the loss of contact at the anodic interface drove cell failure. To investigate these effects, an electrochemical model was developed that took into account the cell geometry and incorporated Butler–Volmer kinetics at the Li/SSE interface, as well as transport in the SSE and the growing interphase. Figure 4.5b shows the results for the situation in which the voltage of the first half-cycle was matched to the experiment through choice of the unknown interphase conductivity and interfacial exchange current density. These conditions were then used to predict the voltage of the second half-cycle on the basis of the experimentally measured contact area variation of the bottom interface without taking into account the spatial contact distribution. The predicted magnitude of the cell voltage under these conditions was much lower than the measured value. Reducing the contact area in simulations of the second half-cycle increased the overpotential (Fig. 4.5b), but matching to the experiment requires the imposition of an extremely low contact area.

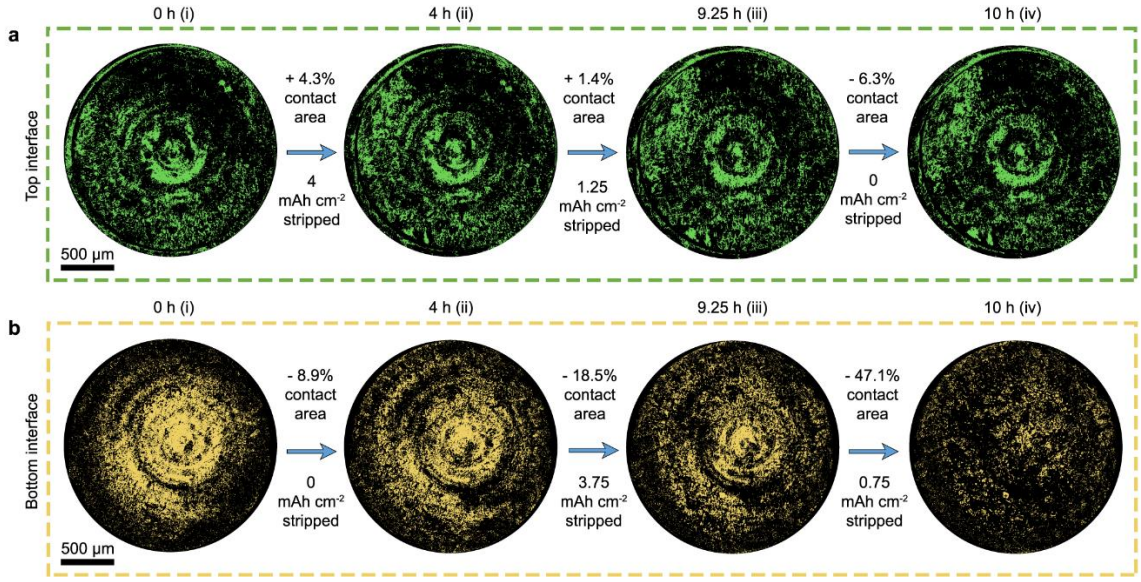

Figure 4.6. a) Contact area maps of the entire top Li/LSPS interface throughout the experiment. The percentage change in contact area and lithium capacity removed between maps are indicated. **b)** Contact area maps of the entire bottom Li/LSPS interface throughout the experiment. Colored pixels indicate the presence of interfacial contact at that location, while black pixels indicate a lack of contact (that is, a void or no lithium is present at that location).

The spatiotemporal evolution of contact at each interface was visualized by creating contact area maps from the segmented datasets (Fig. 4.6). These contact area maps showed the contact area across the entire interface throughout cycling, with coloured pixels (green for the top interface and yellow for the bottom interface) representing contact between lithium and the interphase/LSPS, and black pixels in the maps indicating no contact (that is, either an interfacial void or no lithium was present). At time = 0 h, there were already numerous regions without interfacial contact that are probably the result of insufficient stack pressure. This meant that the effective current density was actually 4–5 times higher than the nominal value. The contact area maps for the top interface (Fig. 4.6a) show that there was only minor contact loss at the top throughout the entire experiment. The contact area maps of the bottom interface (Fig. 4.6b) showed a more substantial change in contact

distribution. A contact loss of −8.9% occurred over the first 4 h during reduction. A dramatic contact loss of −47.1% at the bottom interface occurred over the last 0.75 h during stripping, which corresponded to the period of rapid cell polarization. The contact loss at the bottom interface was greater in the final hour of cycling than during the first nine hours.

The contact analysis suggested that the discrepancy between the predicted and experimental voltage curves was likely due to current constriction from spatial reconfiguration and the loss of interfacial contact. Current constriction can occur when interfacial contact locations are relatively small compared to the nominal interfacial area, which causes distortion of current lines and the creation of constriction resistance. The phenomenon of current constriction is well established in other types of solid–solid interfaces[97], but it has only recently been proposed as a key factor in lithium-based SSBs in a study that found that the constriction in bulk ion transport near the Li/LLZO interface is responsible for high interfacial impedance[45]. As shown in Fig. 4.6b, the large, continuously contacting regions present initially at the bottom interface were broken up into small isolated contacting spots by the end of the experiment. Before cycling, 71% of the total contact area at this interface was contained within two large regions with areas of 0.42 and 0.19 mm^2, whereas the remaining 29% came from separated contact regions with individual areas of less than 0.02 mm^2. After stripping, 100% of the contact area was supplied by separated contact regions with areas less than 0.02 mm^2. The increase of small, isolated contact spots would greatly enhance current constriction effects, which probably drove the substantial cell polarization.

As shown here, operando X-ray computed microtomography enabled quantification of the spatial distribution of physical contact at Li/SSE interfaces. However,

these experiments probably provided an overestimate of the contact area, since the spatial resolution was not sufficient to resolve all microscopic voids or atomic-scale vacancies. Importantly, our results allowed for the monitoring of micron-scale contact changes across the entire field of view of the interface, thus capturing how the interfacial contact changes impacted the electrochemistry. We therefore conclude that the loss of contact at the stripping interface was the underlying phenomenon that lead to cell failure in this system.

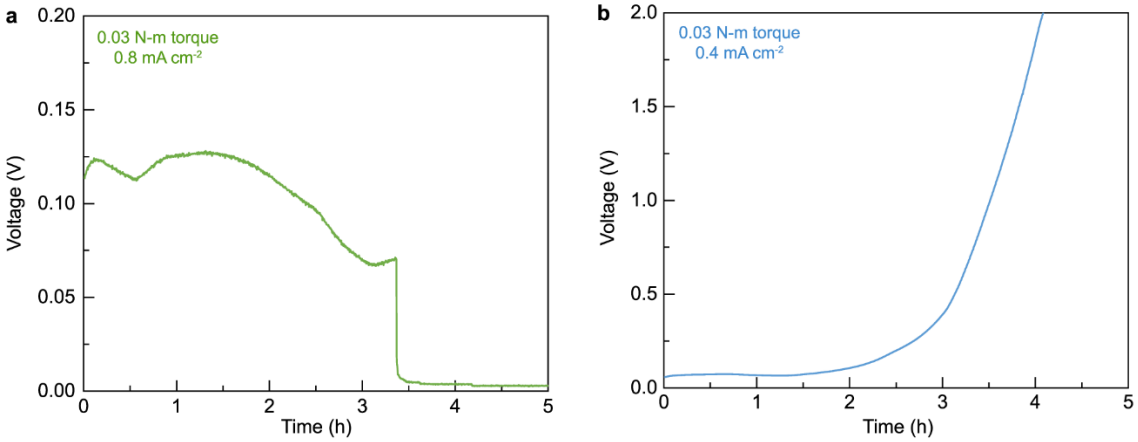

Figure 4.7. **a)** Galvanostatic stripping experiment with a Li/LPSC/Li symmetric cell assembled in the custom X-ray tomography housing. At a current density of 0.8 mA cm^{-2} and assembly torque of 0.03 N-m, the cell short circuited after ~3.5 hours of stripping. **b)** Stripping at the same stack pressure but using a lower current density of 0.4 mA cm^{-2} resulted in cell polarization after 2 h due to the accumulation of interfacial voids at the stripping interface.

The evolution of contact is expected to affect behaviour at all solid-state electrochemical interfaces. Indeed, similar polarization behaviour has been observed during lithium plating/stripping experiments with LLZO[45,46], which is the most stable SSE against lithium metal, as well as sodium/Na-β″-alumina interfaces[159], suggesting that these results are relevant to solid-state interfaces beyond lithium. To explore polarization

behaviour in different SSEs, electrochemical experiments were conducted with the argyrodite-type SSE material LPSC in symmetric cells using the X-ray tomography cell housing. Unlike LSPS, LPSC forms a kinetically stabilized interphase versus lithium, which minimizes interphase growth but also enables lithium filaments to penetrate the material. At a current density of 0.8 mA cm^{-2}, the cell short-circuited due to filament growth before any substantial polarization could occur (Fig. 4.7a). The lower current density of 0.4 mA cm^{-2} avoided filament growth but led to severe polarization beyond 2.0 V after a few hours (Fig. 4.7b), much like the Li/LSPS/Li cells shown in Fig. 4.2a and resembling other LPSC results. The electrochemical similarities between LSPS, LLZO, and LPSC indicated that the *operando* experiments in this work captured interfacial contact phenomena that are relevant to a wide range of SSE materials.

4.5 Volumetric Changes and Partial Molar Volume Mismatch

This dataset also enabled the analysis of volume changes and displacements throughout the cell. Figure 4.8a shows a portion of a lithium electrode that decreased in volume during stripping at 1 mA cm^{-2}. The Li/SSE interface moved upwards by ~17 μm (indicated by the red lines) due to the lithium electrode receding and the simultaneous expansion of the interphase at the opposite interface. Through this process, however, the current collector also moved downwards by ~20 μm (blue lines). Additional analysis showed that the LSPS pellet underwent non-uniform displacements during cycling, as shown by the vector field map with fivefold scaling in Fig. 4.8b. The maximum displacement measured in the SSE was ~20 μm, which was consistent with the upward movement of the Li/LSPS interface in the previous half-cycle (Fig. 4.8a). The LSPS material thus moved non-uniformly towards the anodic interface, with greater

displacements near the centre of the pellet compared with the edges of the pellet that probably resulted in shear strain and non-uniform stresses.

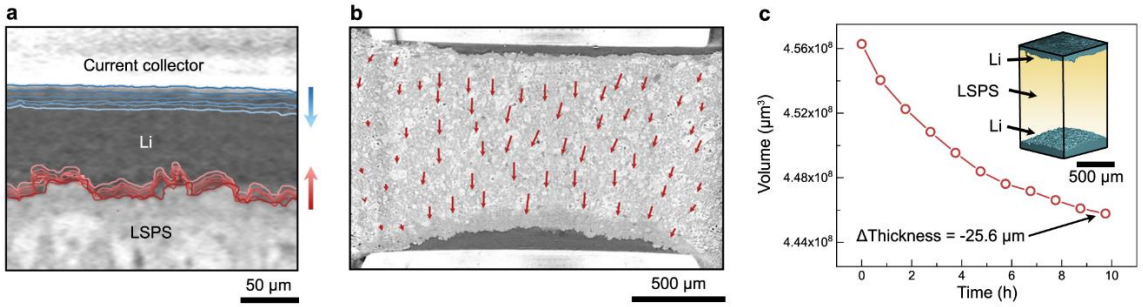

Figure 4.8. a) The position of the Li/LSPS interface and the current collector tracked during stripping of the lithium. The arrows indicate the direction of motion of each interface: darker lines represent positions at earlier times during the stripping, with the transition to lighter lines as stripping proceeds. **b**) Vector map showing physical displacements of the point at the base of each vector as lithium was stripped from the bottom interface at a current density of 1 mA cm^{-2}. The magnitude of each vector is scaled by a factor of five for visual clarity. **c**) Measured volume of a subvolume consisting of the entire Li/LSPS/Li stack during cycling at 1 mA cm^{-2}. The analyzed subvolume was 680 × 680 × 1360 µm and is visualized in the inset, with lithium metal in blue and LSPS in yellow. The total change in thickness of this cell stack at the end of cycling was −25.6 µm.

Analysis of a subvolume showed that the volume of the cell stack (that is, all materials between the current collectors) decreased during cycling (Fig. 4.8c), as also suggested by the observed displacement of the LSPS pellet coupled with the displacement of the current collector. Since the overall electrochemical process involved stripping lithium at one interface to form an interphase at the other, this net volume loss could be explained if the partial molar volume of lithium in the interphase was less than in lithium metal. Indeed, the partial molar volume of lithium in most battery cathodes and binary compounds is less than that in lithium metal, and these compounds are expected to be present within the interphase. As a result of this partial molar volume mismatch, the LSPS pellet and current collectors were displaced during cycling and there was a net decrease in

cell volume. The different magnitudes of the displacements within the LSPS occurred because the lithium electrodes at the edges of the cell were thinner, resulting in less interphase growth at these locations.

The observation of cell-volume shrinkage is different from that expected for Li/SSE/Li symmetric cells that undergo only lithium plating/stripping, as there would be no partial molar volume mismatch between the electrodes. Importantly, however, these results are relevant for designing full cells that contain a lithium metal anode and a cathode material since lithium has a lower partial molar volume in most cathode materials than in lithium metal, which will result in an overall reduction in cell volume during discharge. Our results highlight the chemo-mechanical challenges in creating full cells with controlled stack pressure throughout cycling, and they also indicate that commonly studied Li/SSE/Li symmetric cells are not entirely representative of the chemo-mechanical conditions present in full cells.

4.6 Conclusions

This investigation revealed the dynamic evolution of lithium interfaces in SSBs and directly showed that the loss and reconfiguration of interfacial contact was the critical factor that caused cell failure. The chemo-mechanical phenomena observed herein are expected to play important roles during the operation of SSBs on the basis of a wide variety of SSE chemistries beyond LSPS, as supported by the experiments with LPSC. Contact evolution/current constriction and volumetric changes are inherent challenges in SSBs, and nearly all SSEs decompose to some extent to form an interphase. These results, along with continued use of operando X-ray tomography and other such techniques, will help to guide

the development of SSBs with high energy densities and long lifetimes. In particular, the dynamics of lithium filament growth and the effects of incorporating different composite cathodes are key scientific aspects that require greater understanding for the successful integration of lithium metal within SSBs. Considering the wider application of this characterization method, different SSEs will exhibit different extents of X-ray attenuation, which will affect the contrast at interfaces; furthermore, the observation of dynamic processes would benefit from faster tomographic scan times (<7 min). It is also important to study how volume change mismatches between electrodes in full-cell architectures can alter mechanical stress throughout the cell. Material displacements, localized stress variations and the loss of stack pressure caused by introducing a cathode could have an impact on contact at the Li/SSE interface, and thus the electrochemical performance of full SSBs.

CHAPTER 5. HOW ELECTROCHEMCIAL PARAMETERS IMPACT LITHIUM METAL PENETRATION THROUGH SOLID-STATE ELECTROLYTES

5.1 Introduction

As discussed in Chapter 1, SSBs are challenged by non-uniform lithium deposition that manifests as lithium filaments propagating through the SSE to form a short circuit. While this phenomenon occurs in SSEs that form stable interphases against lithium metal, it is strongly dependent on the electrochemical conditions that are applied to the cell. Over the past five years, the SSB community has emphasized improving the current density that a cell can operate at before a short circuit forms. Numerous methods to enhance the rate performance have been proposed, including electrolyte composition and processing, as well as a variety of interfacial modifications that facilitate deposition.

While great strides have been made to improve the rate performance of Li/SSE interfaces, a key challenge is that there is currently no standard electrochemical procedure that can be used to compare between different studies. The most widely used tool is the critical current density (CCD) test, which involves plating and stripping Li/SSE interfaces while increasing the current density after a predetermined number of cycles. However, the CCD has many issues that makes it difficult to compare between studies[162]. Firstly, there is no standardized CCD protocol that is used between all studies. For example, some studies use a fixed cycle time for every current density tested, while other studies normalize the areal capacity for all current densities. Some studies apply a current density for only

one cycle before proceeding to the next step, while others allow the cell to run for many cycles at each current density. Secondly, the geometry of the experimental setup, such as the SSE thickness, electrode areas, and electrode thicknesses, can significantly impact the CCD. These discrepancies, among others, have made it challenging to compare CCD values.

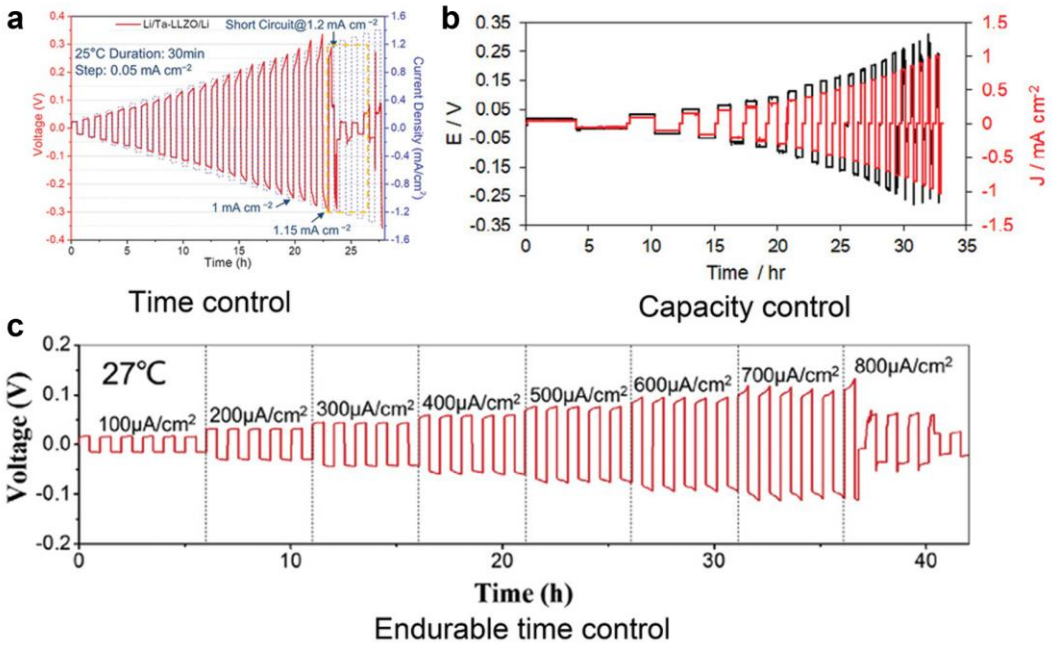

Figure 5.1. Effects of different CCD protocols on the measure CCD value. **a)** Time controlled CCD uses a fixed time for each cycle. The amount of lithium transported in each cycle thus increases over time as the current density is increased, and often results in a lower CCD value. **b)** Capacity controlled CCD uses a normalized capacity for each cycle to create a fair comparison between current densities. **c)** Some CCD protocols apply each current density for many cycles instead of just one, which affects the resulting CCD value. Adapted with permission from reference[162]. Copyright 2021 John Wiley & Sons, Inc.

Efforts toward reducing the prevalence of lithium penetration and short circuiting in lithium metal SSBs have primarily emphasized the importance of plating/stripping rates in dictating cell stability, which can be characterized by the CCD. This prevailing focus on the CCD has overshadowed another important electrochemical parameter: the amount of

lithium (i.e., areal capacity) that can be stably plated and stripped in each cycle. The general effect of areal capacity on cell stability has been previously observed; for instance, CCD measurements vary when using different cycle times (Fig. 5.1), suggesting that plating/stripping larger amounts of lithium capacity makes cell failure more likely. Critically, however, the impact of areal capacity on filamentary growth and short circuiting has not been systematically investigated and quantified. Furthermore, many studies that probe plating/stripping behavior use limited areal capacities that are well below the commercial requirements of at least 3 mAh cm^{-2} for high-energy cells. Given the importance of reaching high areal capacities while also operating at high current densities, there is a need to carefully examine the effects of cycling capacity on the stability of the lithium electrode in SSBs.

The study discussed in this chapter was published in *ACS Applied Materials and Interfaces* in 2022, and investigated the relationships between current density, areal capacity, and plating/stripping stability in lithium metal SSBs with the argyrodite SSE Li_6PS_5Cl. Conventional CCD measurements were compared to results in which lithium was continuously plated in one direction at different current densities. These results showed that continuous plating eventually caused short circuits even at current densities far below the CCD. For instance, short circuits formed at ~1/4 of the measured CCD (2.4 mA cm^{-2}) when plated for long enough. Analysis of many cells allowed for the identification of "threshold capacities" at various current densities, below which lithium could be reversibly plated and stripped over many cycles. Mechanistically, these results suggest that lithium filaments form over a wide range of current densities, but they can be reversibly stripped as long as they do not form catastrophic short circuits. Together, these findings reveal the

effects of areal capacity on lithium short circuiting, representing an important advance in the understanding of SSB behavior.

5.2 Limitations of the Critical Current Density

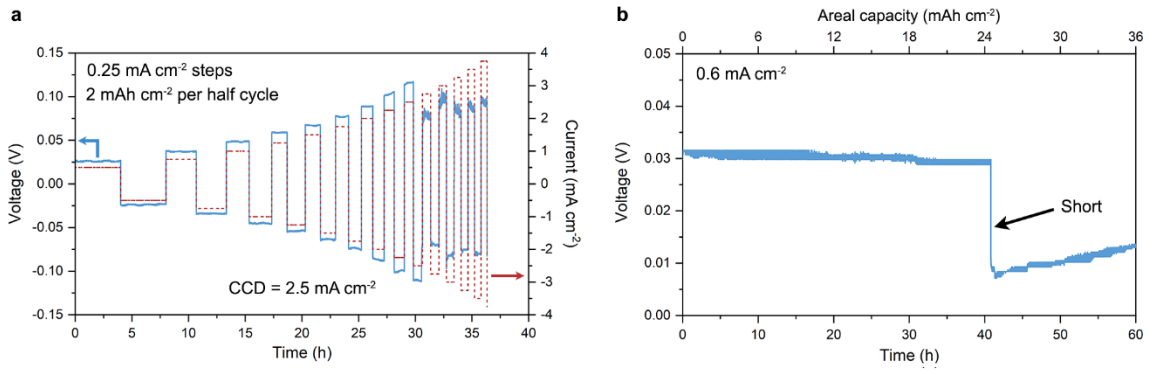

Figure 5.2. a) Critical current density test of a symmetric Li/LPSC/Li cell. The initial current density was 0.5 mA cm^{-2}, and the current density was increased in 0.25 mA cm^{-2} steps after each cycle. The half-cycle capacity was 2 mAh cm^{-2}. The CCD for this cell was 2.5 mA cm^{-2}. **b)** Continuous plating at one interface in a Li/LPSC/Li cell at 0.6 mA cm^{-2}. A short circuit formed after plating over 24 mAh cm^{-2} (∼120 μm of lithium metal plated). Both cells were assembled using an SSE fabrication pressure of 375 MPa and a stack pressure of 15 MPa.

Understanding current density limits is critical for designing commercial SSBs, which must be able to plate at least 3 mAh cm^{-2} of lithium at current densities greater than 3 mA cm^{-2}. CCD experiments were conducted using symmetric Li/LPSC/Li cells to determine the rate capabilities of optimized cells that were assembled with an SSE fabrication pressure of 375 MPa and a stack pressure of 15 MPa. The current density was ramped in 0.25 mA cm^{-2} steps starting at 0.5 mA cm^{-2}, and 2 mAh cm^{-2} of lithium was plated during each half-cycle. A representative cell cycled using this procedure is shown in Figure 5.2a. The CCD of this cell was 2.5 mA cm^{-2}, and the average CCD for five cells using the same conditions was 2.4 ± 0.4 mA cm^{-2}. In the context of the wider literature,

this CCD value is among the highest reported for SSBs at room temperature with unmodified interfacial chemistry and flat interfaces (nonporous electrodes), as shown in Fig. 5.3.

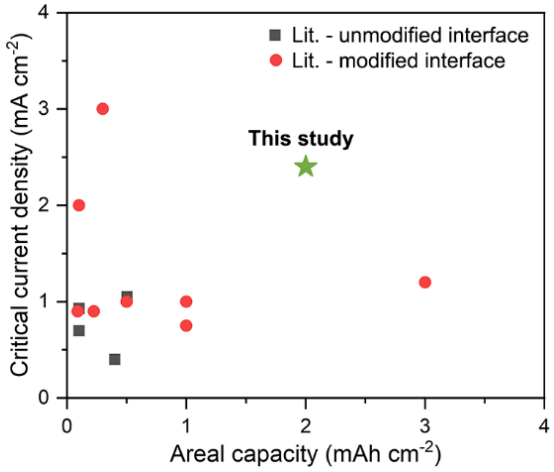

Figure 5.3. Plot of the measured CCD versus areal capacity per half cycle used to compare the CCD measurement from the current study (green star) compared to other reports. Red circles represent data points that were collected at elevated temperatures or that featured a modified Li/SSE interface to enhance performance. Black squares represent data for unmodified interfaces at room temperature. For studies where cycle duration was controlled by time (instead of capacity), the areal capacity in this plot was taken from the final cycle where failure occurred.

The sensitivity of the CCD test to electrochemical parameters makes it challenging to understand whether there is a current density below which uniform plating occurs. To highlight this fact, a symmetric cell was constructed and continuously plated lithium at one interface using a current density of 0.6 mA cm^{-2} (Fig. 5.2b), which was far below the measured CCD. After plating for over 40 h (corresponding to 100+ μm of lithium), the cell failed due to a short circuit. This experiment revealed that lithium can still grow in a filamentary manner to penetrate the SSE when given enough time at current densities that

are less than 1/4 of the measured CCD, and highlighted that CCD tests do not provide complete insight into the rates at which nonuniform deposition occurs.

5.3 Threshold Capacity as a Metric to Evaluate Plating in SSBs

Building on the experiment presented in Fig. 5.2b, a testing protocol based on continuous plating until short circuit formation was used to probe the susceptibility of symmetric cells to lithium filament penetration under an array of electrochemical and assembly conditions. The cumulative areal capacity of lithium plated until the point of short circuiting was used as a metric to compare performance among cells, and this value was denoted as the threshold capacity for a given cell. Cells with six different pairs of electrolyte fabrication pressures and current densities were probed, with five cells being tested for each pair of conditions (a total of 30 cells). Repeated tests were necessary to evaluate the average effects of current density and cell fabrication conditions on short circuiting. Figure 5.4a is a plot of the threshold capacity as a function of current density for these 30 cells; the corresponding electrochemical curves are shown in Fig. 5.4b, and Table 5.1 lists the average threshold capacity values measured. Half of the cells were assembled using an electrolyte fabrication pressure of 125 MPa (red circles), while the other half were assembled with a fabrication pressure of 375 MPa (blue circles). The fabrication pressure was applied during cold-pressing of the pellet before cell testing, and it affected the density of the SSE pellet. The stack pressure applied to all cells during testing was 15 MPa. Figure 5.4c shows that good interfacial contact was established between the LPSC layer and the lithium electrode under these conditions.

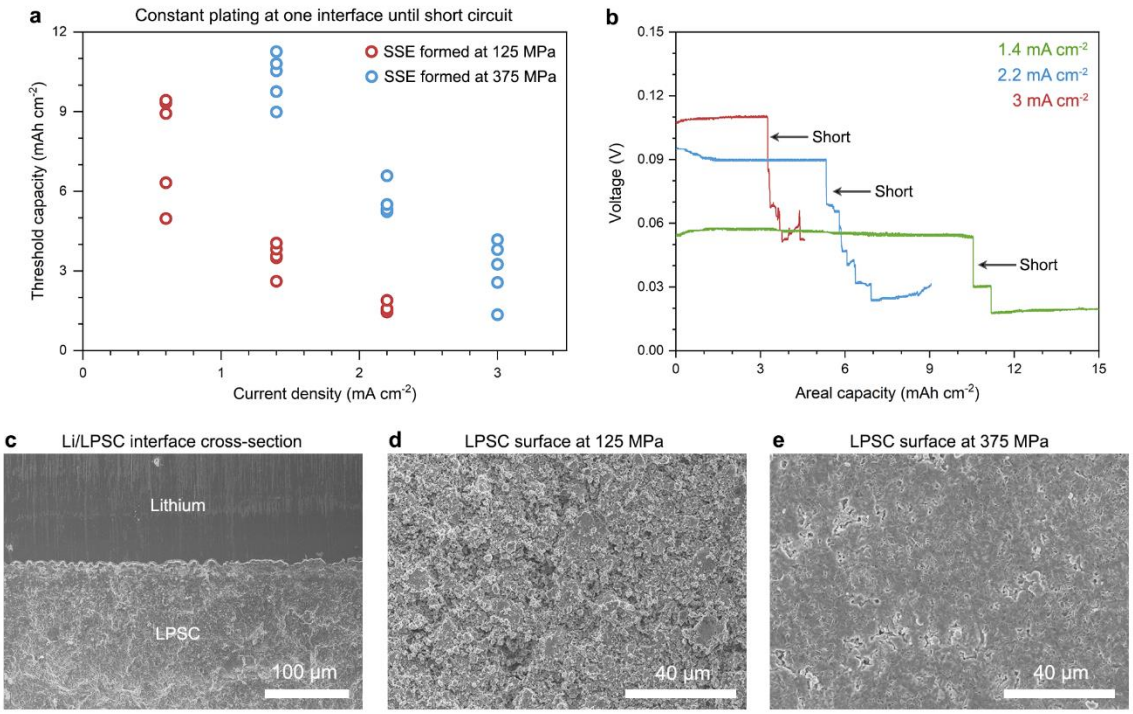

Figure 5.4. a) Plot of the threshold capacity as a function of current density for two electrolyte fabrication pressures: 125 MPa (red circles) and 375 MPa (blue circles). Five symmetric cells were tested for each current density and/or fabrication pressure. **b)** Example electrochemical curves of continuous plating experiments for the cells in **(a)**. **c)** SEM image of the cross-section of a pristine Li/LPSC interface. **d, e)** SEM images showing the morphology of LPSC pellets pressed at 125 and 375 MPa.

The data in Fig. 5.4a provided insight into a number of trends relevant to lithium metal penetration through SSEs. First, all 30 cells eventually short circuited despite the range of current densities tested (0.6–3.0 mA cm^{-2}), including many below the measured CCD. Second, the cells tested at higher current densities exhibited lower threshold capacities before short circuiting, indicating greater prevalence of nonuniform lithium deposition that has been demonstrated in other studies. Third, the electrolyte fabrication pressure (and thus SSE density) played an important role in determining the threshold capacity. At a given current density, every cell assembled using the higher electrolyte fabrication pressure (375 MPa) was able to plate more lithium compared to the lower

fabrication pressure (125 MPa). For example, the average threshold capacity that could be plated at 1.4 mA cm^{-2} was 3.5 mAh cm^{-2} for SSE pellets formed at 125 MPa. Increasing the fabrication pressure to 375 MPa resulted in a substantially higher average threshold capacity of 10.3 mAh cm^{-2}. SEM images of the surface morphology of LPSC pressed at 125 and 375 MPa (Fig. 5.4d,e) showed that the porosity decreased at higher pressures. This observation was supported by measurements of the pellet geometric density, which yielded 73% relative density at 125 MPa, and an increased relative density of 83% at 375 MPa. SSEs with higher density have fewer void spaces into which lithium can electrochemically grow or be mechanically deformed to fill during the application of stack pressure.

Table 5.1. Summary of average threshold capacities measured in Figure 5.4.

Fabrication pressure (MPa)	**Current density (mA cm^{-2})**	**Average threshold capacity (mAh cm^{-2})**
125	0.6	7.8 ± 2.0
125	1.4	3.5 ± 0.5
125	2.2	1.6 ± 0.2
375	1.4	10.3 ± 0.9
375	2.2	5.6 ± 0.6
375	3.0	3.0 ± 1.1

With five cells tested for each fabrication pressure/current density pair, the plot in Fig. 5.4a also shows that there was variation of the threshold capacity among cells despite using the same assembly procedure. For example, the cells fabricated at 125 MPa and plated at 0.6 mA cm^{-2} had threshold capacities ranging from 5.0 to 9.4 mAh cm^{-2}. This variation could be related to differences in pore distribution and morphology of the interfaces in different cells, which can affect the initial uniformity of the Li/LPSC interface

after the application of stack pressure. Variation could also be attributed to the nature of crack formation and lithium propagation across the electrolyte, which will depend partially on the locations of defects that differ even under the same assembly conditions due to their stochastic nature. Regardless of the mechanisms involved, the observed variation in threshold capacity indicates that collecting data from multiple cells is important to correctly assess the behavior of Li/SSE interfaces in both research and industrial settings. Practical lithium metal SSBs must account for such cell-to-cell variations and operate under conditions that are safe for the full range of conditions required to ensure sufficient quality control over cell lifetime. This variance may be a distinct challenge for SSBs due to the presence of defects in SSEs like pores, cracks, and grain boundaries that are absent in liquid electrolytes and likely cannot be precisely controlled between cells.

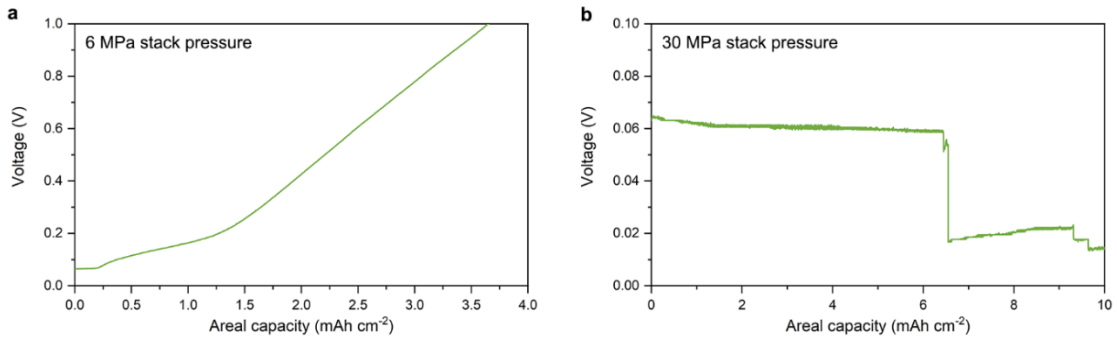

Figure 5.5. Continuous plating at 1.4 mA cm^{-2} with an SSE fabrication pressure of 375 MPa and a stack pressure of **a)** 6 MPa and **b)** 30 MPa.

It was also found that stack pressure plays a major role in resisting filament formation, consistent with other studies. An optimal stack pressure for symmetric cells in this work was found to be 15 MPa, which was the value used for all cells in Figs. 5.2 and 5.4. A lower stack pressure of 6 MPa resulted in voltage polarization due to voiding at the stripping interface (Fig. 5.5a), which could be attributed to less lithium deformation.

Plating at 30 MPa resulted in less areal capacity transported before short circuiting (Fig. 5.5b). This behavior was likely caused by the higher pressure driving greater quantities of lithium into the SSE before plating, as demonstrated by Doux et al..

The data presented in Fig. 5.4 focused on understanding the resistance to lithium metal penetration and short circuiting without the effects of previous stripping. Since stripping is an integral part of a real lithium metal battery, it was important to investigate the following: (1) the effectiveness of stripping toward dissolving existing filaments, (2) how contact loss during stripping impacted subsequent plating, and (3) how the areal capacity used during cycling impacted cell stability. To understand these issues, cycling experiments were conducted using the optimized cell assembly with a fabrication pressure of 375 MPa and stack pressure of 15 MPa. The same current densities (1.4, 2.2, and 3.0 mA cm^{-2}) were used to facilitate comparison to the data in Fig. 5.4a.

5.4 Relationship Between Threshold Capacity and Cycling Stability

Figure 5.6 shows symmetric cell cycling using a half-cycle capacity of 2.0 mAh cm^{-2}. This areal capacity was chosen because it was less than the threshold capacity in all cases (Fig. 5.4a and Table 5.1), ensuring that short circuiting would not occur during the first half-cycle. Figure 5.6a shows that cells cycled at 1.4 and 2.2 mA cm^{-2} exhibited excellent stability for 100 cycles without short circuiting or voltage polarization associated with poor stripping. Cycling these cells substantially increased the cumulative amount of lithium that could be plated before failure compared to the continuous plating experiments in Fig. 5.4a. For example, the average plating threshold capacity at a current density of 2.2 mA cm^{-2} was 5.6 mAh cm^{-2}, whereas cells cycled at 2.2 mA cm^{-2} using 2.0 mAh cm^{-2} per

half-cycle were able to cumulatively plate over 200 mAh cm^{-2} at one interface without short circuiting (Fig. 5.6a). Since filaments can be formed at current densities well below the CCD, these experiments strongly indicated that stripping was effective at removing previously grown lithium filaments even at relatively high current densities and capacities. However, contrasting behavior was observed for cells cycled with the same cycle capacity of 2.0 mAh cm^{-2} with the higher current density of 3.0 mA cm^{-2}, as shown in Fig. 5.6b. Instead of extended lifetime, these cells rapidly failed in the second half-cycle when plating began at the freshly stripped interface. Notably, the half-cycle capacity of 2.0 mAh cm^{-2} was 66.7% of the average threshold capacity for plating at 3.0 mA cm^{-2}, compared to 19.4% for 1.4 mA cm^{-2} and 35.7% for 2.2 mA cm^{-2}. This behavior suggested that using a capacity well below the average threshold capacity for short circuiting mitigated the risks of symmetric cell failure, but cycling with capacities near the threshold led to rapid short circuiting.

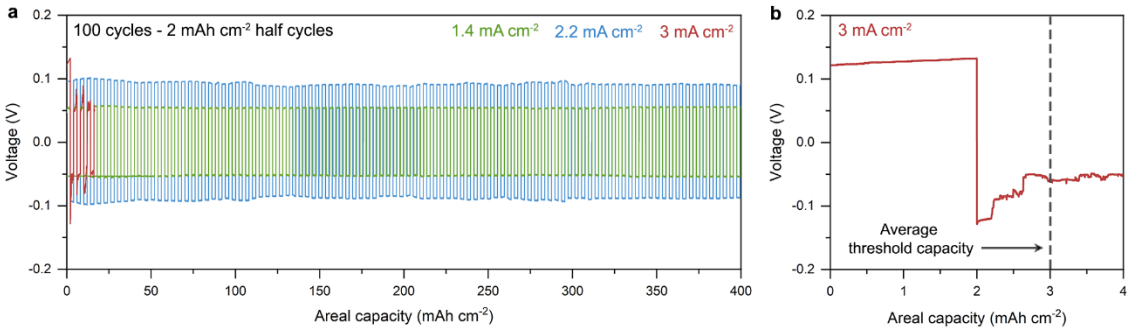

Figure 5.6. a) Cycling of symmetric Li/LPSC/Li cells at current densities of 1.4 mA cm^{-2} (green), 2.2 mA cm^{-2} (blue), and 3.0 mA cm^{-2} (red) with half-cycle areal capacities of 2.0 mAh cm^{-2}. **b)** Magnified plot from the cell cycled at 3.0 mA cm^{-2} in **(a)**. The dashed line represents the average threshold capacity for cells plated at 3.0 mA cm^{-2}, as presented in Fig. 5.4a and Table 5.1.

The effects of how approaching the threshold capacity in a half-cycle affects cycling stability were investigated next. A symmetric cell was cycled at 1.4 mA cm^{-2} with a larger half-cycle capacity of 6.0 mAh cm^{-2} (Fig. 5.7a); this half-cycle capacity was 58.2% of the average threshold capacity found in Fig. 5.4a. Using these cycling conditions, it was possible to reversibly plate 6.0 mAh cm^{-2} of lithium in each half-cycle for a total capacity of over 550 mAh cm^{-2}, demonstrating similar stability as shown in Fig. 5.6a. However, Fig. 5.7b shows that increasing the half-cycle capacity to 9.0 mAh cm^{-2} (87.3% of the average threshold capacity) severely reduced the cell lifetime, with a short circuit forming in the first cycle. Similar stability issues were observed in cells cycled at 2.2 mA cm^{-2} with 5.0 mAh cm^{-2} transported per half-cycle (89.3% of the average threshold capacity), as shown in Fig. 5.7c.

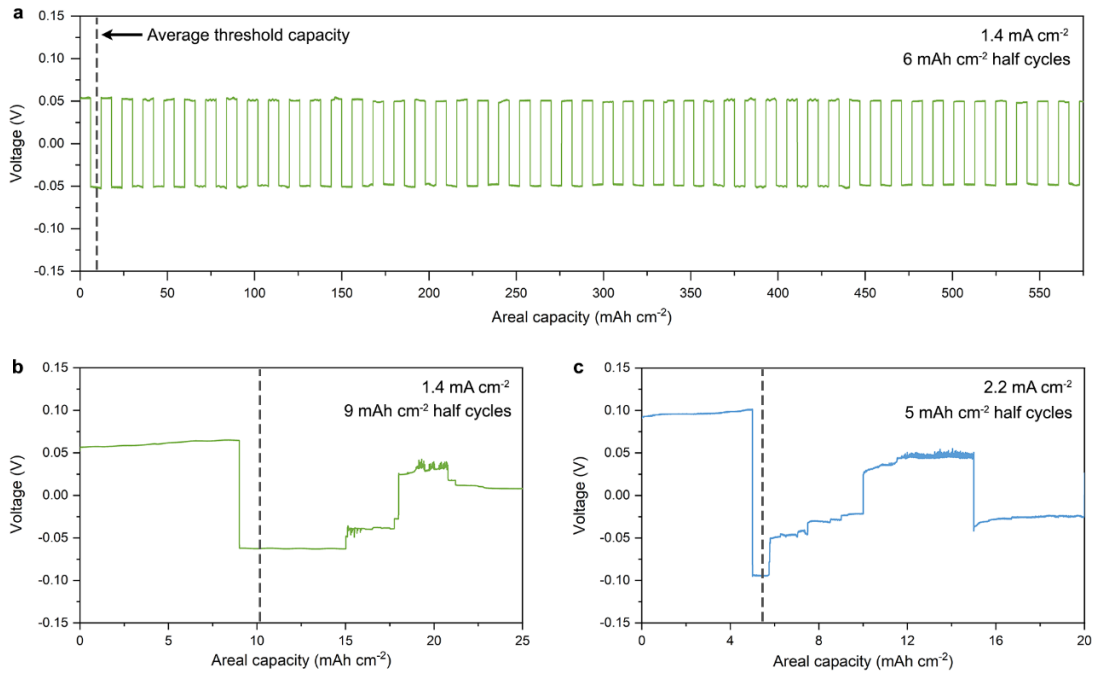

Figure 5.7. a) Stable symmetric cell cycling at 1.4 mA cm^{-2} using a half-cycle capacity of 6.0 mAh cm^{-2}. (b) Unstable cycling at 1.4 mA cm^{-2} when the half-cycle capacity was increased to 9.0 mAh cm^{-2}. (c) Unstable cycling at 2.2 mA cm^{-2} using a half-cycle capacity of 5.0 mAh cm^{-2}. The dashed line in each plot represents the average threshold capacity for the corresponding current density as measured in Fig. 5.4.

These extensive results from symmetric cells show that cell stability was linked to the amount of lithium that is plated each cycle, which is critical information that is usually absent from conventional CCD measurements. Understanding the average threshold capacity at a given current density allows for tuning of the cycling capacity to substantially increase the lifetime of symmetric cells. Furthermore, these cells could be reversibly cycled without polarization and contact loss caused by stripping, indicating that lithium was sufficiently replenished to maintain contact at the interfaces at current densities up to 2.2 mA cm^{-2}.

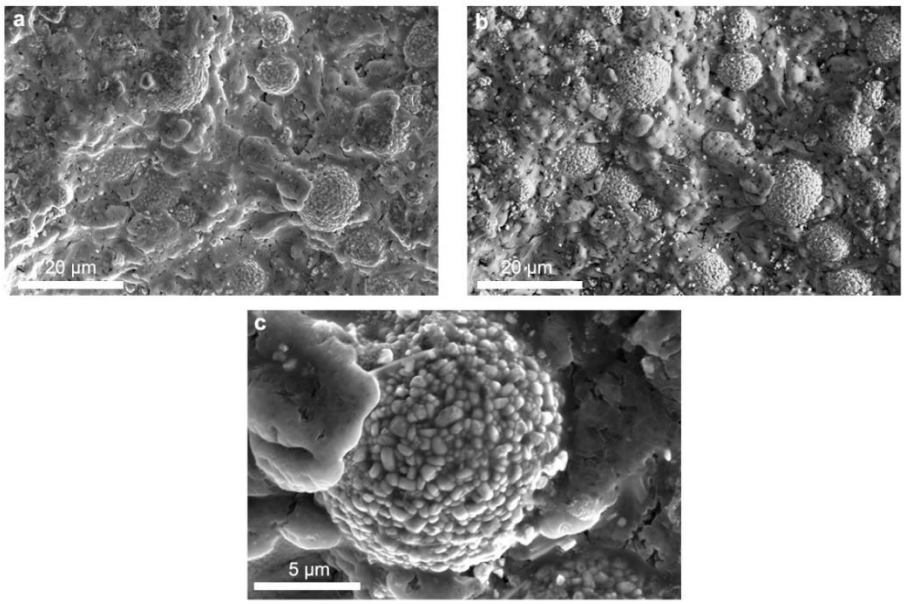

Figure 5.8. SEM image of the composite cathode microstructure using **a)** a secondary electron detector and **b)** a backscattered electron detector. **c)** Magnified image of a polycrystalline NMC811 particle collected using secondary electrons.

The data presented thus far leveraged symmetric cells to probe Li/SSE interfaces. However, these results must be connected to data from full SSBs that incorporate both a lithium metal anode and a cathode, as there may be fundamental differences in lithium

metal penetration when plating/stripping in a full cell compared to symmetric cells. To compare to symmetric cells, full cells were constructed with composite cathodes consisting of 70 wt % $LiNi_{0.8}Mn_{0.1}Co_{0.1}O_2$ (NMC811), 27.5 wt % LPSC, and 2.5 wt % carbon black. SEM images of the pressed composite cathode microstructure are shown in Fig. 5.8. Using five full cells, the continuous plating symmetric cell experiments in Fig. 5.4 were replicated by applying a high current density of 2.0 mA cm^{-2} during the first charge. The theoretical areal capacity loading of the cathode was 6.0 mAh cm^{-2} in these experiments to ensure that a short circuit would occur before the cathode was depleted of lithium. Figure 5.9a shows a cell charged under these conditions, which was able to plate 2.5 mAh cm^{-2} before shorting; the average threshold capacity for the five cells was 2.8 mAh cm^{-2}.

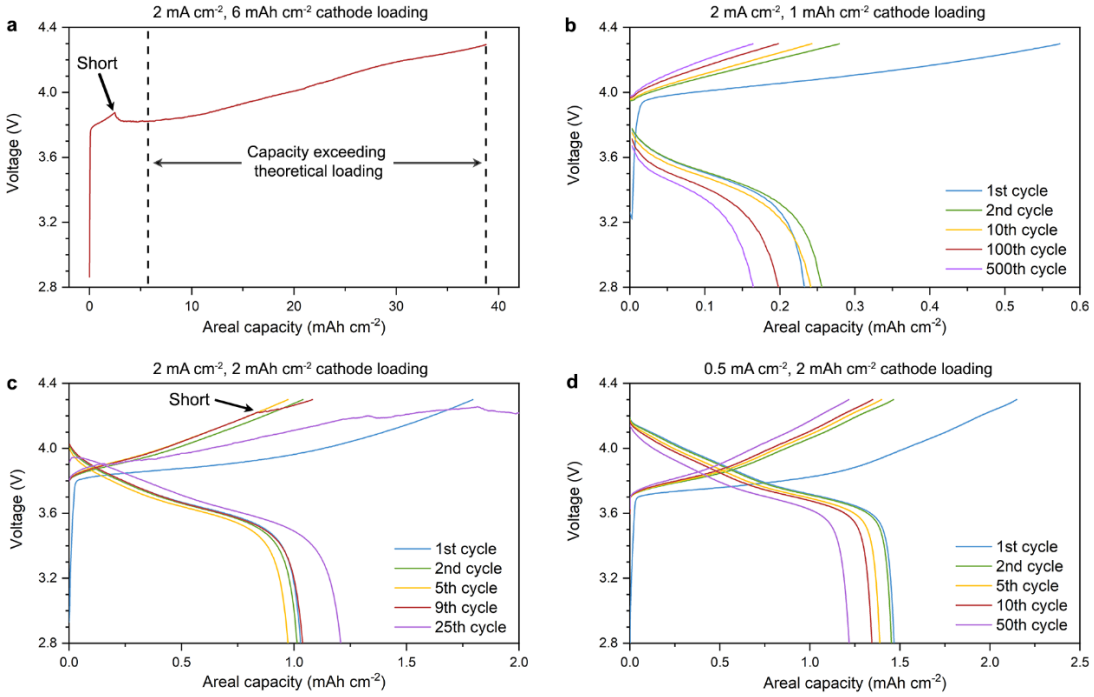

Figure 5.9. a) Charging a Li/LPSC/NMC811 full cell at 2.0 mA cm^{-2} with a cathode loading of 6.0 mAh cm^{-2} to form a short circuit during the first charge. **b)** Cycling a full cell at 2.0 mA cm^{-2} using a lower cathode loading of 1.0 mAh cm^{-2}. **c)** Cycling a full cell at 2.0 mA cm^{-2} using a cathode loading of 2.0 mAh cm^{-2}. **d)** Cycling a full cell at 0.5 mA cm^{-2} with a loading of 2.0 mAh cm^{-2}. The SSE fabrication pressure was 375 MPa, and the stack pressure was 16 MPa for all cells.

The charging curve in Fig. 5.9a showed the typical short-circuiting behavior that was observed in the full cells. The short circuits in the full cells were identified by a sudden drop in cell voltage, which was also sometimes followed by a slow decrease in voltage that should not occur if lithium was being extracted from the cathode. The cell voltages eventually continued to increase and reached the voltage limit, but the cells exhibited large charging capacities substantially exceeding the theoretical areal capacity of the cathode. For example, the cell in Fig. 5.9a showed an excess capacity of 33 mAh cm^{-2} beyond the 6.0 mAh cm^{-2} theoretical cathode capacity. This behavior indicated that the full-cell failure observed was a form of "soft shorting". Similar short-circuit voltage profiles have also been reported by other groups.

With an average threshold capacity established for these full cells charged at 2.0 mA cm^{-2}, full cells were cycled with lower cathode loadings to intentionally reduce the plated capacity to be below the threshold. If the relationship between capacity and plating/stripping stability for full cells was similar to symmetric cells, then full cells with lower cathode loadings should have had greatly enhanced lifetimes. It is noted that cycling at 2.0 mA cm^{-2} with lower cathode loadings will increase the cathode C-rate and result in a lower fraction of the theoretical capacity being accessed, as well as higher overpotentials. Fig. 5.9b shows charge–discharge curves for a cell cycled at 2.0 mA cm^{-2} with a cathode loading of 1.0 mAh cm^{-2}. Due to the high C-rate of 2C, the first charge only reached 58% of the theoretical capacity, and the first cycle had a low Coulombic efficiency of 40.6%. These penalties limited the average amount of lithium plated in each charge to be 0.19 mAh cm^{-2}, which was far below the average threshold capacity of 2.8 mAh cm^{-2}. Similar to the symmetric cells, this full cell was capable of cycling 500 times without the formation of a

short circuit. The cumulative lithium plated over these 500 cycles was 94 mAh cm^{-2}, which was much larger than the average threshold capacity and demonstrated the cell's reversibility, albeit at low areal capacities.

Increasing the cathode loading to 2.0 mAh cm^{-2} enabled a higher fraction of the theoretical cathode loading to be accessed at the same current density of 2.0 mA cm^{-2} (Fig. 5.9c), but the cell still had a low initial CE of 57.3%. As a result, the average capacity plated per charge in the first eight cycles was 1.09 mAh cm^{-2}. Despite being cycled at areal capacities well below the average threshold capacity of 2.8 mAh cm^{-2}, this cell began to short in the ninth cycle and continued to gain excess charge capacity during subsequent cycles. However, the cumulative capacity plated before the short circuit initiated in cycle 9 was ~9.5 mAh cm^{-2}, demonstrating a modest improvement over the threshold capacity. Cycling a cell at 0.5 mA cm^{-2} with the same cathode loading resulted in over 50 cycles without any short circuiting, as shown in Fig. 5.9d.

These data revealed important information about plating/stripping behavior in full cells. First, it appeared that full cells with NMC811 cathodes are prone to short circuiting at lower areal capacities compared to symmetric cells. In this case, plating an average areal capacity of 2.8 mAh cm^{-2} at 2.0 mA cm^{-2} in full cells led to failure, whereas symmetric cells tested at 2.2 mA cm^{-2} could withstand an average areal capacity of 5.6 mAh cm^{-2}. Second, the benefits of using a half-cycle capacity below the average threshold capacity may have been diminished for full cells. While cycling without a short circuit was possible in full cells when using low half-cycle capacities of 0.19 mAh cm^{-2} (6.8% of the average threshold capacity), increasing the half-cycle capacity to just 38.9% of the average

threshold capacity only yielded moderate improvements in cell lifetime and did not prevent short circuiting.

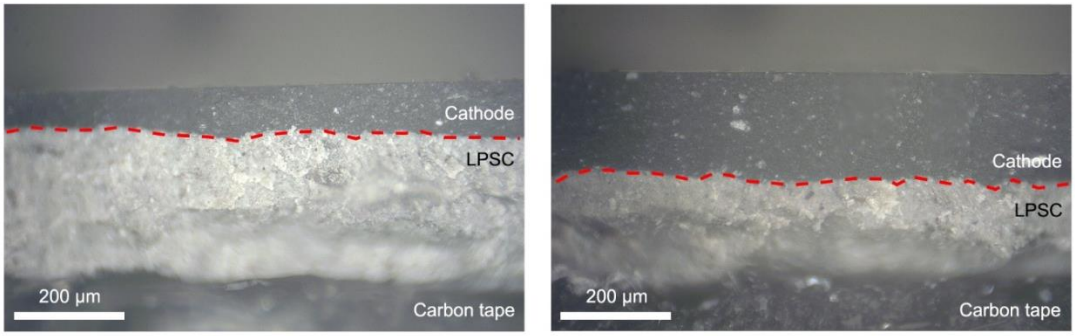

Figure 5.10. Optical images of the cathode/LPSC interface, showing how the cathode thickness varied at different locations.

It is unclear if the diminished performance of full cells compared to symmetric cells was a consequence of differences in cell assembly or if there were fundamentally different lithium plating/stripping mechanisms in these different cell configurations. In this study, symmetric cells benefitted from having a relatively thick lithium electrode (~0.3 mm) on each side of the electrolyte, which helped distribute pressure uniformly across the interface since lithium deforms readily. Full cells have a more rigid composite cathode, which could alter the stress distribution at the interface despite using the same cell housings as symmetric cells. Additionally, the composite cathode thickness could vary across the interface in some samples, as shown in Fig. 5.10. Therefore, it is possible that the inferior full-cell performance was due to cell engineering and not electrochemical mechanisms. On the other hand, there could be changes in lithium plating/stripping behavior due to different potential distribution across the cells, as well as chemo-mechanical effects that resulted from the expansion and contraction of cathode active material that were not present in

symmetric cells. Detailed characterization of plating/stripping in full cells using pure lithium metal anodes is thus urgently needed to understand these differences, which can then guide engineering of full cells for improved performance.

5.5 Conclusions

This work further developed an understanding of the relationships between current density, capacity, and plating/stripping stability in SSBs. It was found that given enough time, lithium metal penetration through the SSE occurs and caused short circuits even at current densities much lower than the CCD. The average threshold capacity was used as a parameter to gauge resistance to short circuiting, and a relatively large dataset revealed that the average threshold capacity was strongly impacted by current density, SSE fabrication pressure, and stack pressure. This behavior indicated that lithium filaments can grow either by fracturing the SSE or by propagating through porous regions within the SSE at a variety of current densities. These results suggested that completely uniform lithium deposition was not attained over the entire interface even at relatively low current densities, which was likely due to the presence of unavoidable interfacial defects.

When symmetric cells were cycled using a plating capacity much lower than the threshold capacity, they exhibited excellent stability at current densities up to 2.2 mA cm^{-2}. However, increasing the plating capacity closer to the threshold capacity resulted in rapid cell failure. These findings suggest that the amount of lithium plated and stripped can affect the morphology of lithium near the interface, and they underscore the importance of controlling areal capacity transported in each cycle to ensure long cell lifetime. Finally, full cells were fabricated and tested using similar experiments to understand how these

concepts apply to practical SSBs. While similar phenomena were observed in the relationship between areal capacity and short circuiting, it was also found that full cells were more susceptible to short circuiting at lower areal capacities transferred, motivating the need for future studies to elucidate potential mechanistic differences.

The results herein represent a systematic investigation that shed light on the role of areal capacity transferred in determining the short circuiting behavior of SSBs. CCD measurements widely used in the SSB literature are important, but they do not provide a full picture of interfacial stability for a given material and set of conditions. In particular, if CCD measurements are performed with low areal capacity transferred (<1 mAh cm^{-2}) per half-cycle, this can artificially inflate the CCD since higher areal capacities are necessary for high-energy-density full-cell SSBs. Thus, it would be ideal if both average CCD values and threshold capacity measurements (or another similar metric) are reported for new materials and SSB configurations in future studies.

CHAPTER 6. ELECTROCHEMICAL MECHANISMS OF ANODE-FREE SOLID-STATE BATTERIES

6.1 Introduction

Lithium metal anodes have received considerable attention in SSBs. In lab-scale experiments, relatively thick lithium metal foils (~0.1 to 0.5 mm) are typically used to reduce the complexity of cell assembly. However, no commercial battery would use a foil this thick, as it would occupy too much volume. Instead, manufacturing cells with excess lithium metal would use a thickness of ~10-25 μm. In an ideal scenario, lithium metal SSBs would have no excess lithium present in the assembled state. This configuration is called an anode-free battery, and is possible because the cathode typically contains lithium that can be used to form the lithium metal *in situ* onto the current collector during charging. Anode-free SSBs have two key advantages over using an excess lithium foil as the anode. First, there is an increase in the cell-level energy density of ~10-15% as a result of eliminating the volume of excess lithium foil (Fig. 6.1). Second, manufacturing thin lithium foils is complex and expensive due to its high reactivity and mechanical properties. Anode-free SSBs can avoid this problem, offering the opportunity to reduce costs and simplify the production line.

While there is great interest in anode-free solid-state batteries, achieving stable cycling in these cells is fundamentally challenging. One reason is that the lithium metal anode must be formed *in situ* by depositing onto a substrate at high current densities. Lithium metal foils are soft and can easily deform to contact the SSE, whereas it may be

difficult to establish and maintain good contact between a current collector and SSE. Another issue is that the Coulombic efficiency must be very high, as the only source of lithium ions is the cathode. Lithium metal anodes in both SSBs and liquid electrolytes are known to have lower Coulombic efficiencies, making this problem hard to overcome.

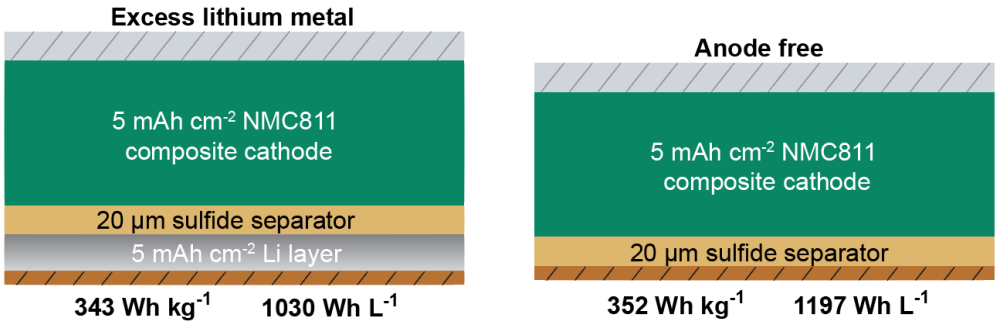

Figure 6.1. Schematics of an SSB with an excess lithium layer (left) and an anode-free configuration (right). The calculated specific energy and energy density for both architectures are labeled.

Because of these limitations, only a few recent studies have focused on evaluating the performance of SSBs with anode-free configurations. Wang et. al demonstrated the ability to plate and strip > 3 mAh cm^{-2} at interfaces between bare current collectors and LLZO. However, the cells were ran at relatively low current densities and required hot pressing current collectors onto LLZO at > 900 °C to achieve stable plating and stripping. A different approach was developed by Samsung by incorporating a Ag-C layer between the current collector and SSE to facilitate uniform deposition. These cells exhibited extraordinary electrochemical performance, among the highest of any SSBs to date. Despite this state-of-the-art performance, these cells required the Ag-C layer to achieve cycling without short circuiting. An ideal anode free configuration would avoid using

mediator layers, and instead interface directly with the current collector in order to maximize cell energy and reduce costs.

In this chapter, the mechanisms of plating and stripping lithium metal in anode-free SSBs with the sulfide LPSC were investigated. Simple cold pressing of copper foil onto LPSC at 15 MPa enabled high performance during the initial *in situ* plating, with large amounts of lithium metal (>5 mAh cm^{-2}) deposited at a high current density of 1 mA cm^{-2}. Despite the impressive performance during the initial plating, it was found that non-uniform stripping of the lithium metal layer led to catastrophic contact loss and required re-nucleation in the subsequent plating step. The repeated process of non-uniform stripping and re-nucleation led to premature short circuiting. However, anode-free full cells were found to have comparable Coulombic efficiencies as full cells with thick lithium foils, suggesting that anode-free interfaces did not hinder capacity retention. Lastly, strategies to mitigate the detrimental effects of non-uniform stripping were explored and provided further insight into how anode-free interfaces can be stabilized.

6.2 Deposition of Lithium Metal at Cu/LPSC Interface

We first investigated the deposition behavior of lithium metal in anode-free Cu/LPSC/Li half cells to determine if commercially relevant amounts of lithium could be plated. In these half cells, a 10 µm thick copper current collector was cold pressed onto one side of a dense LPSC layer at ~15 MPa of stack pressure. A thick lithium metal foil was simultaneously pressed onto the other side of the LPSC to serve as the lithium source. Figure 6.2a shows a typical voltage profile when depositing lithium metal onto copper foil at 1 mA cm^{-2} in this cell assembly. The beginning of deposition exhibited a nucleation

overpotential associated with the initial formation of the lithium metal layer, which then stabilized to a voltage of -50 mV. Notably, this cell was able to plate over 6.5 mAh cm^{-2} before a short circuit formed, as indicated by the sudden step in the potential. Cross-sections of a similar sample tested under the same conditions showed that thick layers of lithium metal can be plated, as shown by the optical and SEM images in Fig. 6.2b,c.

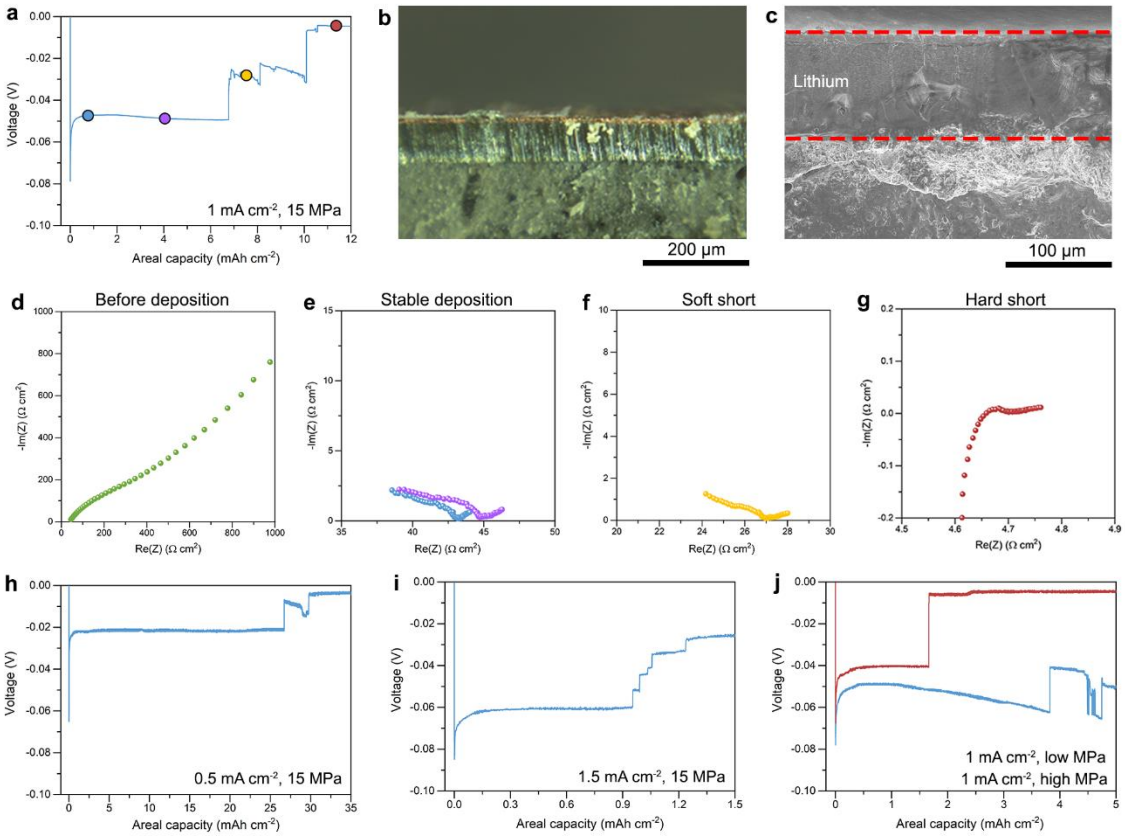

Figure 6.2. a) Deposition of lithium metal onto copper foil at 1 mA cm^{-2} in an anode-free Cu/LPSC/Li half cell with a stack pressure of 15 MPa. **b, c)** Optical and SEM images of thick lithium layers deposited at 1 mA cm^{-2}. **d-g)** EIS data gathered at different stages of the deposition in **(a)**. **h)** Depositing lithium metal onto copper foil at 0.5 mA cm^{-2} and 15 MPa. **i)** Depositing lithium metal onto copper foil at 1.5 mA cm^{-2} and 15 MPa. **j)** Depositing lithium metal onto copper foil at 1 mA cm^{-2} using stack pressures of 5 MPa (blue curve) and 30 MPa (red curve).

EIS measurements were taken periodically during the deposition shown in Fig. 6.2a. The impedance of the as-assembled cell was high (Fig. 6.2d), but was dramatically reduced after nucleating the lithium layer (Fig. 6.2e), and stayed relatively constant around this value during the remainder of deposition. After plating ~6.5 mAh cm^{-2}, an intermediate step in the voltage was observed with a corresponding decrease in impedance (Fig. 6.2f). This step could be associated with a phenomenon known as a "soft short", although the behavior of short circuits is not well defined in SSBs. After continuing to apply current, the voltage profile underwent additional steps towards 0 V. The final EIS measurement (Fig. 6.2g), captured at a cell potential of approximately -5 mV, showed that the impedance had continued to decrease and exhibited a different shape than the intermediate short circuit. In particular, the diameter of the semi-circle was reduced to only 0.1 Ω cm2, and the first ~10 data points had negative -Z'' values, indicating a transition to a more complete short circuit.

Additional experiments were conducted to understand how different conditions impacted electrochemical behavior during the first lithium deposition step. Figure 6.2h,i show the voltage profiles for deposition at 0.5 mA cm^{-2} and 1.5 mA cm^{-2}. Similar to symmetric cells with thick lithium foil electrodes, the current density played a key role in how much lithium capacity could be passed before a short circuit forms. Over 25 mAh cm^{-2} (>125 microns of Li) was plated at 0.5 mA cm^{-2}, whereas only 1 mAh cm^{-2} was possible at 1.5 mA cm^{-2}. It was also found that the stack pressure impacted anode-free deposition, as shown in Fig. 6.2j. Operating at lower stack pressure of 5 MPa resulted in less capacity being plated compared to the stack pressure of 15 MPa in Fig. 6.2a. Interestingly, a higher pressure of 30 MPa was also worse, despite increasing stack pressure typically enhancing

interfacial contact in SSBs. This could possibly be due to larger amounts of deformation of the deposited lithium into LPSC, creating more regions with higher effective current densities. However, future studies are required to fully assess the effects of stack pressure on anode-free deposition.

The ability to deposit > 5 mAh cm^{-2} at a relatively high current density of 1 mA cm^{-2} is remarkable given that the cell assembly only used cold pressing at moderate pressures to interface copper foil with the LPSC electrolyte. This result is contrasted with the challenges of interfacing an anode-free current collector with the oxide LLZO, which required the simultaneous application of very high temperatures and moderate pressures to form a viable interface. It is hypothesized that integrating copper with LPSC is possible at room temperature due to the softer mechanical properties of sulfides, especially compared to the hard and brittle nature of oxides like LLZO. The ability for the electrolyte to locally reconfigure its shape to better match the current collector could play a key role in developing high performance anode-free SSBs.

After demonstrating that large capacities of lithium can be deposited in both half cell anode-free configurations, characterization experiments were carried out using cryo-FIB/SEM to observe how the thickness and morphology of lithium varied at different locations of the anode/SSE interface. These experiments leveraged two important capabilities to provide detailed information about the deposition process. Firstly, the anode-free architecture facilitated FIB milling through the entirety of the lithium deposit due to the thinness of the copper foil (~10 μm). Secondly, milling at cryogenic temperatures was critical to maximize preservation of the lithium deposit thickness and morphology. To highlight these effects, two trenches were milled at different temperatures next to each

other on the same sample, as shown in Fig. 6.3. The left trench was milled at -145 °C, while the right trench was milled at 25 °C. Significant differences in lithium morphology were observed, with the room temperature cut exhibiting extensive porosity, beam damage, and lighter contrast.

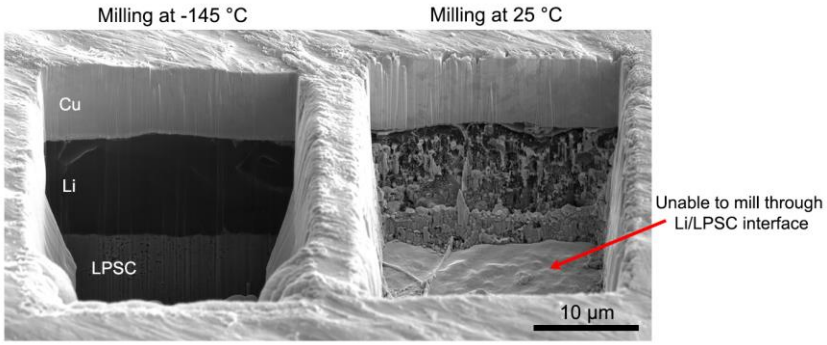

Figure 6.3. Comparison of FIB milling at different temperatures on the same sample. The left trench was milled at -145 °C, while the right trench was milled at 25 °C.

Figure 6.4 shows SEM images taken after cryo-FIB milling at different positions on three distinct samples. The first sample (Fig. 6.4a,b) was extracted from a Cu/LPSC/Li half cell after depositing 3 mAh cm^{-2} of lithium (~15 microns) at 0.5 mA cm^{-2}. The two images show the Cu/Li/LPSC cross-section at the center and edge of the sample. In each image, the top layer (brighter contrast) is the 10 micron thick copper foil. Below that is the deposited lithium (darkest contrast) and then the LPSC electrolyte (intermediate contrast). The lithium deposits in each image were ~15 microns thick, as expected based on the areal capacity that was plated. Overall, the lithium layer exhibited uniformity in thickness across the interface when plated at this current density (0.5 mA cm^{-2}). The lithium had a smooth and continuous morphology, similar to what was observed by Wang et al. at anode-free

interfaces with LLZO. It is noted that these images only provided a handful of local snapshots of the lithium thickness, and that greater variation may not be captured here.

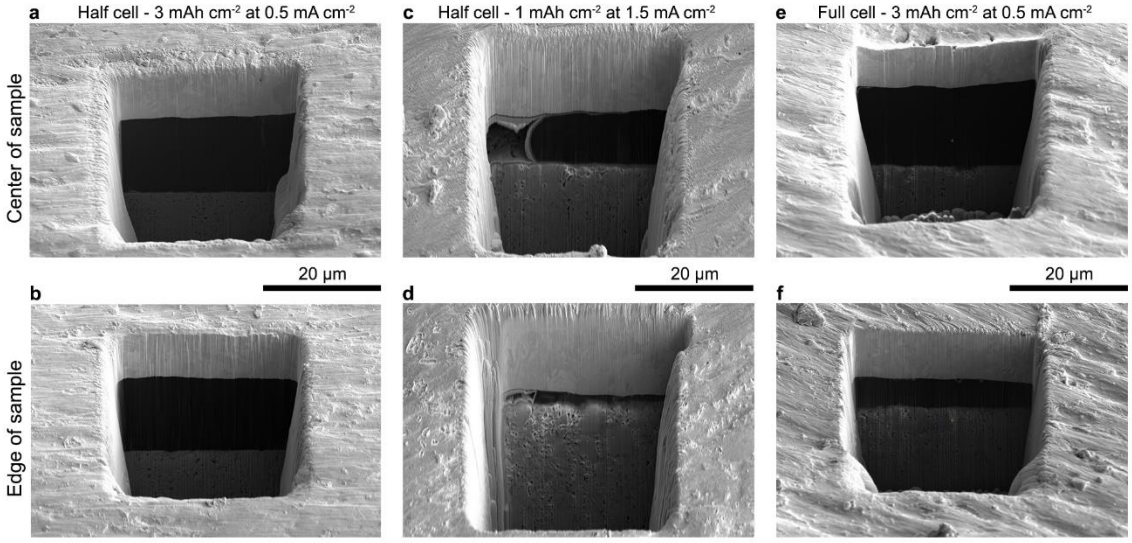

Figure 6.4. SEM images taken after cryo-FIB milling through anode-free Cu/LPSC interfaces after deposition. The top row of images were taken at the center of each sample, while the bottom row of images were taken at the edge. **a,b)** 3 mAh cm^{-2} deposited at 0.5 mA cm^{-2} in a Cu/LPSC/Li half cell. **c,d)** 1 mAh cm^{-2} deposited at 1.5 mA cm^{-2} in a Cu/LPSC/Li half cell. **e,f)** 3 mAh cm^{-2} deposited at 0.5 mA cm^{-2} in a Cu/LPSC/NMC full cell.

The same cryo-FIB/SEM experiment was repeated for a half cell where 1 mAh cm^{-2} was deposited at a high current density of 1.5 mAh cm^{-2}. Two images from the center and edge are shown in Fig. 6.4c,d. This sample exhibited greater variation in deposition thickness from the center to the edge, which was attributed to plating at a higher current density. The region at the center of the sample (Fig. 6.4c) had a lithium thickness of ~11 µm, exceeding the expected 5 µm if deposition was uniform. In contrast, a region at the edge of the sample (Fig. 6.4d) had a lithium thickness of only 2 µm. Based on these results, it is apparent that higher current densities may reduce deposition uniformity. This behavior could explain why significantly less capacity could be plated at 1.5 mA cm^{-2} before

shorting compared to 0.5 mA cm^{-2} (Fig. 6.2). The presence of thicker lithium in the center of the 1.5 mA cm^{-2} sample suggests that there were larger local current densities in that region, which would make it more likely that lithium filaments would form.

The deposition uniformity was also investigated for anode-free full cells. A Cu/LPSC/NMC full cell with a 3 mAh cm^{-2} cathode loading was charged at 0.5 mA cm^{-2} and subsequently characterized using cryo-FIB (Fig. 6.3e,f). An image of a trench cut in the center of the sample revealed a lithium thickness of 17 µm, while an image taken near the sample's edge showed a much smaller lithium thickness of 6 µm. Given these results, the full cell exhibited worse deposition uniformity compared to the half cell despite using the same areal capacity and current density. However, both cells had a similar smooth and continuous lithium morphology. The reasons for the differences in deposition uniformity were not entirely clear. One factor could have been the difference in how the cells were assembled and how pressure was distributed throughout them.

6.3 Impact of Stripping on Cycling Stability

With an improved understanding of plating at anode-free interfaces, the impact of stripping on cell reversibility was investigated next. Figure 6.5a shows that an anode-free half cell cycled at 0.5 mA cm^{-2} with 3 mAh cm^{-2} per half cycle short circuited in the third cycle. The cumulative lithium capacity plated at the Cu/LPSC interface was ~6.5 mAh cm^{-2}, less than the 25 mAh cm^{-2} achieved when plating at 0.5 mA cm^{-2} continuously (Fig. 6.2). The poor reversibility of this cell could be attributed to the large loss of contact, as evidenced by the voltage polarization at the end of stripping. It is important to note that polarization occurred despite a theoretical lithium thickness of ~1.5

μm being left at the interface due to the low Coulombic efficiency of 90%. The loss of contact can thus be associated with interfacial regions that were completely stripped of lithium, while other areas retained lithium metal. A consequence of completely removing lithium in parts of the interface was the need to re-nucleate lithium during the subsequent plating cycle, as shown by the nucleation overpotential in the 2nd and 3rd cycle voltage curves.

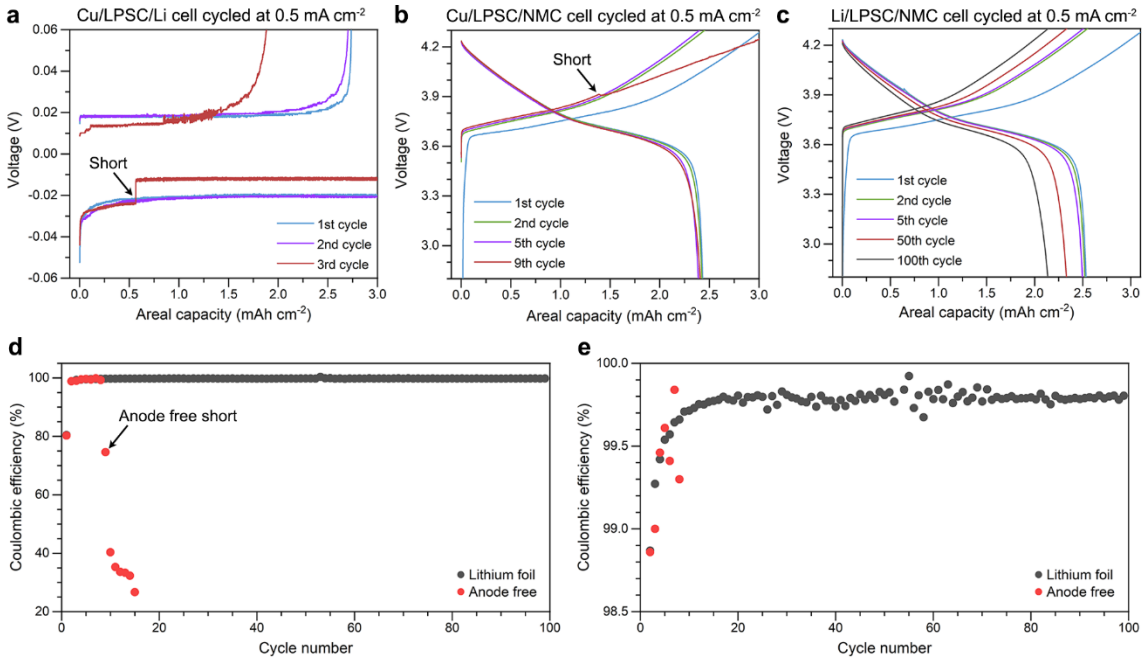

Figure 6.5. a) Cycling a Cu/LPSC/Li half cell at 0.5 mA cm^{-2} with 3 mAh cm^{-2} per half cycle. **b)** Cycling a Cu/LPSC/NMC full cell at 0.5 mA cm^{-2} with a cathode loading of 3 mAh cm^{-2}. **c)** Cycling a Li/LPSC/NMC full cell at 0.5 mA cm^{-2} with a cathode loading of 3 mAh cm^{-2}. This cell used a lithium metal anode with a thickness of ~0.3 mm. **d)** Comparison of the Coulombic efficiencies between the anode free full cell (red circles) and thick Li foil full cell (black circles). **e)** Magnified view of the plot in **(d)**.

Figure 6.5b shows the cycling performance of an anode-free full cell cycled under the same conditions as the half cell. Interestingly, the full cell exhibited a longer cell lifetime by shorting in the 9th cycle instead of the 3rd. Similar to other full cells using

sulfide SSEs, the short circuit was identified based on an abrupt and slight drop in cell voltage during charging, followed by excess capacity beyond the cathode loading. The improvement over the half cell could be partially explained by the 80% initial CE of the full cell, indicating that a thicker theoretical lithium layer of ~2.5 μm was left on the copper foil after the first discharge. The 80% initial CE of this cell was primarily due to the cathode not reincorporating all of the lithium during discharge. This behavior was supported by the fact that a similar initial CE was found for a full cell using thick lithium foil as the anode (Fig. 6.5c). However, the excess lithium left on the copper foil after the first discharge was not able to significantly extend the lifetime of the cell. The temporary improvement in cell lifetime suggested that the buffer effect provided by the excess lithium was eroded over time, likely due to regions of the excess lithium being completed stripped towards the end of the cell's life.

A full cell using a thick lithium metal foil was assembled and tested under the same conditions as the anode-free configurations to better understand the limitations of anode-free interfaces (Fig. 6.5c). Because the areal capacity cycled was much lower than the thickness of the lithium foil, this cell always retained lithium metal at the anode/LPSC interface. This difference greatly impacted cell performance, as the thick lithium foil full cell was able to complete over 100 cycles without short circuiting. Given the evidence of how lithium was stripped in anode-free half and full cells, the key reason for the improved cyclability was likely the retention of lithium metal across the entire interface after stripping, avoiding the catastrophic effects of plating at harshly stripped interfaces.

Despite the poor lifetime of the anode-free full cell compared to the thick lithium foil, it delivered comparable electrochemical performance before shorting. Both cells were

able to access the total cathode loading during the first charge, and exhibited initial CEs of 80%. The Coulombic efficiencies of subsequent cycles in the anode-free cell were also similar to the thick lithium foil cell (Fig. 6.5d,e), with the anode-free cell having an average Coulombic efficiency of 99.3% before shorting compared to 99.4% for the thick lithium foil. The similarity in CE between the two configurations showed that the anode-free architecture developed in this work could achieve relatively efficient cycling, but was limited by its greater propensity towards short circuiting. Additionally, the similar CEs indicated that the cathode was likely the limiting factor for achieving higher CE, instead of the anode.

The nature of harsh lithium stripping at the anode-free interface and subsequent re-nucleation behavior necessitated proper control over stripping to maximize cell performance. To avoid these challenges, the effects of initially depositing a thick lithium layer and stripping a limited percentage of that capacity were explored to prevent complete stripping and voltage polarization. Figure 6.6a shows an anode-free half cell operated at 0.5 mA cm^{-2}, where 3 mAh cm^{-2} was first deposited and then cycled using a half cycle capacity of 1.5 mAh cm^{-2}. The stripping curves exhibited excellent stability without any polarization, indicating that the lithium layer was maintained across the entire copper substrate. No nucleation overpotentials were observed after the initial deposition, further demonstrating the beneficial effects of retaining lithium metal at the interface. Given these improvements, the cell showed a remarkable increase in cell lifetime, with a cumulative lithium capacity of ~114 mAh cm^{-2} being deposited onto copper before a subtle short circuit formed in the 75th cycle (red curve). A similar experiment (Fig. 6.6b,c) was conducted using an anode-free full cell with a cathode loading of 3 mAh cm^{-2} and a limited cycling

capacity of 1 mAh cm^{-2} after the first charge. This cell also showed improved cyclability, lasting over 100 limited cycles without a short circuit forming.

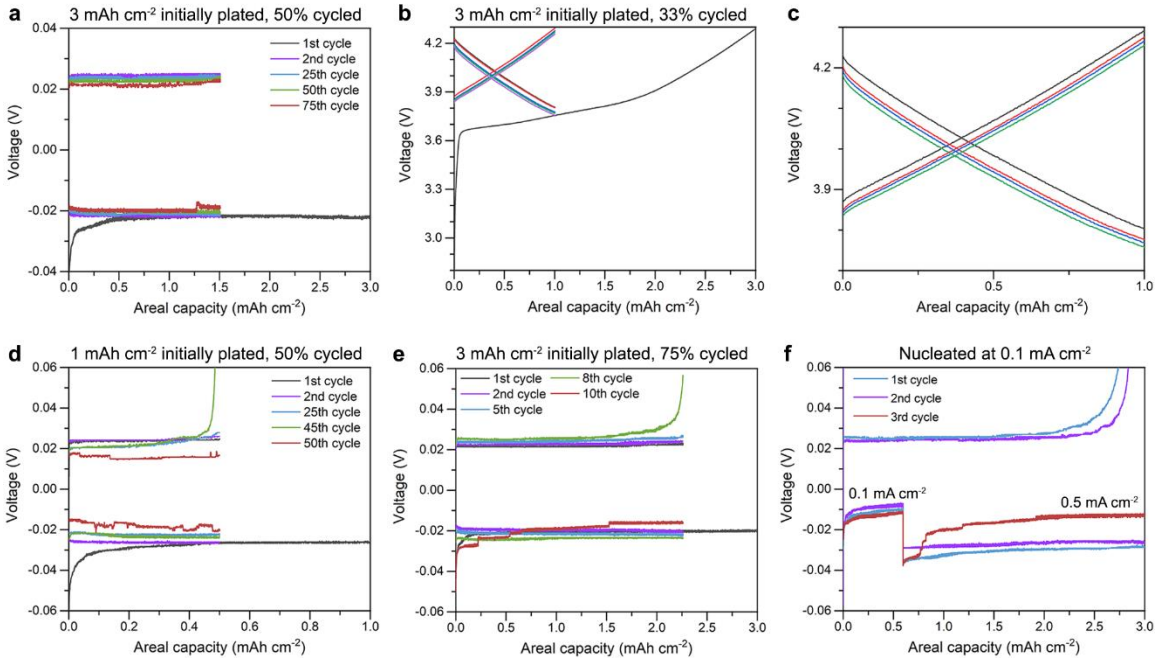

Figure 6.6. a) Limited cycling of a Cu/LPSC/Li half cell at 0.5 mA cm^{-2} with an initial deposition step of 3 mAh cm^{-2} and subsequent half cycles of 1.5 mAh cm^{-2}. **b)** Limited cycling of a Cu/LPSC/NMC full cell with a cathode loading of 3 mAh cm^{-2} at 0.5 mA cm^{-2}. Each half cycle was 1 mAh cm^{-2} after the initial charge. **c)** Magnified view of the limited charge/discharge curves in **(b)**. **d)** Limited cycling of a Cu/LPSC/Li half cell at 0.5 mA cm^{-2} with an initial deposition step of 1 mAh cm^{-2} and subsequent half cycles of 0.5 mAh cm^{-2}. **e)** Limited cycling of a Cu/LPSC/Li half cell at 0.5 mA cm^{-2} with an initial deposition step of 3 mAh cm^{-2} and subsequent half cycles of 2.3 mAh cm^{-2}. **f)** Cycling a Cu/LPSC/Li half cell with a slow nucleation step at 0.1 mA cm^{-2}, followed by plating and stripping at 0.5 mA cm^{-2}.

An important observation during these controlled stripping experiments was that the thickness of the initial deposited lithium layer influenced cell stability. Figure 6.6d shows that a cell with a lower initial deposit capacity of 1 mAh cm^{-2} and cycled capacity of 50% short circuited after plating only ~25 mAh cm^{-2} onto copper. This result was worse

than the cell in Fig. 6.6a that had a thicker initial lithium layer, which plated ~114 mAh cm^{-2} onto copper before shorting. A notable difference was that the cell with the thinner initial lithium layer began to polarize during stripping, as shown in the 45th cycle curve, whereas the cell with the 3 mAh cm^{-2} initial layer had stable stripping in every cycle. After repeated polarization during stripping of the thinner layer, the nucleation overpotential returned. The worse stability of the cell with less initial lithium was likely due to the fact that it had less material to act as a buffer against detrimental stripping. For example, stripping 50% from a 3 mAh cm^{-2} initial layer would leave ~7.5 µm of lithium, whereas stripping 50% from an initial layer of 1 mAh cm^{-2} would leave only ~2.5 µm (assuming a uniform lithium thickness in both cases). Since deposited lithium can be non-uniform, a cell with a thinner lithium layer would be more susceptible to completely losing lithium in some regions during stripping.

These results suggested that harsh stripping followed by re-nucleation of the *in situ* lithium layer is the limiting factor for anode-free cells. Therefore, tailoring the electrochemistry of the cell to promote facile nucleation was hypothesized to be another route to enhance cell lifetime. Based on this idea, a Cu/LPSC/Li cell was ran with a low current density of 0.1 mA cm^{-2} during the nucleation phase, followed by plating at 0.5 mA cm^{-2} until a total half cycle capacity of 3 mAh cm^{-2} was reached. Figure 6.6f shows that despite nucleating at a slow rate, there was no improvement compared to the half cell shown in Fig. 6.5a. These findings suggest that the quality of the initially deposited lithium may not significantly impact subsequent deposition onto that layer.

The development of strategic electrochemical procedures will be critical for making viable anode-free SSBs. While this has shown the benefits of limiting the cycle capacity

after forming the initial lithium layer to prevent catastrophic stripping and re-nucleation, the limitations demonstrated here are too restrictive for commercial batteries. The utilization of the cathode loading must be maximized in order to achieve a high reversible areal capacity and avoid the penalty of having unused, heavy cathode particles that supply the initial lithium. For example, having a cell with a cathode loading / *in situ* Li thickness of 3 mAh cm^{-2} and 100% cycle utilization would have a cell level specific energy of ~285 Wh kg^{-1} in the discharged state. Decreasing the utilization to 50%, as presented in this work, would reduce the specific energy to 141 Wh kg^{-1}. Although the protocols in this work are not viable for a commercial cell, it is envisioned that careful optimization of electrochemical protocols during the end of discharge and beginning of charge could help solve the challenges of anode-free cycling.

New engineering strategies are also needed to mitigate the challenges of harsh stripping and re-nucleation in anode free solid-state batteries. While Samsung's Ag-C layer has demonstrated that interfacial engineering can alleviate these problems, it would be beneficial to find solutions that occupy minimal volume and mass to maximize the advantages in energy density. One approach could be to develop mechanically pliable materials that are better at uniformly distributing pressure at the entire, which could promote more uniform stripping. These pliable materials could be either the SSE or a conducting material that can act as the current collector. Incorporating thin films on the substrate that stabilize deposition behavior could also improve cell lifetime.

6.4 Conclusions

This work demonstrated the feasibility and limitations of plating and stripping lithium metal in anode-free SSBs. An anode-free configuration with a sulfide SSE was assembled using a simple cold pressing step at ~15 MPa. Large amounts of lithium (> 5 mAh cm^{-2}) could be plated onto the copper current collector at a high current density of 1 mA cm^{-2} without short circuiting. However, lithium was found to be preferentially stripped in some regions, causing complete lithium removal and contact loss in those regions. Subsequent plating at poorly stripped interfaces required re-nucleation of lithium metal due to its absence in some regions. This process of non-uniform stripping and re-nucleation greatly accelerated the formation of a short circuit. Despite these limitations, it was shown that anode-free full cells exhibited comparable Coulombic efficiencies to full cells with thick lithium metal foils, suggesting that anode-free interfaces do not hinder capacity retention. Different strategies were explored to mitigate the effects of non-uniform stripping and prevent premature short circuiting.

CHAPTER 7. ENERGY DENSITY ANALYSIS OF ALLOY ANODES IN SOLID-STATE BATTERIES

7.1 Introduction

Research on SSBs has been primarily focused on using lithium metal as the anode material due to its superior capacity and reduction potential. However, the challenges of interfacing lithium metal with SSEs has opened opportunities for other types of anodes to be utilized in SSBs. In particular, materials that alloy with Li have shown promising electrochemical behavior in SSBs. Materials such as silicon, tin, aluminum, and others, can store more Li^+ ions per mass and volume than conventional graphite anodes, and their use in SSBs could enable specific energy and energy density values much higher than conventional Li-ion batteries[26–30,144,163,164].

The challenges of using alloy materials to reliably deliver high capacity with minimal degradation during charge/discharge cycling arise largely because of the chemo-mechanical interactions of these materials with their surroundings within a battery system. Alloy anodes have been well-studied in liquid electrolyte systems, and are known to experience large volumetric changes that can cause severe capacity fade[26]. The all-solid environment in SSBs presents entirely new interfacial interactions and chemo-mechanical behavior compared to conventional liquid environments, which could allow for improved cycling performance of alloy anodes while avoiding deleterious shorting issues when using lithium metal.

In this chapter, alloy anodes in SSBs were evaluated by calculating the energy densities of different battery chemistries at the cell-level. The methodology of these calculations is discussed in a step-by-step procedure to justify the equations used. Energy density plots were created and analyzed to provide numerical context for how alloy anodes could be feasible in commercial SSBs. The mechanistic benefits of using alloy anodes instead of lithium metal in SSBs are discussed, as well as the advantages that alloys in SSBs have over alloys in liquid electrolytes. Together, this analysis and discussion show that alloy anodes offer practical alternatives to high energy density SSBs.

7.2 Mechanistic Advantages of Alloy Anodes in SSBs

A key challenge of using alloy anodes in liquid electrolytes is the relationship between the volumetric changes of particles during cycling and SEI formation[165,166]. Alloy particles experience much larger volume changes than conventional graphite particles. Since the SEI is a film that lies on the surface of these particles, stresses generated during lithiation and delithiation can cause the SEI layer to fracture. This process exposes the underlying active particles to the electrolyte again, opening a pathway for new SEI to form. Continual SEI formation is inherently detrimental because it consumes lithium ions and increases impedance, resulting in greater capacity fade. While SEI is present on graphite anodes, it's formation occurs primarily in the first cycle and exhibits little growth afterwards. Decoupling the mechanics of alloy lithiation/delithiation from SEI growth is therefore an important step towards enabling alloy anodes.

The distinct mechanical properties of SSEs compared to liquid electrolytes could help solve this challenging relationship. For example, SSEs cannot flow and wet the

surfaces of alloy particles, which could reduce SEI formation if the existing SEI becomes cracked. The application of stack pressure and surrounding solid materials could also confine and compress the alloy particles, possibly reducing the detrimental effects of volume change. Additionally, the composition and structure of interphases formed between alloy anodes and SSEs are distinct from liquid electrolytes and may have better electrochemical stability.

While SSBs offer alloy anodes new opportunities outside of liquid electrolytes, alloy anodes conversely offer new opportunities in SSBs beyond lithium metal anodes. As discussed in the Chapter 1, lithium metal can penetrate through SSEs and form a short circuit that kills the cell. While significant progress has been made to mitigate this process, it is unclear whether large format SSBs manufactured at commercial scale will be able to avoid short circuiting with suitable quality control. Alloy anodes are intriguing alternatives to lithium metal anodes in SSBs because they exhibit both high capacity and much greater resistance to short circuiting.

7.3 Energy Density Analysis of Alloy Anodes

The specific energy and energy density of different battery configurations were evaluated using a series of equations with materials properties and cell assumptions as the inputs. It is important to note that these calculations only considered a single stack at the cell-level consisting of the electrodes, electrolyte, and current collectors. The effects of having multiple stacks and the additional mass and volume of hardware at the pack-level were not factored into the analysis. All cells assumed a cathode areal capacity loading of 4 mAh cm^{-2}. Table A.1 lists the assumed N:P ratios, which describe the ratio of the anode

capacity to the cathode capacity and are used to derive the anode areal capacity loading. Two key material properties, the density and specific capacity, are listed in Table A.3 for all materials evaluated.

A volume ratio between the active material and electrolyte was assumed for each electrode evaluated; these ratios are listed in Tables A.1 and A.2. For the solid-state cells evaluated, it was assumed that each component containing SSE used the same type of electrolyte throughout the entire cell. Additionally, only active material and electrolyte were considered in the SSB composite electrodes. Calculations for composite electrodes in liquid cells assumed a composition of 95 wt% active material, 2.5 wt% binder, and 2.5 wt% conductive carbon. The porosity of each composite electrode with liquid electrolyte is listed in Table A.2. A higher porosity was assumed for the alloy anodes due to their greater volume expansion during lithiation.

With the assumed electrode compositions and densities of every component, the composite electrode density could be calculated by summing the material density (ρ_i) multiplied by the material volume fraction (ϕ_i) for each component in the composite.

$$\rho_{composite} = \sum_{i=1}^{N} \rho_i \phi_i \tag{7.1}$$

Given the active material's specific capacity (q_{active}), density (ρ_{active}), and volume fraction (ϕ_{active}), the electrode charge density (Q_{vol}) could be calculated using Eq. 7.2.

$$Q_{vol} = q_{active} \rho_{active} \phi_{active} \tag{7.2}$$

The necessary electrode thickness was then calculated by dividing the assumed areal capacity (Q_{areal}) by the electrode charge density.

$$l_{electrode} = \frac{Q_{areal}}{Q_{vol}} \tag{7.3}$$

The areal mass loading ($m_{electrode}$) of the electrode was calculated by multiplying the electrode thickness by the composite electrode density.

$$m_{electrode} = l_{electrode}\rho_{composite} \tag{7.4}$$

The entire thickness and areal mass loading of a single stack was calculated by summing the values of each individual component in the stack (Eqs. 7.5 and 7.6). Every stack used a 10 μm thick copper current collector and a 10 μm thick aluminum current collector. For Figure 7.1a, the thickness of the electrolyte layer was 20 μm in all cases. In Figure 7.2, the thickness of the electrolyte was intentionally varied to understand it's effect on cell energy. The densities used to calculate the areal mass loadings for the current collectors and electrolyte are listed in Table A.3.

$$l_{stack} = l_{Al} + l_{cathode} + l_{electrolyte} + l_{anode} + l_{Cu} \tag{7.5}$$

$$m_{stack} = m_{Al} + m_{cathode} + m_{electrolyte} + m_{anode} + m_{Cu} \tag{7.6}$$

With the total stack thickness and areal mass loading, the specific energy and energy density were calculated using Eqs. 7.7 and 7.8. The assumed average cell voltages for each configuration are listed in Table A.4, as well as the calculated energy values.

$$Specific\ energy = \frac{q_{cathode} V_{cell}}{m_{stack}} \tag{7.7}$$

$$Energy\ density = \frac{q_{cathode} V_{cell}}{l_{stack}} \tag{7.8}$$

Figure 7.1 shows the theoretical energy density and specific energy values for a variety of different solid-state and liquid-based cell stacks. There are two clusters of values from SSBs with alloy anodes, highlighted in green and blue. These two clusters arise when using two different exemplary SSE materials within the cells; the blue cluster with lower specific energy utilizes the oxide LLZO and the green cluster with higher specific energy utilizes the sulfide LPSC. The lower specific energy of LLZO-based cells in Fig. 7.1 results from the high density of LLZO (5.11 g cm^{-3}), and removing LLZO from the cathode composite would boost specific energy (not shown).

This figure also shows that LPSC-based SSBs have slightly lower specific energy (but similar energy density) compared to equivalent liquid-electrolyte cells; this is again because this SSE has higher density than liquid electrolytes (1.86 g cm^{-3} vs 1.3 g cm^{-3}). These specific energy differences could be minimized by including less SSE in the composite cathode. Overall, it is clear that SSE materials with low density and/or minimizing the use of SSE materials within the electrode structures are key strategies for achieving maximal specific energy. In all cases, however, alloy anode-based SSBs with

LPSC exceed the energy density and specific energy of the graphite-based liquid-electrolyte Li-ion cell included for comparison in Fig. 7.1.

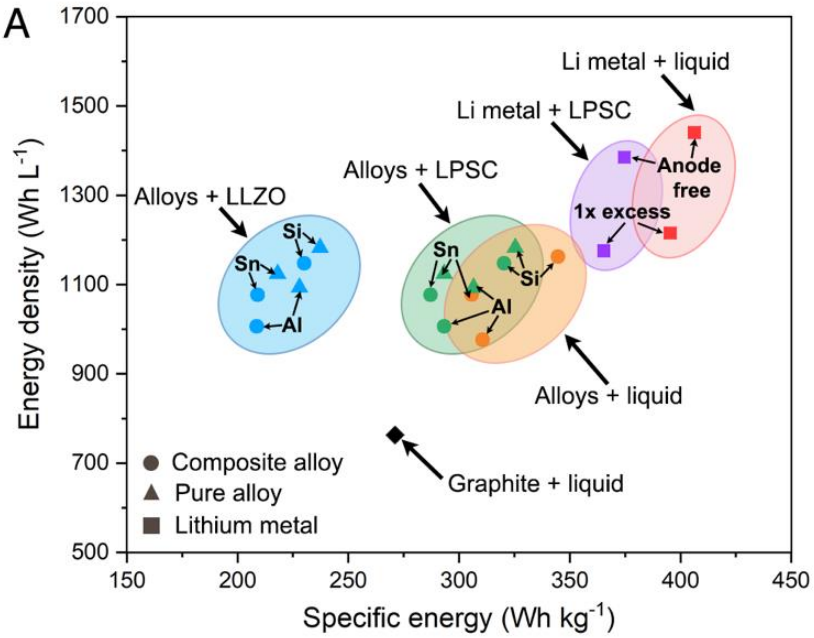

Figure 7.1. Predicted energy density (Wh L^{-1}) and specific energy (Wh kg^{-1}) of solid-state and liquid-based battery stacks with different anodes: graphite, lithium, and alloy materials (silicon, tin, aluminum). For the alloy anodes, circles represent composites with the SSE material included in the electrode, while triangles represent the pure alloy anode material as the electrode. All cells assume pairing with a $LiNi_{0.8}Mn_{0.1}Co_{0.1}O_2$ composite cathode, and the SSB cells assume 40 vol% of the cathode architecture contains SSE material and that the SSE separator is 20 μm thick.

Within the green oval representing LPSC-based SSBs in Fig. 7.1, individual points representing SSBs with aluminum (990 mAh g^{-1}), tin (992 mAh g^{-1}), and silicon (3579 mAh g^{-1}) are shown. The circular data points assume the anode structures include 40 vol % SSE, and the triangular points assume that the anode is made of pure alloy material. While silicon-based anodes result in the highest specific energy and energy density, the differences among cells with various active materials are relatively small despite their large

differences in specific capacity. This is because of the diminishing returns in terms of cell-specific metrics for anode specific capacities greater than ~1000 mAh g^{-1}, since the cells still contain the same amount of cathode material. This trend is expected among other alloys as well. Another conclusion from comparing the values in Fig. 7.1 is that the inclusion of SSE material within an alloy anode composite (circles) does not significantly reduce the energy values compared to a pure anode material (triangles). This is largely because the alloy electrodes are relatively thin compared to the cathode as a result of the higher Li storage capacities of the alloy materials, and thus adding SSE to the anode does not significantly change the overall energy metrics.

Lithium-metal based cells using SSEs and liquid electrolytes exhibit the highest specific energy. The true energy advantage of lithium is achieved in an anode-free configuration, where all lithium is plated on a bare current collector during the first charge. While such a concept is promising, it is challenging to achieve stable cycling with anode-free cells (using either liquid or SSEs) because having zero excess Li^+ inventory requires extremely high Coulombic efficiencies. When 1× excess lithium is used (i.e., a ~20-μm lithium foil is used as the anode), the energy density of the cell is similar to the alloy anode cells, while still surpassing them in specific energy. We note that in all cases for lithium or alloy anodes, these metrics were calculated in the discharged state, and the necessary net volume increase in the cell after charge would result in lower energy density when calculated in the charged state.

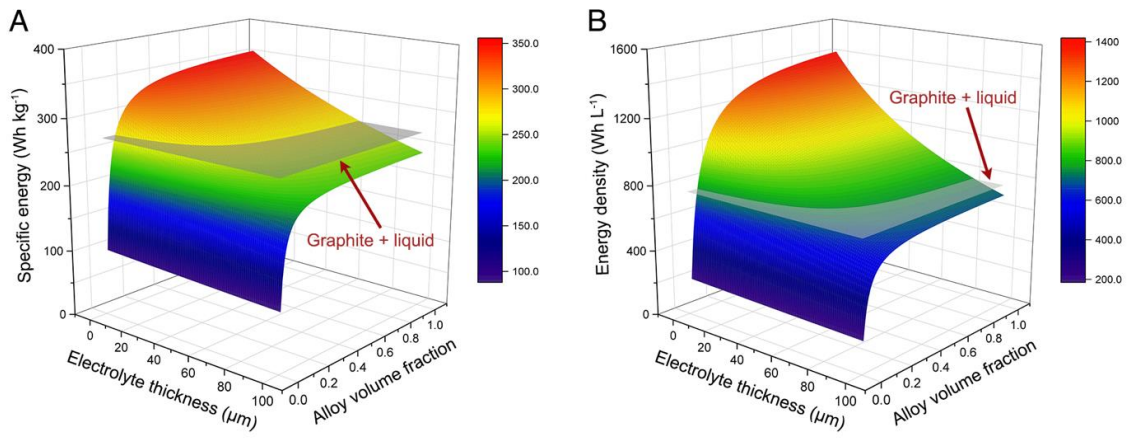

Figure 7.2. (a) Specific energy (Wh kg^{-1}) and **(b)** energy density (Wh L^{-1}) for a SSB stack as a function of the electrolyte separator thickness and the volume fraction of active material in the anode. The battery consisted of silicon active anode material, LPSC SSE in the anode, cathode, and separator, and NMC-811 active cathode material with 60 vol% active material loading in the cathode.

The effects of the SSE thickness and volume fraction of active material in the alloy anode on specific energy and energy density are represented by the surface plots shown in Fig. 7.2. This analysis was only performed on a cell stack using LPSC as the SSE and silicon as the active material. As a reference, the values calculated for a conventional graphite + liquid cell are represented by the grey planes. These plots therefore visualize what combinations of electrolyte thickness and alloy volume fraction store more energy than a conventional battery. In general, a thin SSE separator of ~20 μm is necessary to greatly surpass conventional battery chemistry. However, alloy volume fraction can have a much greater effect, as there is a dramatic drop in specific energy and energy density when using volume fractions below 0.2. Fortunately, successful SSB cycling has been demonstrated at active material fractions around 0.5. Increasing the fraction of active material in the composite will continue to yield meaningful boosts in energy density, albeit not as much as the transition away from low fractions. Overall, these surface plots show

that there are a number of viable combinations of SSE thickness and alloy composition that could surpass the energy density of conventional lithium-ion batteries.

7.4 Conclusions

Alloy materials are attractive candidates as anodes in lithium-ion batteries due to their high capacity. Although commercial batteries have successfully incorporated small amounts of alloys to boost energy density, and other companies are seeking to transition to full alloy anodes, the detrimental behavior of lithiating and delithiating alloys has limited the cell lifetime when using liquid electrolytes. This chapter has analyzed the potential benefits of pairing alloy anodes with SSEs, from both qualitative and quantitative perspectives. The mechanical and chemical properties of SSEs provide an opportunity to mitigate the chemo-mechanical phenomena in alloy anodes that cause capacity fade. Furthermore, alloy anodes in SSBs could greatly reduce the chances of cell failure due to short circuiting. Energy density calculations showed that SSBs with alloy anodes can significantly exceed conventional batteries, while also remaining competitive with next-generation materials like lithium metal anodes.

CHAPTER 8. CONCLUSIONS AND FUTURE WORK

Great strides have been made by the SSB community over the past 5 years to better understand how electrodes and SSEs should be interfaced to build high performance batteries. Before 2017, the presence of detrimental interfacial phenomena in SSBs had been identified, but little was known about the underlying mechanisms that governed them. This dissertation has made important contributions to the cumulative understanding of how these interfacial processes occur and impact SSB performance.

Chapters 3 and 4 showed that poor interphases at electrode/SSE interface must avoided for any practical SSB, further informing the design constraints that must be considered when selecting materials. Chapter 4 also demonstrated how the loss of contact at the interface can cause cell failure, emphasizing that the spatial distribution of contact can be as important as the amount of contact area due to current constriction effects. New insights into the relationship between electrochemical testing parameters and lithium filament penetration were gained in Chapters 5, which showed that lithium filaments can be formed even at low current densities in sulfide SSEs. The impact that areal capacity has on the stability of plating and stripping lithium metal in SSBs was also demonstrated. The performance of anode-free SSBs using a relatively simple assembly was investigated in Chapter 6, revealing that while large amounts of lithium can be deposited at relatively high rates, the cyclability of these cells is severely limited by non-uniform stripping. Although this dissertation was focused primarily on studying phenomena at Li/SSE interfaces, Chapter 7 provided motivation and analysis to justify the opportunities of using alloy anodes in SSBs.

While there are still outstanding questions about interfacial dynamics that must be answered, SSBs have started to enter a new era of development focused on advancing the processing capabilities to manufacture these devices at scale. A major limitation of lab-scale research on SSBs has been the dimensions of the cells, which typically use thick SSEs (~0.5-1 mm), unrealistic electrode thicknesses, and relatively small areas (< 1 cm^2). Commercial SSBs require thin SSEs on the order of ~20 µm with much larger total areas. Lithium metal SSBs must also either utilize no excess lithium (anode-free), or be manufactured with lithium foils that are substantially thinner than what is typically used in a lab (~10-25 µm vs 100-500 µm). Significant work is thus needed to transition lab-scale research into a dimensional regime that is comparable to the demands of commercial SSBs. Efforts have already been underway[167–169], but the commercialization of SSBs would benefit tremendously from a widespread adoption of more practical components in lab-scale research.

Another problem that must be solved to build viable SSBs is achieving excellent cycling performance at stack pressures that are a few MPa or less[98,99]. High stack pressure has long been used as a crutch for many studies to successfully cycle SSBs[51,170–173], as higher pressures make it easier to establish intimate interfacial contact between the SSE and electrodes. This includes operating at pressures greater than 100 MPa, approximately equivalent to the pressure at the bottom of the Mariana Trench. Such high stack pressures are not feasible for commercial devices, as the hardware required would greatly diminish the pack-level energy density. This fact is also likely true for the stack pressures used in parts of this dissertation (~15 MPa), despite these values only being moderate in the context of lab-scale SSB research. Future studies on SSBs should thus emphasize the investigation

of performance and mechanisms when operating at stack pressures less than 5 MPa. Finding strategies to develop stable interfaces at low pressures is critical to the development of practical SSBs, but will be difficult due to the nature of stripping at lithium metal interfaces and ion transport in composite cathodes.

Beyond striving to meet the demands of commercial SSBs, it will be important to continue to invest in research on novel anode, cathode, and SSE materials. Anodes could benefit from further exploration into materials besides lithium metal. Recent work has shown that can silicon anodes in SSBs can be cycled with impressive performance[173], albeit at very large stack pressures. On the cathode side, these materials have been hindered by the need to incorporate SSE particles in the cathode to increase ionic conductivity. Emphasis should be placed on developing new forms of cathodes that can operate with zero added SSE, whether it be through novel chemistries or innovative structures of existing chemistries. Lastly, the development of novel SSEs should not be neglected. While many promising materials have been made, there is still no reported SSE that exhibits all of the following: high conductivity, excellent electrochemical stability, ability to easily conform to interfaces, and simple processing at scale.

APPENDIX

A.1 Tables for energy density calculations in Chapter 7

Table A.1. Composition and areal capacity for each SSB electrode evaluated.

Composition (vol%)	**Areal capacity (mAh cm^{-2})**
60% $LiNi_{0.8}Mn_{0.1}Co_{0.1}O_2$, 40% LPSC	4
60% $LiNi_{0.8}Mn_{0.1}Co_{0.1}O_2$, 40% LLZO	4
60% Si, 40% LPSC	4.4
60% Al, 40% LPSC	4.4
60% Sn, 40% LPSC	4.4
60% Si, 40% LLZO	4.4
60% Al, 40% LLZO	4.4
60% Sn, 40% LLZO	4.4
100% Si	4.4
100% Al	4.4
100% Sn	4.4
1x excess Li (solid)	4
Anode-free Li (solid)	0 (*in discharged state)

Table A.2. Composition, areal capacity, and porosity for each liquid electrode evaluated.

Composition (wt%)	**Areal capacity (mAh cm^{-2})**	**Porosity (%)**
95% $LiNi_{0.8}Mn_{0.1}Co_{0.1}O_2$ 2.5% binder 2.5% conductive additive	4	30
95% graphite 2.5% binder 2.5% conductive additive	4.4	30
95% silicon 2.5% binder 2.5% conductive additive	4.4	50
95% aluminum 2.5% binder 2.5% conductive additive	4.4	50
95% tin 2.5% binder 2.5% conductive additive	4.4	50
1x excess Li (liquid)	4	-
Anode-free Li (liquid)	0 (*in discharged state)	-

Table A.3. List of the densities and specific capacities used.

Material	**Density (g cm^{-3})**	**Specific capacity (mAh g^{-1})**
Li_6PS_5Cl (LPSC)	1.86	-
$Li_7La_3Zr_2O_{12}$ (LLZO)	5.1	-
$LiNi_{0.8}Mn_{0.1}Co_{0.1}O_2$ (NMC)	4.78	200
Silicon	2.33	3579
Aluminum	2.7	990
Tin	5.75	992
Lithium	0.53	3861
Graphite	2.2	372
Binder	1.8	-
Conductive carbon	0.16	-
Liquid electrolyte	1.3	-
Aluminum	2.7	-
Copper	8.96	-

Table A.4. Average voltage, specific energy, and energy density for each configuration.

	Average voltage (V)	**Specific energy (Wh kg^{-1})**	**Energy density (Wh L^{-1})**
Sulfides			
Li (1x excess)/LPSC/NMC	3.8	365	1176
Li (anodeless)/LPSC/NMC	3.8	375	1385
60% Si/LPSC/NMC	3.4	320	1147
60 % Al/LPSC/NMC	3.45	293	1006
60% Sn/LPSC/NMC	3.3	287	1077
100% Si/LPSC/NMC	3.4	325	1182
100% Al/LPSC/NMC	3.45	307	1094
100% Sn/LPSC/NMC	3.3	293	1124
Oxides			
60% Si/LLZO/NMC	3.4	230	1147
60% Al/LLZO/NMC	3.45	209	1006
60% Sn/LLZO/NMC	3.3	209	1077
100% Si/LLZO/NMC	3.4	237	1182
100% Al/LLZO/NMC	3.45	228	1094
100% Sn/LLZO/NMC	3.3	218	1124
Liquid			
Graphite/Liquid/NMC	3.7	279	784
Si/Liquid/NMC	3.4	345	1162
Al/Liquid/NMC	3.45	311	977
Sn/Liquid/NMC	3.3	306	1078
Li (1x excess)/Liquid/NMC	3.8	395	1215
Li (anodeless)/Liquid/NMC	3.8	406	1440

REFERENCES

1. Fischer, M., Werber, M. & Schwartz, P. V. Batteries: Higher energy density than gasoline? *Energy Policy* **37**, 2639–2641 (2009).

2. Harlow, J. E. *et al.* A wide range of testing results on an excellent lithium-ion cell chemistry to be used as benchmarks for new battery technologies. *J. Electrochem. Soc.* **166**, A3031 (2019).

3. Dubal, D. P., Ayyad, O., Ruiz, V. & Gómez-Romero, P. Hybrid energy storage: The merging of battery and supercapacitor chemistries. *Chem. Soc. Rev.* **44**, 1777–1790 (2015).

4. Energy storage grand challenge: Energy storage market report. *U.S. Department of Energy* (2020).

5. Goodenough, J. B. & Park, K. S. The Li-ion rechargeable battery: A perspective. *J. Am. Chem. Soc.* **135**, 1167–1176 (2013).

6. Goodenough, J. B. How we made the Li-ion rechargeable battery. *Nat. Electron.* **1**, 204 (2018).

7. Albertus, P., Babinec, S., Litzelman, S. & Newman, A. Status and challenges in enabling the lithium metal electrode for high-energy and low-cost rechargeable batteries. *Nat. Energy* **3**, 16–21 (2018).

8. Betz, J. *et al.* Theoretical versus practical energy: A plea for more transparency in the energy calculation of different rechargeable battery systems. *Adv. Energy Mater.* **9**, 1803170 (2019).

9. Radin, M. D. *et al.* Narrowing the gap between theoretical and practical capacities in Li-ion layered oxide cathode materials. *Adv. Energy Mater.* **7**, 1602888 (2017).

10. Cao, Y., Li, M., Lu, J., Liu, J. & Amine, K. Bridging the academic and industrial metrics for next-generation practical batteries. *Nat. Nanotechnol.* **14**, 200–207 (2019).

11. Xiao, J. *et al.* Understanding and applying coulombic efficiency in lithium metal batteries. *Nat. Energy* **5**, 561–568 (2020).

12. Li, J., Fleetwood, J., Hawley, W. B. & Kays, W. From materials to cell: State-of-the-art and prospective technologies for lithium-ion battery electrode processing. *Chem. Rev.* **122**, 903–956 (2022).

13. Logan, E. R. & Dahn, J. R. Electrolyte design for fast-charging Li-ion batteries. *Trends Chem.* **2**, 354–366 (2020).

14. Winter, M., Barnett, B. & Xu, K. Before Li ion batteries. *Chem. Rev.* **118**, 11433–11456 (2018).

15. Asenbauer, J. *et al.* The success story of graphite as a lithium-ion anode material-fundamentals, remaining challenges, and recent developments including silicon (oxide) composites. *Sustain. Energy Fuels* **4**, 5387–5416 (2020).

16. Mizushima, K., Jones, P. C., Wiseman, P. J., & Goodenough, J. B. Li_xCoO_2 ($0 < x < 1$): A new cathode material for batteries of high energy density. *Mater. Res. Bull.* **15**, 783-789 (1980).

17. Wang, K. *et al.* Recent advances and historical developments of high voltage lithium cobalt oxide materials for rechargeable Li-ion batteries. *J. Power Sources* **460**, 228062 (2020).

18. Wang, L., Chen, B., Ma, J., Cui, G. & Chen, L. Reviving lithium cobalt oxide-based lithium secondary batteries-toward a higher energy density. *Chem. Soc. Rev.* **47**, 6505–6602 (2018).

19. Deberdt, R. & Le Billon, P. Conflict minerals and battery materials supply chains: A mapping review of responsible sourcing initiatives. *Extr. Ind. Soc.* **8**, 100935 (2021).

20. Haregewoin, A. M., Wotango, A. S. & Hwang, B. J. Electrolyte additives for lithium ion battery electrodes: Progress and perspectives. *Energy Environ. Sci.* **9**, 1955–1988 (2016).

21. Manthiram, A. A reflection on lithium-ion battery cathode chemistry. *Nat. Comm.* **11**, 1550 (2020).

22. Blomgren, G. E. The development and future of lithium ion batteries. *J. Electrochem. Soc.* **164**, A5019 (2017).

23. Jung, R., Metzger, M., Maglia, F., Stinner, C. & Gasteiger, H. A. Oxygen release and its effect on the cycling stability of $LiNi_xMn_yCo_zO_2$ (NMC) cathode materials for Li-ion batteries. *J. Electrochem. Soc.* **164**, A1361 (2017).

24. Yang, X. G., Liu, T. & Wang, C. Y. Thermally modulated lithium iron phosphate batteries for mass-market electric vehicles. *Nat. Energy* **6**, 176–185 (2021).

25. Zhao, M., Li, B. Q., Zhang, X. Q., Huang, J. Q. & Zhang, Q. A perspective toward practical lithium-sulfur batteries. *ACS Cent. Sci.* **6**, 1095–1104 (2020).

26. McDowell, M. T., Lee, S. W., Nix, W. D. & Cui, Y. 25th anniversary article: Understanding the lithiation of silicon and other alloying anodes for lithium-ion batteries. *Adv. Mater.* **25**, 4966–4985 (2013).

27. Wu, H. *et al.* Stable cycling of double-walled silicon nanotube battery anodes through solid-electrolyte interphase control. *Nat. Nanotechnol.* **7**, 310–315 (2012).

28. Zhang, W. J. A review of the electrochemical performance of alloy anodes for lithium-ion batteries. *J. Power Sources* **196**, 13–24 (2011).

29. Zhang, W. J. Lithium insertion/extraction mechanism in alloy anodes for lithium-ion batteries. *J. Power Sources* **196**, 877–885 (2011).

30. Liu, N. *et al.* A yolk-shell design for stabilized and scalable Li-ion battery alloy anodes. *Nano Lett.* **12**, 3315–3321 (2012).

31. Chae, S., Choi, S. H., Kim, N., Sung, J. & Cho, J. Integration of graphite and silicon anodes for the commercialization of high-energy lithium-ion batteries. *Angew. Chem. Int. Ed.* **59**, 110–135 (2020).

32. Lin, D., Liu, Y. & Cui, Y. Reviving the lithium metal anode for high-energy batteries. *Nat. Nanotechnol.* **12**, 194–206 (2017).

33. Cheng, X. B., Zhang, R., Zhao, C. Z. & Zhang, Q. Toward safe lithium metal anode in rechargeable batteries: A review. *Chem. Rev.* **117**, 10403–10473 (2017).

34. Choi, J. & Kim, P. J. A roadmap of battery separator development: Past and future. *Curren. Opin. Electrochem.* **31**, 100858 (2022).

35. Wood, K. N., Noked, M. & Dasgupta, N. P. Lithium metal anodes: Toward an improved understanding of coupled morphological, electrochemical, and mechanical behavior. *ACS Energy Lett.* **2**, 664–672 (2017).

36. Wood, K. N. *et al.* Dendrites and pits: Untangling the complex behavior of lithium metal anodes through operando video microscopy. *ACS Cent. Sci.* **2**, 790–801 (2016).

37. Chen, K. H. *et al.* Dead lithium: Mass transport effects on voltage, capacity, and failure of lithium metal anodes. *J. Mater. Chem. A* **5**, 11671–11681 (2017).

38. Hobold, G. M. *et al.* Moving beyond 99.9% Coulombic efficiency for lithium anodes in liquid electrolytes. *Nat. Energy* **6**, 951–960 (2021).

39. Liu, H. *et al.* Plating/stripping behavior of actual lithium metal anode. *Adv. Energy Mater.* **9**, 1902254 (2019).

40. Fang, C. *et al.* Quantifying inactive lithium in lithium metal batteries. *Nature* **572**, 511–515 (2019).

41. Janek, J. & Zeier, W. G. A solid future for battery development. *Nat. Energy* **1**, 16141 (2016).

42. Manthiram, A., Yu, X. & Wang, S. Lithium battery chemistries enabled by solid-state electrolytes. *Nat. Rev. Mater.* **2**, 16103 (2017).

43. Famprikis, T., Canepa, P., Dawson, J. A., Islam, M. S. & Masquelier, C. Fundamentals of inorganic solid state electrolytes for batteries. *Nat. Mater.* **18**, 1278-1291 (2019).

44. Kasemchainan, J. *et al.* Critical stripping current leads to dendrite formation on plating in 3 lithium anode solid electrolyte cells. *Nat. Mater.* **18**, 1105-1111 (2019).

45. Krauskopf, T., Hartmann, H., Zeier, W. G. & Janek, J. Toward a fundamental understanding of the lithium metal anode in solid-state batteries - An electrochemo-mechanical study on the garnet-type solid electrolyte $Li_{6.25}Al_{0.25}La_3Zr_2O_{12}$. *ACS Appl. Mater. Interfaces* **11**, 14463–14477 (2019).

46. Wang, M. J., Choudhury, R. & Sakamoto, J. Characterizing the Li-solid-electrolyte interface dynamics as a function of stack pressure and current density. *Joule* **3**, 2165-2178 (2019)

47. Doux, J. M. *et al.* Stack pressure considerations for room-temperature all-solid-state lithium metal batteries. *Adv. Energy Mater.* **10**, 1903253 (2020).

48. Hänsel, C. & Kundu, D. The stack pressure dilemma in sulfide electrolyte based li metal solid-state batteries: a case study with Li_6PS_5Cl solid electrolyte. *Adv. Mater. Interfaces* **8**, 2100206 (2021).

49. Lee, C. *et al.* Stack pressure measurements to probe the evolution of the lithium-solid-state electrolyte interface. *ACS Energy Lett.* **6**, 3261–3269 (2021).

50. Zhang, W. *et al.* (Electro)chemical expansion during cycling: Monitoring the pressure changes in operating solid-state lithium batteries. *J. Mater. Chem. A* **5**, 9929–9936 (2017).

51. Koerver, R. *et al.* Chemo-mechanical expansion of lithium electrode materials-on the route to mechanically optimized all-solid-state batteries. *Energy Environ. Sci.* **11**, 2142–2158 (2018).

52. Krauskopf, T., Richter, F. H., Zeier, W. G. & Janek, J. Physicochemical concepts of the lithium metal anode in solid-state batteries. *Chem. Rev.* **120**, 7745-7794 (2020).

53. Xia, S., Wu, X., Zhang, Z., Cui, Y. & Liu, W. Practical challenges and future perspectives of all-solid-state lithium-metal batteries. *Chem* **5**, 753–785 (2019).

54. Liu, K., Liu, Y., Lin, D., Pei, A. & Cui, Y. Materials for lithium-ion battery safety. *Sci. Adv.* **4**, eaas9820 (2018).

55. Zhang, Z. *et al.* New horizons for inorganic solid state ion conductors. *Energy & Environ. Sci.* **11**, 1945-1976 (2018).

56. Murugan, R., Thangadurai, V. & Weppner, W. Fast lithium ion conduction in garnet-type $Li_7La_3Zr_2O_{12}$. *Angew. Chem. Int. Ed.* **46**, 7778–7781 (2007).

57. Yamane, H. *et al.* Crystal structure of a superionic conductor, $Li_7P_3S_{11}$. *Solid State Ion.* **178**, 1163–1167 (2007).

58. Kamaya, N. *et al.* A lithium superionic conductor. *Nat. Mater.* **10**, 682–686 (2011).

59. Deiseroth, H. J. *et al.* Li_6PS_5X: A class of crystalline Li-rich solids with an unusually high Li^+ mobility. *Angew. Chem. Int. Ed.* **47**, 755–758 (2008).

60. Aono, H., Eisuke, S., Sakdaoka, Y., Imanaka, N. & Adachi, G. Electrical properties and sinterability for lithium germanium phosphate $Li_{1+x}M_xGe_{2-x}(PO_4)_3$, M = Al, Cr, Ga, Fe, Sc, and In systems. *Bull. Chem. Soc. Jpn.* **65** 2200–2204 (1992).

61. Mindemark, J., Lacey, M. J., Bowden, T. & Brandell, D. Beyond PEO—Alternative host materials for Li+-conducting solid polymer electrolytes. *Prog. Polym. Sci.* **81**, 114–143 (2018).

62. Zhou, Q., Ma, J., Dong, S., Li, X. & Cui, G. Intermolecular chemistry in solid polymer electrolytes for high-energy-density lithium batteries. *Adv. Mater.* **31**, 1902029 (2019).

63. Gorecki, W., Jeannin, M., Belorizky, E., Roux, C., & Armand, M. Physical properties of solid polymer electrolyte PEO(LiTFSI). *J. Phys. Cond. Mater.* **7**, 6823 (1995).

64. Lee, M. J. *et al.* Elastomeric electrolytes for high-energy solid-state lithium batteries. *Nature* **601**, 217–222 (2022).

65. Banerjee, A., Wang, X., Fang, C., Wu, E. A. & Meng, Y. S. Interfaces and interphases in all-solid-state batteries with inorganic solid electrolytes. *Chem. Rev.* **120**, 6878–6933 (2020).

66. Tan, D. H. S., Banerjee, A., Chen, Z. & Meng, Y. S. From nanoscale interface characterization to sustainable energy storage using all-solid-state batteries. *Nat. Nanotechnol.* **15**, 170-180 (2020).

67. Lewis, J. A., Tippens, J., Cortes, F. J. Q. & McDowell, M. T. Chemo-mechanical challenges in solid-state batteries. *Trends Chem.* **1**, 845–857 (2019).

68. Nolan, A. M., Zhu, Y., He, X., Bai, Q. & Mo, Y. Computation-accelerated design of materials and interfaces for all-solid-state lithium-ion batteries. *Joule* **2**, 2016-2046 (2018).

69. Mo, Y., Ong, S. P. & Ceder, G. First principles study of the $Li_{10}GeP_2S_{12}$ lithium super ionic conductor material. *Chem. Mater.* **24**, 15–17 (2012).

70. Richards, W. D., Miara, L. J., Wang, Y., Kim, J. C. & Ceder, G. Interface stability in solid-state batteries. *Chem. Mater.* **28**, 266–273 (2016).

71. Xiao, Y. *et al.* Understanding interface stability in solid-state batteries. *Nat. Rev. Mater.* **5**, 105–126 (2020).

72. Ong, S. P. *et al.* Phase stability, electrochemical stability and ionic conductivity of the $Li_{10\pm1}MP_2X_{12}$ (M = Ge, Si, Sn, Al or P, and X = O, S or Se) family of superionic conductors. *Energy Environ.l Sci.* **6**, 148–156 (2013).

73. Tian, Y. *et al.* Compatibility issues between electrodes and electrolytes in solid-state batteries. *Energy Environ. Sci.* **10**, 1150–1166 (2017).

74. Wang, Z. *et al.* In situ STEM-EELS observation of nanoscale interfacial phenomena in all-solid-state batteries. *Nano Lett.* **16**, 3760–3767 (2016).

75. Wu, E. A. *et al.* New insights into the interphase between the na metal anode and sulfide solid-state electrolytes: A joint experimental and computational study. *ACS Appl. Mater. Interfaces* **10**, 10076–10086 (2018).

76. Banerjee, A. *et al.* Revealing nanoscale solid-solid interfacial phenomena for long-life and high-energy all-solid-state batteries. *ACS Appl. Mater. Interfaces* **11**, 43138–43145 (2019).

77. Lewis, J. A. *et al.* Interphase morphology between a solid-state electrolyte and lithium controls cell failure. *ACS Energy Lett.* **4**, 591–599 (2019).

78. Ma, C. *et al.* Interfacial stability of Li metal-solid electrolyte elucidated via in situ electron microscopy. *Nano Letters* **16**, 7030–7036 (2016).

79. Zhu, Y., He, X. & Mo, Y. First principles study on electrochemical and chemical stability of solid electrolyte-electrode interfaces in all-solid-state Li-ion batteries. *J. Mater. Chem. A* **4**, 3253–3266 (2016).

80. Zhu, Y., He, X. & Mo, Y. Origin of outstanding stability in the lithium solid electrolyte materials: insights from thermodynamic analyses based on first-principles calculations. *ACS Appl. Mater. Interfaces* **7**, 23685–23693 (2015).

81. Han, F., Zhu, Y., He, X., Mo, Y. & Wang, C. Electrochemical stability of $Li_{10}GeP_2S_{12}$ and $Li_7La_3Zr_2O_{12}$ solid electrolytes. *Adv. Energy Mater.* **6**, 1501590 (2016).

82. Culver, S. P., Koerver, R., Zeier, W. G. & Janek, J. On the functionality of coatings for cathode active materials in thiophosphate-based all-solid-state batteries. *Adv. Energy Mater.* **9**, 1900626 (2019).

83. Koerver, R. *et al.* Redox-active cathode interphases in solid-state batteries. *J. Mater. Chem. A* **5**, 22750–22760 (2017).

84. Walther, F. *et al.* Visualization of the interfacial decomposition of composite cathodes in argyrodite-based all-solid-state batteries using time-of-flight secondary-ion mass spectrometry. *Chem. Mater.* **31**, 3745-3755 (2019).

85. Koerver, R. *et al.* Capacity fade in solid-state batteries: interphase formation and chemomechanical processes in nickel-rich layered oxide cathodes and lithium thiophosphate solid electrolytes. *Chem. Mater.* **29**, 5574–5582 (2017).

86. Tippens, J. *et al.* Visualizing chemomechanical degradation of a solid-state battery electrolyte. *ACS Energy Lett.* **4**, 1475–1483 (2019).

87. Wenzel, S., Leichtweiss, T., Krüger, D., Sann, J. & Janek, J. Interphase formation on lithium solid electrolytes - An in situ approach to study interfacial reactions by photoelectron spectroscopy. *Solid State Ion.* **278**, 98–105 (2015).

88. Wenzel, S., Sedlmaier, S. J., Dietrich, C., Zeier, W. G. & Janek, J. Interfacial reactivity and interphase growth of argyrodite solid electrolytes at lithium metal electrodes. *Solid State Ion.* **318**, 102–112 (2018).

89. Wenzel, S. *et al.* Interphase formation and degradation of charge transfer kinetics between a lithium metal anode and highly crystalline $Li_7P_3S_{11}$ solid electrolyte. *Solid State Ion.* **286**, 24–33 (2016).

90. Wenzel, S. *et al.* Direct observation of the interfacial instability of the fast ionic conductor $Li_{10}GeP_2S_{12}$ at the lithium metal anode. *Chem. Mater.* **28**, 2400–2407 (2016).

91. Hartmann, P. *et al.* Degradation of NASICON-type materials in contact with lithium metal: SEI formation on solid electrolytes. *J. Phys. Chem. C* **117**, 21064–21074 (2013).

92. Simon, F. J., Hanauer, M., Richter, F. H. & Janek, J. Interphase formation of PEO20:LiTFSI-Li_6PS_5Cl composite electrolytes with lithium metal. *ACS Appl. Mater. Interfaces* **12**, 11713-11723 (2020).

93. Schwöbel, A., Hausbrand, R. & Jaegermann, W. Interface reactions between LiPON and lithium studied by in-situ X-ray photoemission. *Solid State Ion.* **273**, 51–54 (2015).

94. Auvergniot, J. *et al.* Redox activity of argyrodite Li_6PS_5Cl electrolyte in all-solid-state Li-ion battery: An XPS study. *Solid State Ion.* **300**, 78–85 (2017).

95. Han, X. *et al.* Negating interfacial impedance in garnet-based solid-state Li metal batteries. *Nat. Mater.* **16**, 572-579 (2017).

96. Lewis, J. A. *et al.* Linking void and interphase evolution to electrochemistry in solid-state batteries using operando X-ray tomography. *Nat. Mater.* **20**, 503–510 (2021).

97. Greenwood, J. A. Constriction resistance and the real area of contact. *Br. J. Appl. Phys.* **17**, 1621 (1966).

98. Wang, M. J., Kazyak, E., Dasgupta, N. P. & Sakamoto, J. Transitioning solid-state batteries from lab to market: Linking electro-chemo-mechanics with practical considerations. *Joule* **5**, 1371–1390 (2021).

99. Doerrer, C. *et al.* High energy density single-crystal NMC/Li_6PS_5Cl cathodes for all-solid-state lithium-metal batteries. *ACS Appl. Mater. Interfaces* **13**, 37809-37815 (2021).

100. Gao, X. *et al.* Solid-state lithium battery cathodes operating at low pressures. *Joule* **6**, 636–646 (2022).

101. Cheng, E. J., Sharafi, A. & Sakamoto, J. Intergranular Li metal propagation through polycrystalline $Li_{6.25}Al_{0.25}La_3Zr_2O_{12}$ ceramic electrolyte. *Electrochim. Acta* **223**, 85–91 (2017).

102. Ren, Y., Shen, Y., Lin, Y. & Nan, C. W. Direct observation of lithium dendrites inside garnet-type lithium-ion solid electrolyte. *Electrochem. Comm.* **57**, 27–30 (2015).

103. Nagao, M. *et al.* In situ SEM study of a lithium deposition and dissolution mechanism in a bulk-type solid-state cell with a Li_2S-P_2S_5 solid electrolyte. *Phys. Chem. Chem. Phys.* **15**, 18600–18606 (2013).

104. Rosso, M. *et al.* Dendrite short-circuit and fuse effect on Li/polymer/Li cells. *Electrochim. Acta* **51**, 5334–5340 (2006).

105. Porz, L. *et al.* Mechanism of lithium metal penetration through inorganic solid electrolytes. *Adv. Energy Mater.* **7**, 1701003 (2017).

106. Aguesse, F. *et al.* Investigating the dendritic growth during full cell cycling of garnet electrolyte in direct contact with Li metal. *ACS Appl. Mater. Interfaces* **9**, 3808–3816 (2017).

107. Monroe, C. & Newman, J. The impact of elastic deformation on deposition kinetics at lithium/polymer interfaces. *J. Electrochem. Soc.* **152**, A396 (2005).

108. Han, F. *et al.* High electronic conductivity as the origin of lithium dendrite formation within solid electrolytes. *Nat. Energy* **4**, 187–196 (2019).

109. Ning, Z. *et al.* Visualizing plating-induced cracking in lithium-anode solid-electrolyte cells. *Nat. Mater.* **20**, 1121-1129 (2021).

110. Dixit, M. B. *et al.* In situ investigation of chemomechanical effects in thiophosphate solid electrolytes. *Matter* **3**, 2138-2159 (2020).

111. Hao, S. *et al.* Tracking lithium penetration in solid electrolytes in 3D by in-situ synchrotron X-ray computed tomography. *Nano Energy* **82**, 105744 (2021).

112. Kazyak, E. *et al.* Li penetration in ceramic solid electrolytes: operando microscopy analysis of morphology, propagation, and reversibility. *Matter* **2**, 1025-1048 (2020).

113. Yu, S. & Siegel, D. J. Grain boundary softening: a potential mechanism for lithium metal penetration through stiff solid electrolytes. *ACS Appl. Mater. Interfaces* **10**, 38151–38158 (2018).

114. Goodenough, J. B., Hong, H. Y. & Kafalas, J. A. Fast Na^+ ion transport in skeleton structures. *Mater. Rese. Bull.* **11**, 203-220 (1976).

115. DeWees, R. & Wang, H. Synthesis and properties of NaSICON-type LATP and LAGP solid electrolytes. *ChemSusChem* **12**, 3713–3725 (2019).

116. Chung, H. & Kang, B. Mechanical and thermal failure induced by contact between a $Li_{1.5}Al_{0.5}Ge_{1.5}(PO_4)_3$ solid electrolyte and Li metal in an all solid-state Li cell. *Chem. Mater.* **29**, 8611–8619 (2017).

117. Safanama, D. & Adams, S. High efficiency aqueous and hybrid lithium-air batteries enabled by $Li_{1.5}Al_{0.5}Ge_{1.5}(PO_4)_3$ ceramic anode-protecting membranes. *J. Power Sources* **340**, 294–301 (2017).

118. Kubanska, A. *et al.* Elaboration of controlled size $Li_{1.5}Al_{0.5}Ge_{1.5}(PO_4)_3$ crystallites from glass-ceramics. *Solid State Ion.* **266**, 44–50 (2014).

119. Zhang, M. *et al.* Preparation and electrochemical properties of $Li_{1+x}Al_xGe_{2-x}(PO_4)_3$ synthesized by a sol-gel method. *J. Electrochem. Soc.* **159**, A1114 (2012).

120. Takahashi, K. *et al.* A super high lithium ion conducting solid electrolyte of grain boundary modified $Li_{1.4}Ti_{1.6}Al_{04}(PO_4)_3$. *J. Electrochem. Soc.* **159**, A342A-348 (2012).

121. Cao, D. *et al.* Processing strategies to improve cell-level energy density of metal sulfide electrolyte-based all-solid-state Li metal batteries and beyond. *ACS Energy Lett.* **5**, 3468–3489 (2020).

122. Papakyriakou, M. *et al.* Mechanical behavior of inorganic lithium-conducting solid electrolytes. *J. Power Sources* **516**, 230672 (2021).

123. Homma, K. *et al.* Crystal structure and phase transitions of the lithium ionic conductor Li_3PS_4. *Solid State Ion.* **182**, 53–58 (2011).

124. Kato, Y. *et al.* High-power all-solid-state batteries using sulfide superionic conductors. *Nat. Energy* **1**, 16030 (2016).

125. Miura, A. *et al.* Liquid-phase syntheses of sulfide electrolytes for all-solid-state lithium battery. *Nat. Rev. Chem.* **3**, 189–198 (2019).

126. Bron, P. *et al.* $Li_{10}SnP_2S_{12}$: An affordable lithium superionic conductor. *J. Am. Chem. Soc.* **135**, 15694–15697 (2013).

127. Krauskopf, T., Culver, S. P. & Zeier, W. G. Bottleneck of diffusion and inductive effects in $Li_{10}Ge_{1-x}Sn_xP_2S_{12}$. *Chem. Mater.* **30**, 1791–1798 (2018).

128. Zheng, B. *et al.* Unraveling (electro)-chemical stability and interfacial reactions of $Li_{10}SnP_2S_{12}$ in all-solid-state Li batteries. *Nano Energy* **67**, 104252 (2020).

129. Schwietert, T. K. *et al.* Clarifying the relationship between redox activity and electrochemical stability in solid electrolytes. *Nat. Mater.* **19**, 428-435 (2020).

130. Lewis, J. A. *et al.* Role of areal capacity in determining short circuiting of sulfide-based solid-state batteries. *ACS Appl. Mater. Interfaces* **14**, 4051–4060 (2022).

131. Vadhva, P. *et al.* Electrochemical impedance spectroscopy for all-solid-state batteries: theory, methods and future outlook. *ChemElectroChem* **8**, 1930–1947 (2021).

132. Choi, W., Shin, H. C., Kim, J. M., Choi, J. Y. & Yoon, W. S. Modeling and applications of electrochemical impedance spectroscopy (EIS) for lithium-ion batteries. *J. Electrochem. Sci. Technol.* **11**, 1–13 (2020).

133. Doux, J.-M. *et al.* Pressure effects on sulfide electrolytes for all solid-state batteries. *J. Mater. Chem. A* **8**, 5049-5055 (2020).

134. Ohno, S. *et al.* How certain are the reported ionic conductivities of thiophosphate-based solid electrolytes? An interlaboratory study. *ACS Energy Lett.* **5**, 910–915 (2020).

135. Pietsch, P. & Wood, V. X-Ray tomography for lithium ion battery research: A practical guide. *Annu. Rev. Mater. Res.* **47**, 451–479 (2017).

136. Gürsoy, D., de Carlo, F., Xiao, X. & Jacobsen, C. TomoPy: A framework for the analysis of synchrotron tomographic data. *J. Synchrotron Radiat.* **21**, 1188–1193 (2014).

137. Scharf, J. *et al.* intelligence. Bridging nano- and microscale X-ray tomography for battery research by leveraging artificial intelligence. *Nat. Nanotechnol.* (2022) doi:10.1038/s41565-022-01081-9.

138. Lin, F. *et al.* Synchrotron X-ray analytical techniques for studying materials electrochemistry in rechargeable batteries. *Chem. Rev.* **117**, 13123–13186 (2017).

139. Egerton, R. F. *Physical Principles of Electron Microscopy* (Springer, 2016).

140. Zhang, D. *et al.* Atomic-resolution transmission electron microscopy of electron beam–sensitive crystalline materials. *Science* **359**, 675–679 (2018).

141. Taheri, M. L. *et al.* Current status and future directions for in situ transmission electron microscopy. *Ultramicroscopy* **170**, 86–95 (2016).

142. Yuan, Y., Amine, K., Lu, J. & Shahbazian-Yassar, R. Understanding materials challenges for rechargeable ion batteries with in situ transmission electron microscopy. *Nat. Comm.* **8**, 15806 (2017).

143. Boebinger, M. G. *et al.* Distinct nanoscale reaction pathways in a sulfide material for sodium and lithium batteries. *J. Mater. Chem. A* **5**, 11701-11709 (2016).

144. Boebinger, M. G. *et al.* Spontaneous and reversible hollowing of alloy anode nanocrystals for stable battery cycling. *Nat. Nanotechnol.* **15**, 475–481 (2020).

145. Boebinger, M. G. *et al.* Avoiding fracture in a conversion battery material through reaction with larger ions. *Joule* **2**, 1783-1799 (2018).

146. Volkert, C. A., Minor, A. M. Focused ion beam micromachining. *MRS Bull.* **32**, 389–399 (2007).

147. Lee, J. Z. *et al.* Cryogenic focused ion beam characterization of lithium metal anodes. *ACS Energy Lett.* **4**, 489–493 (2019).

148. Li, J., Deshpande, R. D., Cheng, Y.-T. & Verbrugge, M. W. Liquid metal alloys as self-healing negative electrodes for lithium ion batteries. *J. Electrochem. Soc.* **158**, A845 (2011).

149. Zachman, M. J., Tu, Z., Archer, L. A. & Kourkoutis, L. F. Nanoscale elemental mapping of intact solid-liquid interfaces and reactive materials in energy devices enabled by Cryo-FIB/SEM. *ACS Energy Lett.* **5**, 1224–1232 (2020).

150. Shen, F., Dixit, M. B., Xiao, X. & Hatzell, K. B. Effect of pore connectivity on Li dendrite propagation within LLZO electrolytes observed with synchrotron X-ray tomography. *ACS Energy Lett.* **3**, 1056–1061 (2018).

151. Dixit, M. B. *et al.* Nanoscale mapping of extrinsic interfaces in hybrid solid electrolytes. *Joule* **4**, 207–221 (2020).

152. Wu, X. *et al.* Operando visualization of morphological dynamics in all-solid-state batteries. *Adv. Energy Mater.* **9**, 1901547 (2019).

153. Sun, F. *et al.* Visualizing the morphological and compositional evolution of the interface of InLi-anode thio-LISION electrolyte in an all-solid-state Li-S cell by: In operando synchrotron X-ray tomography and energy dispersive diffraction. *J. Mater. Chem. A* **6**, 22489–22496 (2018).

154. Kimura, Y. *et al.* Influence of active material loading on electrochemical reactions in composite solid-state battery electrodes revealed by operando 3D CT-XANES imaging. *ACS Appl. Energy Mater.* **3**, 7782–7793 (2020).

155. Dixit, M. B. *et al.* Synchrotron imaging of pore formation in Li metal solid-state batteries aided by machine learning. *ACS Appl. Energy Mater.* **3**, 9534-9542 (2020).

156. Seitzman, N. *et al.* Toward all-solid-state lithium batteries: Three-dimensional visualization of lithium migration in β-Li_3PS_4 ceramic electrolyte. *J. Electrochem. Soc.* **165** A3732 (2018).

157. Harry, K. J., Hallinan, D. T., Parkinson, D. Y., MacDowell, A. A. & Balsara, N. P. Detection of subsurface structures underneath dendrites formed on cycled lithium metal electrodes. *Nat. Mater.* **13**, 69–73 (2014).

158. Madsen, K. E. *et al.* Direct observation of interfacial mechanical failure in thiophosphate solid electrolytes with operando X-ray tomography. *Adv. Mater. Interfaces* **7**, 2000751 (2020).

159. Spencer Jolly, D. *et al.* Sodium/Na β″ alumina interface: Effect of pressure on voids. *ACS Appl. Mater. Interfaces* **12**, 678–685 (2019).

160. Neumann, A. *et al.* Analysis of interfacial effects in all-solid-state batteries with thiophosphate solid electrolytes. *ACS Appl. Mater. Interfaces* **12**, 9277-9291 (2020).

161. Tarhouchi, I., Viallet, V., Vinatier, P. & Ménétrier, M. Electrochemical characterization of $Li_{10}SnP_2S_{12}$: An electrolyte or a negative electrode for solid state Li-ion batteries? *Solid State Ion.* **296**, 18–25 (2016).

162. Lu, Y. *et al.* Critical current density in solid-state lithium metal batteries: Mechanism, influences, and strategies. *Adv. Funct. Mater.* **31**, 2009925 (2021).

163. McDowell, M. T. *et al.* Studying the kinetics of crystalline silicon nanoparticle lithiation with in situ transmission electron microscopy. *Adv. Mater.* **24**, 6034–6041 (2012).

164. Yao, Y. *et al.* Interconnected silicon hollow nanospheres for lithium-ion battery anodes with long cycle life. *Nano Lett.* **11**, 2949–2954 (2011).

165. Huang, W. *et al.* Dynamic structure and chemistry of the silicon solid-electrolyte interphase visualized by cryogenic electron microscopy. *Matter* **1**, 1232–1245 (2019).

166. He, Y. *et al.* Progressive growth of the solid–electrolyte interphase towards the Si anode interior causes capacity fading. *Nat. Nanotechnol.* **16**, 1113–1120 (2021).

167. Wang, C. *et al.* Solvent-free approach for interweaving freestanding and ultrathin inorganic solid electrolyte membranes. *ACS Energy Lett.* **7**, 410–416 (2022).

168. Chen, Y. T. *et al.* Fabrication of high-quality thin solid-state electrolyte films assisted by machine learning. *ACS Energy Lett.* **6**, 1639–1648 (2021).

169. Balaish, M. *et al.* Processing thin but robust electrolytes for solid-state batteries. *Nat. Energy* **6**, 227–239 (2021).

170. Ye, L. & Li, X. A dynamic stability design strategy for lithium metal solid state batteries. *Nature* **593**, 218–222 (2021).

171. Su, Y. *et al.* A more stable lithium anode by mechanical constriction for solid state batteries. *Energy Environ. Sci.* **13**, 908–916 (2020).

172. Luo, S. *et al.* Growth of lithium-indium dendrites in all-solid-state lithium-based batteries with sulfide electrolytes. *Nat. Comm.* **12**, 6968 (2021).

173. Tan, D. H. S. *et al.* Carbon-free high-loading silicon anodes enabled by sulfide solid electrolytes. *Science* **373**, 1494–1499 (2021).